SCANNING PROBE MICROSCOPIC STUDY OF PIEZOTRONICS AND TRIBOELECTRIFICATION FOR THEIR APPLICATIONS IN MECHANICAL SENSING

A Dissertation

Presented to

The Academic Faculty

by

Yusheng (Alvin) Zhou

In Partial Fulfillment

of the Requirements for the Degree

Doctor of Philosophy in the

School of Materials Science and Engineering

Georgia Institute of Technology

May, 2015

SCANNING PROBE MICROSCOPIC STUDY OF PIEZOTRONICS AND TRIBOELECTRIFICATION FOR THEIR APPLICATIONS IN MECHANICAL SENSING

Approved by:

Dr. Zhong Lin Wang, Advisor

School of Materials Science and Engineering

Georgia Institute of Technology

Dr. Meilin Liu

School of Materials Science and Engineering

Georgia Institute of Technology

Dr. Zhiqun Lin

School of Materials Science and Engineering

Georgia Institute of Technology

Dr. Oliver Brand

Electrical and Computer Engineering

Georgia Institute of Technology

Dr. Levent Degertekin

School of Mechanical Engineering

Georgia Institute of Technology

Date Approved: January 06, 2015

[To the students of the Georgia Institute of Technology]

ACKNOWLEDGEMENTS

In the first place, I would like to express my deep appreciation to my advisor Prof. Zhong Lin Wang for his guidance and support to my Ph.D study and research through the last four and half years. Prof. Wang taught me not only a systematic approach to conduct academic research, but also helped me as a mentor to build a stronger personality with optimism, dedication, perseverance and persistence. I believe all these characteristics I learned from him will benefit me for the rest of my life. Also, I would like to thank the rest of my thesis committee: Prof. Meilin Liu, Prof. Zhiqun Lin, Prof. Oliver Brand, and Prof. Levent Degertekin, for their insightful comments and intriguing questions.

I have been also very fortunate to work with the incredible people in our research group. Without their help and collaborations, I can't imagine any of my achievements. In particular, I would like to thank Dr. Guang Zhu for coaching me hands on experimental skills and clean room techniques as well as discussing research ideas; thank Dr. Weihua Han for teaching me on processing data and organizing manuscript; thank Dr. Ronan Hinchet for telling me his tips to keep all information organized in such an information explosion era; thank Ken Pradel for generous help on improving my languages for many written documents; thank Dr. Yong Ding for teaching me and conducting the TEM characterization for my sample; thank Yolande Berta and Tim Zhang for training me on SEMs; thank Dr. Sihong Wang, Dr. Ying Liu, Simiao Niu, Long Lin, Shengming Li, Dr. Caofeng Pan, Dr. Youfan Hu, Dr. Ya Yang, Dr. Cheng-

Ying Chen for insightful discussion on designing experiments, drawing insights from data and organizing them. There are many other group colleagues who have been kind and helpful to me and I want to leverage this opportunity to thank them all! I would also like to thank my master thesis advisor Prof. Jun-en Yao, Prof. Guangyi Shang and labmate Dr. Wei Cai for the prior training which prepared me with the knowledge and experimental skills in SPM for my Ph. D research.

I would also thank my friends who I have been spending memorable time with and gain support from. Gareth Guvanasen, Martin Mueller, Mandy Luo, Giang Do, Shannon Yu, Fuzhu Zhou, Jingyi Zhang, Fang Gao, Ashley Nelson, James Compagnoni, to name a few. Also, I want to specially thank a friend from China-Jingyuan Yu. Even though we only reunion once since I came to US, he made himself always available talking and comforting me during my rough times.

Last but not least, I would like to send my most special thanks to my beloved ones. My parents have always been a spiritual support to me. I apologize for not being able to stay with them as frequent as others parents' kids did. I hope to have more opportunity to have family reunion in the future. Also, many thanks to my grandparents and other family members who have been caring about me. Finally, I feel very fortunate to have met my girlfriend this past summer and I am grateful for her being supporting me through the last seven months of my PhD life!

TABLE OF CONTENTS

Page

ACKNOWLEDGEMENTS iv

LIST OF TABLES ix

LIST OF FIGURES `x

LIST OF ABBREVIATIONS xviii

SUMMARY xix

CHAPTER

1 INTRODUCTION 1

1.1 Demand for technology advancement in mechanical sensors 2

1.2 Piezotronic effect in nanowires– a potential solution for high spatial resolution and high sensitivity strain/force sensing 5

1.3 Triboelectrification, triboelectric nanogenerators (TENGs) and self-powered sensors – technologies for self-sustained sensing system 7

1.4 Thesis background and scope – SPM study of piezotronic and triboelectric effects, and development of a self-powered motion sensor 9

2 CHARACTERIZATION OF THE PIEZOTRONIC EFFECT IN VERTICAL ALIGNED CDSE NANOWIRES 9

2.1 Synthesis of vertically aligned CdSe NW arrays 14

2.2 Electrical property at Pt-CdSe interface modulated by longitudinal force 15

2.3 Theoretical discussion – Schottky barrier height modulated by stress/strain induced polarization 18

3 CHARACTERIZATION OF THE PIEZOTRONIC EFFECT IN GaN NANOWIRES FOR TRANSVERSE FORCE SENSING 18

3.1 AFM based experiment method to characterize GaN nanowires in bending 18

3.2 Electrical property at the Pt-GaN interface modulated by transverse force 22

3.3 Transverse force sensitivity - theoretical model and experimental results 30

4 IN-SITU CHARACTERIZATION OF TRIBOELECTRIFICATION 34

4.1 Existing characterization methods 34

4.2 SPM based methods for in-situ quantitative characterization 35

4.3 Multi-friction effect on triboelectric charge transfer 39

4.4 Surface diffusion of tribo-charge and quantification of its coefficient 42

4.5 Nano-patterning of surface charge via triboelectrification 46

5 MANIPULATION OF THE TRIBOELECTRIC PROCESS BY ELECTRIC FIELD 48

5.1 Existing approaches for modulating triboelectric charge transfer 48

5.2 Theoretical model for electric field’s influence on triboelectrification 51

5.3 SPM based experiment method – manipulation and characterization 55

5.4 Results and Discussion 57

6 SELF-POWERED DISPLACEMENT SENSOR BASED ON MICRO-GRATED TRIBOELECTRIFICATION 63

6.1 Fundamental mechanism of TENG and self-powered displacement sensor 64

6.2 Grating structure design for higher resolution and long working distance 70

6.3 Device fabrication and displacement sensing test 75

6.4 Reproducibility and reliability test 80

6.5 Dynamic speed sensing using amplitude of SC current 83

6.6 Dependence of sensor resolution on grating size 85

6.7 Asymmetric feature design for direction identification 89

7 CONCLUSION 92

REFERENCES 94

LIST OF TABLES

Page

Table 2.1: The parameters used for the simulation of CdSe NW. 14

Table 3.1: Goodness of linear fitting of experimental ln*I*-*F* data. 28

Table 3.2: The parameters used in estimate the Schottky barrier change. 30

Table 6.1: Parameter used for the grating structure simulation. 74

LIST OF FIGURES

Page

Figure 1.1: Various applications demand development of advanced sensing technologies for low power consumption and/or high sensitivity/resolution 1

Figure 1.2: (a) Schematic and (b) optical image of ZnO NW strain sensor. (c) I-V characteristics of ZnO NW as a function of applied strain. (d) Logarithm plot of the current (in A) at fixed bias of V = 1.5 and 2.0 V as a function of strain3. 3

Figure 1.3: Change in energy band diagram for Ag-ZnO-Ag structure as a function of piezopotential. 4

Figure 2.1: Vertically aligned CdSe NW array grown on the mica substrate. (a) Side view SEM images of the short (~ 200-500 nm) NWs and (b) long (~ 2-4 μm) NWs; (c) TEM image of a NW with low magnification; (d) High Resolution TEM (HRTEM) image of CdSe NW; (e) Corresponding selected-area electron diffraction (SEAD) pattern from the region indicated by dashed circle in image. 12

Figure 1.2: Schematic illustration of wurtzite crystal structure of CdSe. 13

Figure 1.3: Piezopotential distributions under normal force ranging from 100 nN to 400 nN. Geometry of the NW used in the simulation is diameter D=60 nm, length L=250 nm. 14

Figure 1.4: (a) Schematic for the piezotronic effect measurement experiment; (b) band diagram of the interface between Pt and CdSe (left) and the change of Schottky barrier by the piezopotential; (c) I-V characteristics of a single CdSe NW measured by C-AFM under different applied forces; (d) Plot of lnI as a function of V; (e) calculated barrier height change from the measured I-V characteristics. 16

Figure 3.1: a) 90˚ tilted SEM view of the vertically aligned GaN NW array grown on Si substrate. b) Low magnification TEM image of a GaN NW. c) High resolution TEM image and corresponding SAED pattern (inset). 20

Figure 3.2: (a) Schematic of the AFM experimental setup. (b) AFM image of a 90° tilted GaN NW. The red mark on one of the NWs indicates the location of the AFM tip during the electrical measurement. (c) Illustration of the experiment process: from top to bottom, the cantilever deflection that is proportional to the applied force on the GaN NW; a bias applied between the AFM tip and the sample; and the corresponding detected current. 21

Figure 3.3: a) Schematic of the AFM tip touching a NW on the middle. b)) Illustration of a good experiment process: the NW does not slip on the edge of the NW, c) Schematic of the AFM tip which is slipping on the edge of a NW. d) Illustration of a bad experiment process: the NW slipped on the edge of the NW and then the cantilever deflection extend curve shows a discontinuity. 21

Figure 3.4: a) Finite element simulation of the potential distribution at the surface of a GaN NW when subjected to a transverse force. b) Positive piezoelectric potential generated in the NW as a function of the transverse force applied. The geometry of the GaN NW used in simulation is 1um in length, 60 nm in diameter. c) AFM measurements of the piezoelectric potential generated by a GaN NW under different bending forces. 22

Figure 3.5: a) Energy band diagram of the electrical circuit, b) and its change with an external force induced piezopotential on GaN NWs. c) Experimentally measured I-V characteristics under a constant transverse force of 104 nN, and d) at different forces between 104 nN and 312 nN. 25

Figure 3.6: (a) Plot of measured current as a function of applied forces under forward bias (blue) and reverse bias (red) and their respective fitting curves. Red curve is an exponential fit, blue curve is a linear fit. (b) Plot of relative current change as a function of applied force. 27

Figure 3.7: Comparison of lnI-V (left) and lnI-V1/4 curve (right). 28

Figure 3.8: Calculated SBH change as a function of the applied force. 30

Figure 3.9: (a) Under constant applied voltage, the current passing through the GaN NW increased step-by-step as the applied force increased. (b) lnI-F curve demonstrating a linear relation between lnI and applied force. (c) Time response of the current change in response to the increased force (left) and deceased force (right). 33

Figure 3.10: (a) Calculated contact area as a function of applied force. (b) Measured current as a function of applied force. 33

Figure 4.1: (a) Schematic of a Rolling Sphere Tool. (b) Measured charge accumulation on the sphere as a function of rolling time. 36

Figure 4.2: Schematic illustration of the experiments based on AFM. (a) triboelectric charge generation by friction between AFM probe and SiO2 (b) subsequent surface potential characterization in the SKPM mode. (c) AFM topography of SKPM surface potential image (d) AFM topography of a larger area on SiO2. The dashed line corresponds to the profile in (f). (e) 3D image of the measured surface potential profile. (f) Cross section profile of the potential distribution. (g) Simulated electric potential distribution in vertical direction under the condition when surface potential was measured in SKPM. Parameters used in simulation: the apex angle of the AFM probe was set to 35˚ with a tip radius of 10 nm, and had potential of -0.168 V; the center 4 μm area on top surface of SiO2 had surface charges with density of -29 μC/m2 and the bottom surface of SiO2 was grounded. The inset is an enlarged picture of the tip area. 37

Figure 4.3: Triboelectric charge accumulation on the SiO2 surface with the increase of the number of repeated rubbing at the same area. (a) Series of surface potential images taken in the same area from intact status to the one after 8th rubbing cycles, and (b) their corresponding potential profiles. (c) Derived surface charge density as a function of the number of friction cycles, and our fit based on charge accumulation theory described in equation 4.4. 40

Figure 4.4: Estimated surface charge density as a function of the number of friction cycles for negative charge, and a fit based on charge accumulation theory 43

Figure 4.5: Charge diffusion over time. (a) Series of images of surface potential distribution as a function of time after the triboelectrification. (b) COMSOL simulation of surface charge density distribution. Initial charge density was set to be a Gaussian distribution: 4.5×1014 exp[-1.2×1011(x2 + y2)], and diffusion coefficient to be 1.10×10-15 m2/s. (c) the cross sections of the series of images in (a). (d) 1D Gaussian fit of the surface charge distribution at 12 min (blue) and 84 (red) min, respectively. Time constant (D*t) can be derived from this fitting. (e) Time constant at different time and its linear fitting. The slope indicate diffusion coefficient. (f) The profiles of series of surface charge distribution images in (b). 44

Figure 4.6: (a) Spreading of charge density profile for a negative triboelectrification process as a function of time. (b) Time constant at different time and its linear fitting for the negative charges. The slope indicates the diffusion coefficient. For this fitting, R2 = 0.9980 47

Figure 4.7: Patterning of the surface triboelectric charges on an insulator surface. Patterning of negative charges: (a) surface topography image, (b) 2D, and (c) 3D images of charge density after patterning. Patterning of positive charges: (d) surface topography image, (e) top and (f) side view of 3D images of charge density after patterning. 48

Figure 5.1: Triboelectric materials series. 50

Figure 5.2: (a) Illustration of the contact electrification process with a tunneling width z, the charge transferred to the dielectric surface with a density of σ, induced charge density σ1 and σ2. (b-f) Energy band diagrams for the metal and dielectric materials in the situations of pre-contact (b), in contact with no bias (c), in separation equilibrium with no (d), positive (e) and negative (f) bias. 52

Figure 5.3: Schematic of experiment setup including two steps: (a) the first step is to use AFM tip with a bias between the tip and the substrate scan over the surface in contact mode, (b) the second step is to use SKPM to map the surface potential distribution. (c) Surface potential distribution of the rubbed and the surrounding area after regionally rubbed by AFM tip at no bias and 5 V bias immediately after rubbing and 1 hr later, demonstrating that bias can reverse the triboelectric charge transfer, and the transferred charges have little leakage or diffusion. 57

Figure 5.4: (a) Surface potential distributions of the Parylene film including the areas that were rubbed by Pt coated AFM tip at different bias from -2 V to 5 V. (b) Cross section profiles of the surface potential of the Parylene film rubbed with bias from -10 V to 10 V. The inset is the calculated surface charge density as a function of bias. With a bias of about 2.5 V, the surface charge density is zero, indicating the contact electrification is completely canceled out by the applied bias. 58

Figure 5.5: Thickness dependence of contact electrification and bias modulation. (a) Images of surface potential change ΔV of different thickness samples after they were rubbed at no bias (i) and nullify bias (ii), respectively. (b) The surface potential change and surface charge density as a function of the thickness of the Parylene layer after the sample was rubbed at no bias. (c) The nullify bias as a function of the thickness of the Parylene layer. (d) Images of surface potential change ΔV of different thickness samples after they were rubbed by different cycles. (e) Calculated surface charge density as a function of friction cycles. (f) The surface potential change and charge density after 20 cycles of friction as a function of thickness of Parylene. 61

Figure 6.1: Schematic illustration of sliding mode TENG. Charge and electric field distribution when two plates (a) overlap each other and (b) separate for a certain distance. 67

Figure 6.2: FEM calculation results of dielectric-to-dielectric TENG in open-circuit (OC) condition. (a) Structure of the FEM model. (b) Calculated electric potential distributions at different sliding distances x. (c) Mesh convergence of VOC when x = 5 cm. (d) Calculated VOC at different x, the inset is the profile of the VOC when x approaches to l. (e-f) Distribution of (e) the X-component and (f) the Y-component of the electric field (the scale in X-direction is 1:5 to the real case). (g-h) Calculated charge distribution of (g) the upper face of the bottom electrode and (h) the lower face of the top electrode, the inset is the enlarged profile of the surface charges at the edges when x = 0.09 m. 68

Figure 6.3: Analysis of the V-Q-x relationship. (a) FEM-calculated linear V-Q relationship of dielectric-on-dielectric TENG. (b-c) Comparisons of parameters (b) A and (c) B obtained through different methods: numerical FEM calculation, semi-analytical interpolation, and theoretical equation. The insets are the profile of the parameters (b) A and (c) B when x approaches to l0. 70

Figure 6.4: Structure of a triboelectric motion sensor. (a) Schematic of a pair of micro-gratings and detailed information of layers illustrated in the inset. (b, c) Optical photograph of as-fabricated micro-grating pair with sizes of ~30 ×15 mm2 for the top grating and ~60×30 mm2 for the bottom grating. (d) Scanning electron microscopic (SEM) images of the top micro-grating with glass slide substrate. The insets show the cross section profile: the ITO layer on top of the patterned SU-8 photoresist serves as the top electrode, and the outmost layer is Parylene film serving as electronegative material that participates in the triboelectric charge transfer. (e) SEM images of the bottom micro-grating. The insets show the cross section profile: the etched Silicon is coated with Al as bottom electrode and SiO2 as electropositive material for triboelectrification. 72

Figure 6.5: Working principle of the micrograting motion sensor. (a) Sketches that illustrate relative moving between two grating pair, leading to the charge transfer between two metal electrodes. Within a cycle of the displacement, the micrograting pair experiences conditions of full overlap, partially separation, full separation, partially separation and full overlap. (b) Numerical simulation of the electrical potential in open circuit condition (blue curve) and charge in the top metal electrode in short circuit condition (red curve). The short circuit current (green curve) is calculated from the charge change by assuming a constant moving speed of 1 mm/s. In OC condition, the potential valley and the peak present at two ends (full overlap) and the middle (full separate), respectively. In the SC condition, current changes signs from negative to positive at the two ends, from positive to negative in the middle. 73

Figure 6.6: Illustration of the electrical potential change when the top grating moves one period. The figures from the left to the right describe different status: full overlap – half separation – full separation – half separation. 74

Figure 6.7: Experimental setup for the motion sensor testing. (a) The top grating is attached to an Acrylic plate using two pieces of adhesive sponge as cushion, the Acrylic plate is fixed on a 1-dimensional linear motor attached on a vertical positioner. The bottom grating is fixed on a plate that is attached with two 1D positioners and a tilt and rotation platform. (b) Detailed amplification of the two grating pair when they are in contact. 77

Figure 6.8: Demonstration of the long distance motion sensing by the OC voltage peak and SC zero-crossings counting method. (a) The OC voltage signals acquired from a displacement of 9.2 mm at a preset speed of 1 mm/s. (b) An enlarged view of the OC voltage signal from a, showing a similar shape as expected from aforementioned numerical simulation. (c) The real time displacement and speed derived from the measured voltage signal. (d) The SC current signals acquired from a non-uniform motion (decelerate - uniform speed - deceleration). (e) The preset motor's trajectory (red curve) and the real time displacement detected by the motion sensor (blue dots). (f) The preset motor's speed (red curve) and the real time speed detected by the motion sensor (blue dots). 79

Figure 6.9: High resolution in displacement sensing realized by analyzing the magnitude of the OC voltage. (a) The OC voltage measured with a step motion of 5 μm per step within a pitch (200 μm). (b) Step motion with 1 μm per step in the sensitive region (10-190 μm) can be clearly resolved through the OC voltage signal. Given the RMS value of noise (0.38 mV), and the voltage change corresponding to 1 μm step motion (2.2 mV), the resolution can be calculated to be 173 nm. (c) OC voltage signal from 1 mm displacement. The shape of voltage signal within a pitch is very repeatable across pitches. 80

Figure 6.10: The noise of the voltage output signal. 82

Figure 6.11: The OC voltage in response to displacement from different as-fabricated devices with feature size of 100 μm (a-b). 82

Figure 6.12: The voltage output of the displacement sensor before and after about 1000 cycles of friction between Parylene and SiO2 are shown in (a) and (b). 83

Figure 6.13: The SEM image of Parylene surface after about 1000 cycles' friction with SiO2 84

Figure 6.14: Real time speed detection through SC current. (a-d) The SC current measured with motion speed from 10 μm/s, 100 μm/s, 1 mm/s, 10 mm/s, respectively. (e) A plot of SC current as a function of motion speed from 5 μm/s to 10 mm/s with a calculated sensitivity of 689±4 pA (mm/s). (f) Speed resolution for different grating feature width at the measurement noise level of 1 pA. 85

Figure 6.15: OC voltage output from a sensor with a period of 40 μm under (a) uniform speed displacement condition, and (b) step motion (2 μm /step) condition 87

Figure 6.16: COMSOL simulation to illustrate the influence of the grating size on the OC voltage and the sensor's displacement sensitivity. Simulation of the electric potential distribution in open circuit condition of a grating pair with the grating size (as half of its period) of 100 μm (a, c) and 10 μm (b, d), respectively. In the model, side walls were neglected. Black lines that represent the sidewall were added afterwards to illustrate the structure of the grating more clearly. (e) Simulated OC voltage output as a function of grating size. (f) The sensitivity, defined as the measured range in a half cycle divided by OC voltage, is a function of the grating size. 88

Figure 6.17: Charge transfer between two electrodes under SC condition as a function of the grating feature size simulated by COMSOL. The inset shows a zoomed-in regime. (b) Calculated SC current as a function of motion velocity for grating pairs with different feature widths. (c) Considering the 1 pA (RMS value) of the measurement system noise level, the speed resolution as a function of grating feature width. 89

Figure 6.18: Moving direction can be identified using asymmetric grating patterns. (a) Illustration of triangle bottom grating structure (blue) and its overlapping area with regard to the top grating (yellow) at forward and backward motion. Overlapping area change as a function of displacement within one pitch at forward (b) and backward (c) motion. (d), (e), (f) experimental results of the SC charge transfer as a function of displacement. 90

LIST OF ABBREVIATIONS

TENG	Triboelectric Nanogenerator
SPM	Scanning Probe Microscopy
AFM	Atomic Force Microscopy
SKPM	Scanning Kelvin Probe Microscopy
SBH	Schottky Barrier Height
OC	Open Circuit
SC	Short Circuit

SUMMARY

As an important component in the modern industrial world, mechanical sensors have been driven by the emerging “internet of things” and artificial intelligent era toward more demanding features. On one hand, applications in human machine interface, artificial skin and cell manipulation are demanding high sensitivity and/or high spatial resolution sensors. On the other hand, increasing adoption of wireless technologies such as mobile computing devices, wireless sensor networks and bio-implantable devices requires their components to have ultra-low power consumptions. While optimizing structural design of existing sensing technology and combining it with advanced microcircuits is a typical approach to enhance their features incrementally, exploring and innovating new sensing mechanisms that lead to a gigantic leap in performance will be of great scientific interest.

Piezotronic effect, recently found in semiconductor piezoelectric nanowires, has shown much higher sensitivity for strain sensing than the traditional piezoresistivity. To demonstrate its potential as a building block for force or strain micro sensor arrays, AFM based methods are developed to characterize both longitudinal and transverse sensing modes in CdSe, and GaN nanowires, respectively. Both experimental results show exponential response of their conductivity change to applied forces. Theoretical models are also presented to explain this mechanism and quantify the relationship, where strain induced piezoelectric polarization changes the metal-semiconductor

Schottky barrier height. The superior performance in sensitivity due to interface modulation plus the nanowires' small size will have promising applications in areas that needs high spatial resolution and high sensitivity force/strain sensors.

Triboelectric nanogenerators (TENGs) have recently been invented for harvesting mechanical energy, showing great promise for powering self-sustained systems. However, characterization and control of charge transfer is of great interest for improving TENGs' performance. In this thesis, a scanning probe microscopy based method is developed to characterize the triboelectric process, including tribo-charge intensity, multi-cycle friction effect, as well as its surface diffusion. Beyond that, effect of external electric field was investigated as an approach to manipulate the polarization and intensity. Finally, a concept of self-powered motion sensing technology is developed and demonstrated experimentally with nanometer resolution, long working distance as well as high robustness. It provides a promising solution for application areas that need ultra-low power consumption devices.

CHAPTER 1

INTRODUCTION

1.1 Demand for technology advancement in mechanical sensors

Mechanical sensors that can convert force, strain or displacement into electrical signals are used ubiquitously in many industries such as consumer electronics, automobile, advanced manufacturing, oil and gas, health care devices and so forth. Nowadays, on one hand, applications in human machine interface, artificial skin[1] and cell manipulation[2] require high sensitivity and/or high spatial resolution. On the other hand, wide adoption of mobile computing, sensor networks and bio-implantable devices need the mechanical sensing technology to have ultra-low power consumptions or self-powered devices.

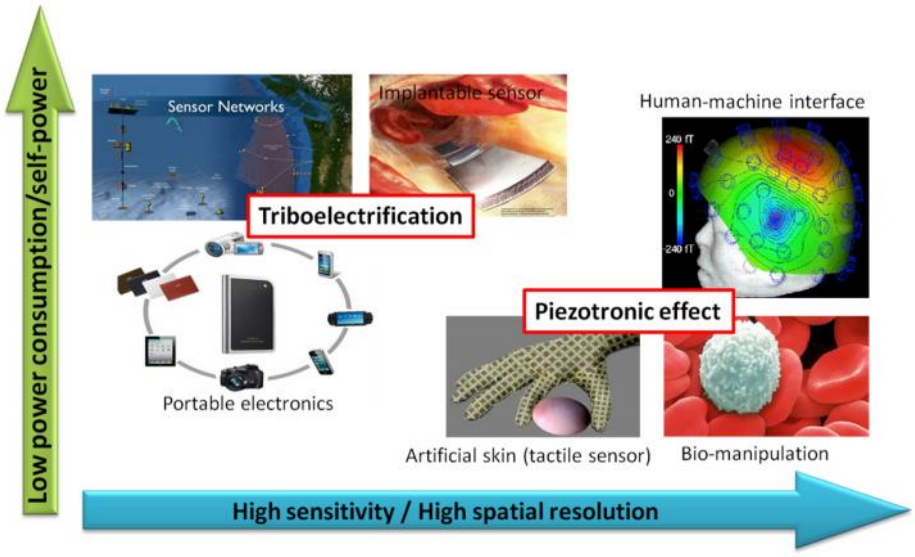

Figure 1.1 Various application demands development of advanced sensing technology for low power consumption and/or high sensitivity/resolution

1.2 Piezotronic effect in nanowires – a potential solution for high spatial resolution and high sensitivity strain/force sensing

For high sensitive and high resolution sensing, recently discovered piezotronic effect in piezoelectric semi-conductive nanowires has shown great potential in sensing strain.[3, 4] This effect refers to a phenomenon that the conductivity of the piezoelectric semiconductor-metal interface changes exponentially with applied strain in the nanowire[3, 5, 6]. It was first reported in ZnO nanowires (NWs) from our group. The conductivity of the ZnO NW was found to be strongly influenced by the axial strain on the NW. This phenomenon was explained through a coupling effect between the material's piezoelectric property and metal-semiconductor property - strain induced polarization in the nanowire changes the Schottky junction barrier height and the interface resistivity[6].

Using this effect, J. Zhou, et al. demonstrated a single ZnO NW strain sensor with much higher sensitivity than conventional sensors[3]. In this device, a single ZnO NW was fixed on a flexible substrate using silver paste (Figure 1.2 a&b). The electric measurements were then conducted at different substrate bending status. Because the thickness of the substrate is much larger than the diameter of the nanowire, the strain exerted on the nanowire through the silver paste was approximated to be axial strain. Figure 1.2c shows the measured I-V characteristics at different levels of strain. The current under fixed voltage was found to be exponentially correlated with the calculated axial strain on the NW, as shown in Figure 1.2d. They calculated the gauge factor (GF)

of their strain sensor to be as high as 1250, much greater than that of conventional metal strain gauges (1-5) or state-of-the-art doped-Si strain sensors (~200)[3].

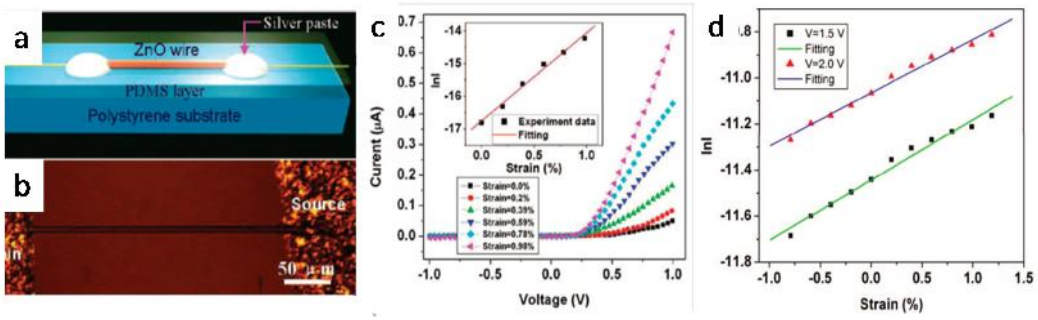

Figure 1.2 (a) Schematic and (b) optical image of ZnO NW strain sensor. (c) I-V characteristics of ZnO NW as a function of applied strain. (d) Logarithm plot of the current (in A) at fixed bias of V = 1.5 and 2.0 V as a function of strain[3].

A qualitative explanation was given by assuming that the current flow through the NW was dominated by the reversed biased Schottky junction[7]. In this case, two Schottky contacts formed at the Ag-ZnO interfaces, as shown in Figure 1.3. Under axial strain, one end has a positive piezoelectric potential while the other has a negative one. The Schottky barrier height (SBH) on the positive potential side increased with strain while the SBH decreased in the negative side. As the conductivity is dominated by the reverse biased Schottky barrier, the current increased in one direction while decreased in the opposite direction.

The model suggests that the current is exponentially dependent on the SBH, as described in equation 1.1, which is in agreement with their experimental results[7].

$$\ln I(\text{£}_{zz})/I(0) = -\Delta\text{¤}_s / kT \qquad (1.1)$$

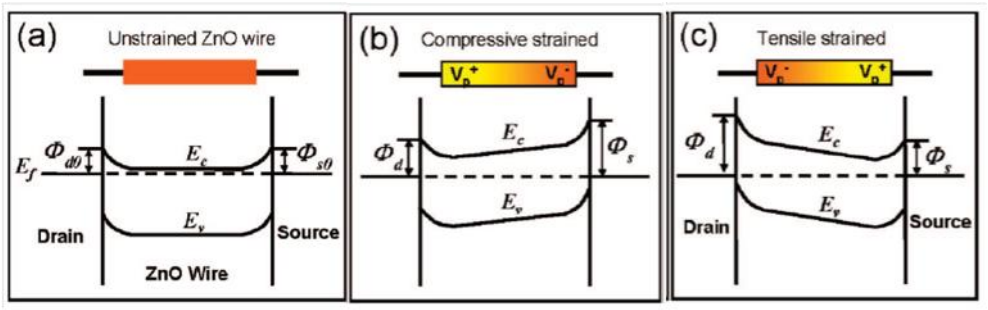

Figure 1.3 Change in energy band diagram for Ag-ZnO-Ag structure as a function of piezopotential[7].

Recently, a more detailed model for the mechanism of piezotronic effect was reported using semiconductor theory by Yan Zhang, et al[6]. As explained in their paper, the critical role of the piezoelectric charge is to induce an abrupt depletion layer in the semiconductor side close to the interface. This extra depletion layer changes the local electric field and thus changes the height of the Schottky barrier formed between the semiconductor NW and the metal.

Based on the piezotronic effect, various nano-electromechanical devices have been demonstrated. Wenzhuo Wu, et al, fabricated a piezoelectrically triggered mechanical-electronic logic cell[8], and nanowire-based resistive switches as programmable electromechanical memory[9].

Its nature of interface modulation, as compared to bulk modulation in traditional piezoresistive effect, has been demonstrated to have much higher gauge factor[3, 10], showing great potential in applications that need high sensitivity in force/strain transduction. The piezotronic effect in nanowires shows great potential to be utilized as

building blocks for ultra-sensitive force/strain sensor arrays for human and machine interface.

For tactile sensors to fully resolve a force pattern, shear force is an important component to detect[11-13]. For vertically aligned nanowires that grow along c axis, both longitudinal and share stress/strain can induce piezoelectric polarization in the nanowires. Furthermore, the polarization will be dominating at different interfaces: longitudinal stress induced polarization is at top and bottom surface and transverse at side surfaces[14, 15]. Therefore, it is possible to integrate both modes into one nanowire, which can largely building blocks.

It is an essential first-step to characterize the piezotronic effect in a single nanowire at both longitudinal and transverse force mode. However, previously reported structure that fixed the nanowire on a flexible substrate through silver paste anchoring its two ends, complicated the exertion of longitudinal force/stress when the substrate was bending. This indirect way of force control makes the measurement hard to be accurate. More importantly, the transverse mode cannot be characterized through this method.

1.3 Triboelectrification, triboelectric nanogenerators (TENGs) and self-powered sensors – technologies for self-sustained sensing system

As a potential energy solution for self-sustain sensor network system, the recently invented device - triboelectric nanogenerators (TENGs) [16-19], have shown

superior performance in harvesting mechanical energy compared to other technologies such as piezoelectric based devices. The core working principle of TENGs is to transform external movement into cyclic contact-separation between two dissimilar materials, the surfaces of which are inversely charged due to triboelectrification[20]. It results in a cyclically changing electric field, which drives electrons to flow in the external circuit through electrostatic induction. Unlike electrostatics that is well explained by Maxwell equations, the triboelectrification is still not fully understood[21]. The tribo-charge density transferred on the surfaces plays a critical role in the output performance of these TENGs[25, 26]. Although different kinds of TENGs have been designed to scavenge mechanical energy from impacts[22], sliding[23], and rotations[24], the mechanisms of the triboelectric process is still unclear and few approaches that can control the tribo-charge with predetermined materials were reported.

Triboelectric or contact electric effect has been ubiquitously known for decades and has extensive applications such as powder spray painting[25], particle-separation[26], and recently developed energy harvesting[16, 17] and chemical sensing[27]. However, its mechanisms are still not well understood. The difficulties in studying it arise, in part, from the complexity of the phenomena, and in part, from lack of standard instrumentation and procedures for accurately controlling the contact electrification process and quantifying contact charging. The existing approaches uses macro scale apparatuses to generate contact electrification and then measure the charge through surface electrostatic force[28], charge induction[21], or surface potential[29]. However, theses

triboelectric characterization methods are based on macro scale experimental setups, which measures the averaged tribo-charge transfer process, thus hardly achieving a quantitative characterization of the process occurred at the interface.

In addition, it is desirable to have approaches to control the trio-charge polarity and density. On one side, in the very long term after the first discovery of this effect, it has been always regarded as detrimental problems in a numbers of situations such as electronic circuits and systems, which thus attracts extensive efforts to alleviate or eliminate this phenomenon[30]. On the other side, for applications that positively utilize this effect such TENGs, increasing its charge transfer density is an essential way to boost it energy harvesting performance[31].

1.4 Thesis background and scope – SPM study of piezotronic and triboelectric effects, and development of a self-powered motion sensor

Equipped with a mechanical probe with sharp tip and accurate 3-D position control capability, scanning probe microscopy (SPM) is demonstrated with atomic level resolution in imaging and various controllable interactions with samples[32]. Therefore, it provides a powerful tool to study the piezotronic and triboelectric effects at the nano scale. The first two parts of this thesis focuses on developing SPM based methodologies.

1) AFM studies of piezotronic effect in piezoelectric semiconductor nanowires. Chapter 2 and 3 present AFM based methods that can characterize the piezotronic effect

in the nanowires with direct and accurate control. Both the vertical and transverse mode is demonstrated in CdSe and GaN nanowires, respectively.

2) SPM characterization and manipulation of triboelectric effect. Chapter 4 focuses on developing an in-situ method that can quantitatively characterize the charge transfer and migration between metal and dielectric materials. This work will provide a powerful tool for researchers in the triboelectric research field to study many fundamental issues that influence triboelectrification such as electrical field, humidity, temperature, difference between contact and friction, etc. Chapter 5 focuses on developing an extrinsic approach to modulate the contact electrification process. A theoretical model is proposed for predicting the modulation effect and experiments were conducted to validate the model. This approach can be potentially utilized to enhance the output performance of energy harvesting devices or nullify the contact electric charge transfer in applications where this effect is undesirable.

3) Self-powered motion sensing technology. Finally, Chapter 6 presents a self-powered displacement and speed sensor based on micro-grated triboelectric effect. The device generates electric sensing signals in response to mechanical displacement without need for external power supply. It demonstrates a concept of zero power consumption sensors with uncompromised performance regarding high resolution and long working distance compared to existing displacement sensing technologies.

CHAPTER 2

CHARACTERIZATION OF THE PIEZOTRONIC EFFECT IN VERTICAL ALIGNED CDSE NANOWIRES[33]

As aforementioned, exploring the vertical mode piezotronic effect in the individual nanowires will pave the way for future integration of nanowire sensor array devices. In addition, it would be interesting to explore this effect in other piezoelectric semiconductor materials so that coupling effect with other properties may be investigated. As an important II-VI group material, CdSe has been studied extensively on its quantum confinement and optoelectronic properties. Recently, one dimensional CdSe nanostructured materials have been reported for potential applications in light emitting devices[34], solar cells[35], photo detectors[36] and lasers[37]. Among them, Wurtzite structured CdSe nanowires also exhibit piezoelectricity due to its non-central symmetric crystal structure. Combined with its semi-conductive property, it becomes an attractive material for piezotronic study, since it will pave the way for future study of the coupling between piezotronic and optoelectronic effect.

2.1 Synthesis of vertically aligned CdSe NW arrays

The CdSe NW arrays were grown using Vapor-Liquid-Solid method on a mica substrate. The detailed processes are as below. First, freshly cleaved muscovite mica substrates (SPI, Grade V-5 research quality) were loaded into an electron beam evaporation system (Kurt J. Lesker, PVD75) for CdSe thin film deposition. After coated with 100nm CdSe thin film, the mica substrates were transferred to sputtering system

(*Cressington coating system, 308R***)** for platinum catalyst deposition. CdSe thin films and platinum particles are used as the barrier and catalysts, respectively. The nominal thickness of the catalyst was 0.3 nm. CdSe powder ***(****Alfa Aesar***,** 99.999% purity, metal basis) loaded in the molybdenum crucible was used as the evaporation material source. The growth was carried out in a typical thermal evaporation horizontal tube furnace where the mica substrate was placed downstream to collect the products. The furnace was then heated up to 750° C with H_2/Ar flow (30 sccm /120 sccm) to generate vapor for 20 min. The samples were taken out for characterizations after the system was cooled down to room temperature.

The morphological was performed by a field-emission scanning electron microscope (SEM, *LEO 1530*) system. Tilted-view images of the as-grown CdSe NWs with different lengths are presented in Figure 2.1a and b, showing that the length of the NWs varies from 200 nm to 4 µm, but the diameter remains constant. A low-magnification transmission electron microscopy (TEM, *JEOL-4000*) image is shown in Figure 2.1c, and the diameter of the NWs is a uniform 60 nm along the length. The corresponding high resolution TEM (HRTEM) image and the Selected Area Electron Diffraction (SAED) pattern indicates that the CdSe NW has a single crystal wurtzite structure and grows along the <0001> direction, as shown in Figure 1d and e, respectively.

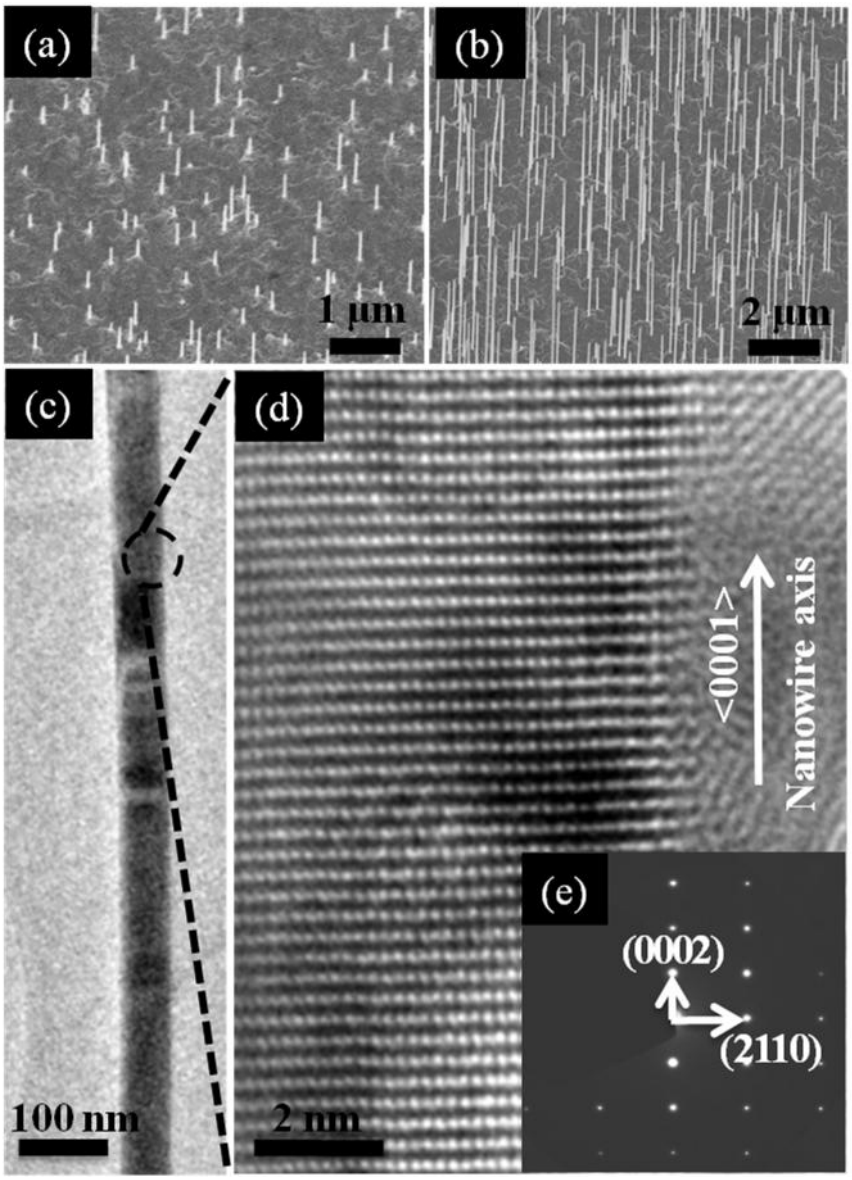

Figure 2.1 Vertically aligned CdSe NW array grown on the mica substrate. (a) Side view SEM images of the short (~ 200-500 nm) NWs and (b) long (~ 2-4 μm) NWs; (c) TEM image of a NW with low magnification; (d) High Resolution TEM (HRTEM) image of CdSe NW; (e) Corresponding selected-area electron diffraction (SEAD) pattern from the region indicated by dashed circle in image.

The wurtzite crystal structure of CdSe is illustrated in Figure 2.2: the red balls represent the Cd^{2+} cations and the gray balls represent the Se^{2-} anions. This structure is

composed of repeating tetrahedral units, where the Se^{2-} anions are located on the corners while the Cd^{2+} cations are in the center. The positive and negative charge centers overlap under strain-free conditions. Once a stress is applied along the c axis, the charge centers are relatively displaced, resulting in a dipole moment. A macroscopic piezopotential can be created along the NW by adding up all of the dipole moments of the unit cells.

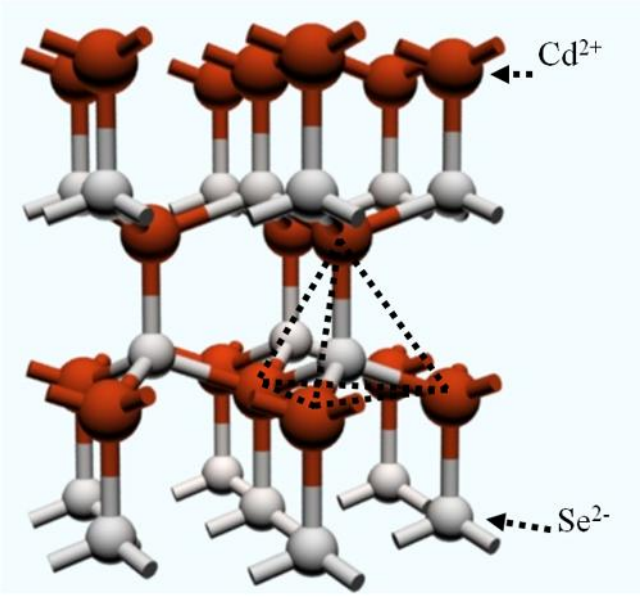

Figure 2.2 Schematic illustration of wurtzite crystal structure of CdSe.

The magnitude of the piezopotential depends on the deformation of the crystal, the doping concentration and the dielectric constant[14]. The distribution of the piezopotential along a NW under various forces was simulated in Comsol using the Lippman theory for doping free CdSe NWs. The parameters used for the simulation are shown in Table 2.1. Figure 2.3 shows the piezoelectric potential distribution when the NW is compressed by various normal forces. The top of the NW exhibits a negative

potential compared to the bottom. It can be shown that the amplitude of the negative potential increases with increased strain due to further separation of the charges in the crystal cells.

Table 2.1 The parameters used for the simulation of CdSe NW.

Parameter	Value
Length (nm)	250
Diameter (nm)	60
Piezoelectric Coupling Coefficients Matrix (C/m^2)	e_{31}=-0.16 e_{33}=0.347 e_{15}=-0.138
Elasticity Matrix (GPa)	C_{12}=46.1 C_{13}=74.9 C_{15}=39.3 C_{33}=81.7 C_{44}=13 C_{66}=14.3

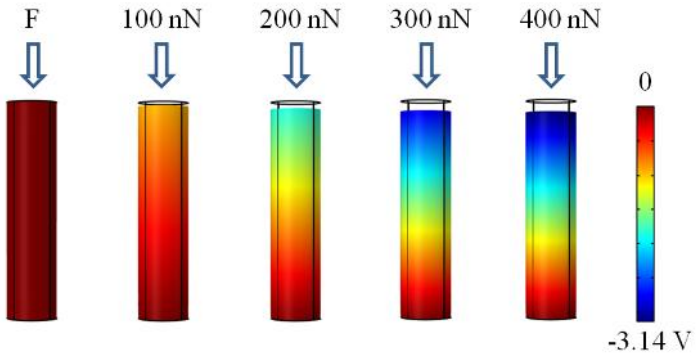

Figure 2.3 Piezopotential distributions under normal force ranging from 100 nN to 400 nN. Geometry of the NW used in the simulation is diameter D=60 nm, length L=250 nm.

2.2 Electrical property at Pt-CdSe interface modulated by longitudinal force

The characterization of the piezotronic effect was conducted by applying a normal force to the top of the CdSe NWs using an AFM probe (System: *Asylum Research MFP-3D,* Probe: *Olympus AC-240TM*). Figure 2.4a shows the schematic of the experimental set-up. The tips of the AFM probes have a Ti(5nm)/Pt(20nm) coating layer. Because of the difference between the work function of Pt (6.1 eV)[38] and the electron affinity of CdSe (4.95 eV)[39], a Schottky junction forms between the CdSe NW and Pt coated tip. The applied force was estimated as the product of probe spring constant, inverse optical lever sensitivity (InvOLS) and cantilever deflection (represented by voltage). During the measurement, firstly a topographic image of CdSe nanowires was obtained in tapping mode. Subsequently, the AFM tip was positioned on top of one CdSe NW and the electrical measurements were carried out. The magnitude of the force was kept constant by keeping the deflection set point during one measurement.

Since the bottom of the NW was connected to a CdSe thin film, to which an Ohmic contact was made using silver paste, it is reasonable to assume that the Schottky barrier formed at the Pt-CdSe junction dominates the I-V characteristics in both directions. The energy band diagrams in Figure 2.4b illustrates an elevated Schottky barrier due to a negative piezopotential induced by the compressive force. Figure 2.4c shows the experimental results of the I-V measurement under increasing applied forces, starting at 420 nN. In the beginning, the reverse current was very small while the

forward current started to increase from bias of 0.5 V, and reached 84 pA at a bias voltage of 2V, indicating a current rectifying phenomenon. As the force increased to 700 nN in increments of 70 nN, the forward bias decreased dramatically to 17 pA at a bias of 2V.

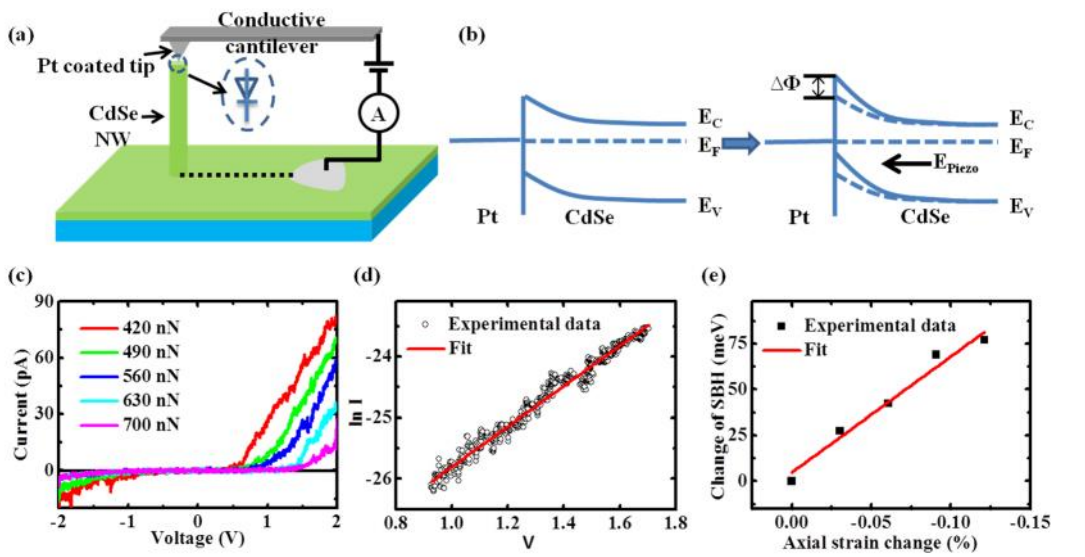

Figure 2.4 (a) Schematic for the piezotronic effect measurement experiment; (b) band diagram of the interface between Pt and CdSe (left) and the change of schottky barrier by the piezopotential; (c) I-V characteristics of a single CdSe NW measured by C-AFM under different applied forces; (d) Plot of *lnI* as a function of V; (e) calculated barrier height change from the measured I-V characteristics.

2.3 Theoretical discussion – Schottky barrier height modulated by stress/strain induced polarization

To evaluate the influence of the applied axial strain on the Schottky barrier of the CdSe NW, the SBH change was calculated according to the I-V characteristics. For the sake of simplicity, we assume an ideal Schottky diode by neglecting the shunt and

series resistance, and apply the thermionic current-voltage relationship described by equation 2.1:[40]

$$I_f = AA^{**}T^2 \exp(-\frac{¤_B}{k_B T})(\exp(\frac{qV_f}{nk_B T}) - 1) \quad (2.1)$$

where A is the area of the source Schottky barrier, A^{**} is the effective Richardson constant, T is the temperature, Φ_B is the SBH, k_B is the Boltzmann constant, q is the electron charge, V_f is the voltage drop on the forward biased Schottky diode, and n is the ideality factor .

To verify that eq. 2.1 can precisely describe the observed I-V characteristic, we plot ln*I* as a function of *V*, as given in Figure 2.4d. In this figure, the ln*I*-V curve fairly linear, which indicates that the thermionic emission-diffusion model is the dominant process in this experiment and the model can be applied to derive the SBH change from the I-V characteristics. Therefore, assuming that the change of A^{**} under strain is much smaller than the strain induced change in the SBH, we can calculate the change of the SBH by

$$\ln(I_f(£_1)/I_f(£_2)) \sim -\Delta¤_s/kT \quad (2.2)$$

As shown in Figure 2.4e, the SBH changes linearly with increased axial strain of the CdSe NW. The barrier height increased by 77.1 meV with strain change of 0.12%.

In the strain-gated piezotronic transistor demonstrated here, the gate electrode of the transistor is replaced by the internal crystal potential generated by strain, and the

control over the transported current is at the interface between the nanowire and the top or bottom electrode. It demonstrates the possibility of fabricating an array of transistors using individual vertical nanowires that can be controlled independently by the applied mechanical force/pressure over the top. Such a piezotronic transistor array is a new design of transistors and is likely to have important applications in high-resolution mapping of strain, force or pressure.

CHAPTER 3

CHARACTERIZATION OF THE PIEZOTRONIC EFFECT IN GaN NANOWIRES FOR TRANSVERSE FORCE SENSING[41]

In addition to longitudinal force, shear force is an important component to detect to fully resolve a force pattern. It is possible to integrate both longitudinal and share force sensing modes into vertically aligned nanowires that grow along c axis, as both modes can induce piezoelectric polarizations and the polarizations are dominating at different interfaces: longitudinal stress induced polarization is at top and bottom surface and transverse at side surfaces. Therefore, to demonstrate this potential, it is important to characterize the transverse mode piezotronic effect. In addition, we also extend the study of this effect to another functional material - Gallium Nitride (GaN). Compared to ZnO, GaN is more chemically stable and thus more resistant to environmental humidity. As an important binary III/V direct bandgap semiconductor material, GaN has attracted extensive research interest on bright light-emitting diodes, it will be intriguing in study its optoelectronic effect with its piezotronic effect.

3.1 AFM based experiment method to characterize GaN nanowires in bending

The n-type Si doped GaN NW array was synthesized by molecular beam epitaxy (MBE) on n-type Si [111] wafers[42]. The doping concentration can be tuned by varying the growth temperature. Figure 3.1a shows that the NWs are vertically aligned with a

uniform length of about 1 μm. From low magnification transmission electron microscopy (TEM) image (Figure 3.1b), the NW diameter is about 60 nm. A corresponding high resolution TEM (HRTEM) image and selected area electron diffraction pattern (SAED) show that the as-grown GaN NWs are single crystalline with a wurtzite structure, and a growth direction of <0001> (Figure 1c).

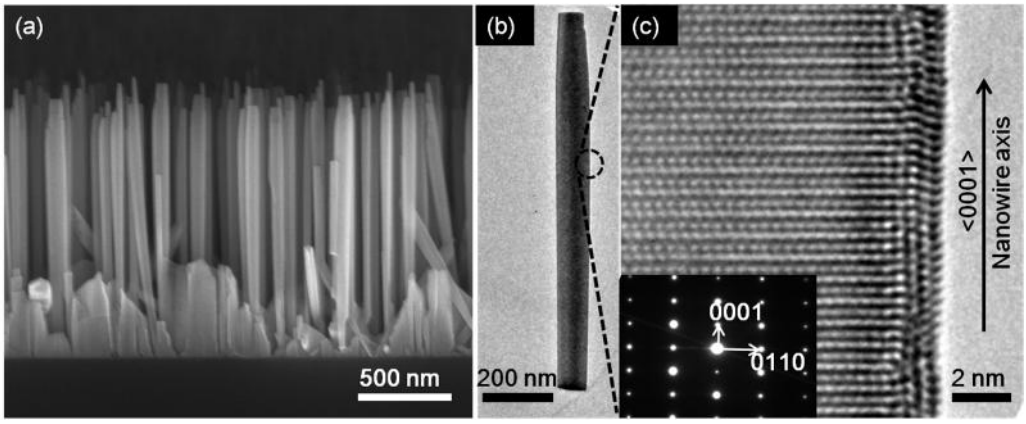

Figure 3.1 a) 90˚ tilted SEM view of the vertically aligned GaN NW array grown on Si substrate. b) Low magnification TEM image of a GaN NW. c) High resolution TEM image and corresponding SAED pattern (inset).

In order to simulate transverse force conditions, we applied a bending force to the free end of a single GaN NW using an atomic force microscope (AFM), as shown in Figure 3.2a. To precisely position and control the AFM tip to the side of a single NW, we used the following procedure: Firstly the NW array sample was cleaved and tilted 90°. Then, a tapping mode image of the edge of the sample was taken (Figure 3.2b). Lastly, the AFM tip was moved to the free end of a single NW using the AFM's closed loop piezo scanner.

In order to characterize the electric transport property under the different bending forces, the *I-V* characteristics of the NW were measured under varying bending forces. Three steps were applied to the experiments, as shown in Figure 3.2c. In the first step, the tip was engaged onto the free end of the NW with a pre-set force. The top curve shows the applied force during the whole process. The applied force was increased by further deflecting the AFM cantilever. Secondly, after the applied force reached a pre-set value, the force remained constant during the dwell stage and the electrical measurements were initiated. In this stage, a sweeping bias between -2 V and +2 V was applied between the NW and the tip as shown in the middle curve. The bottom curve shows the current response to the applied bias. After the *I-V* measurements were performed, the AFM tip was retracted from the NW.

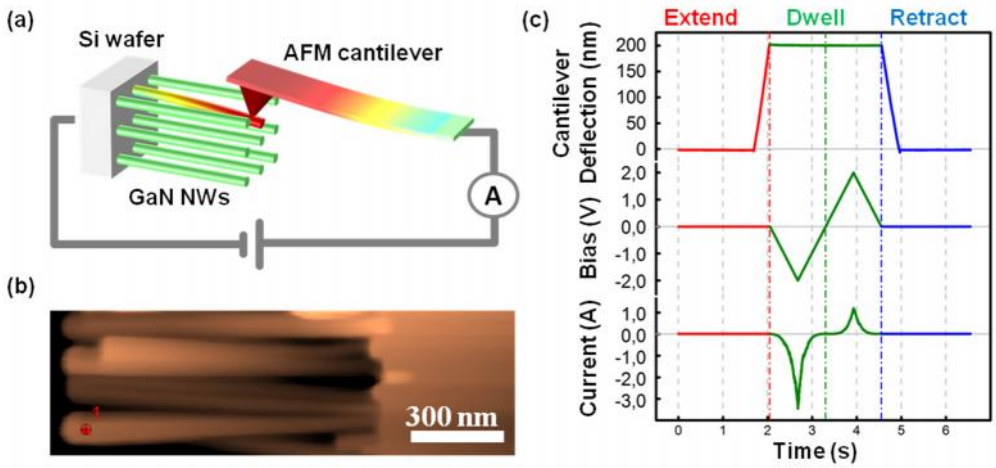

Figure 3.2 (a) Schematic of the AFM experimental setup. (b) AFM image of a 90° tilted GaN NW. The red mark on one of the NWs indicates the location of the AFM tip during the electrical measurement. (c) Illustration of the experiment process: from top to bottom, the cantilever deflection that is proportional to the

applied force on the GaN NW; a bias applied between the AFM tip and the sample; and the corresponding detected current.

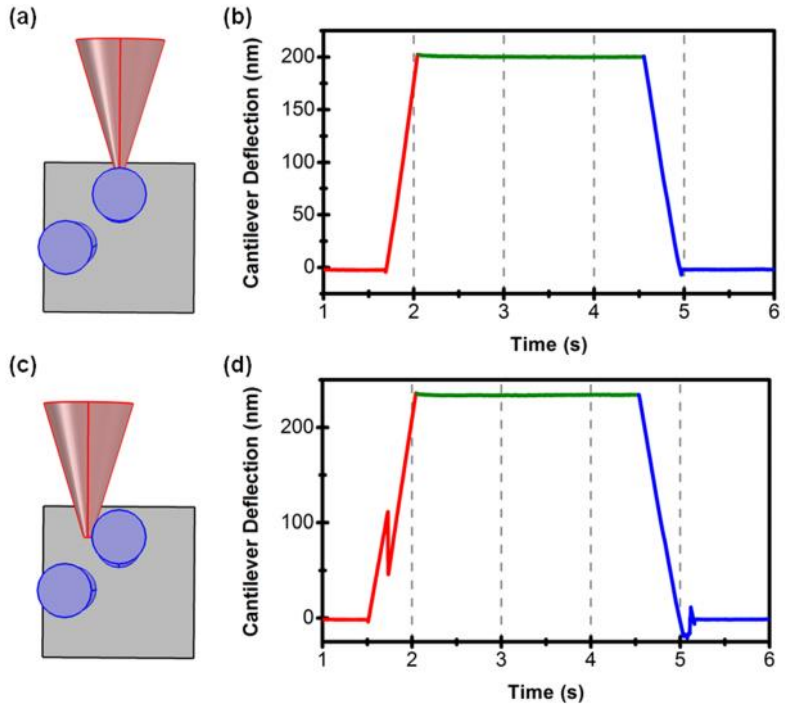

Figure 3.3 a) Schematic of the AFM tip touching a NW on the middle. b)) Illustration of a good experiment process: the NW does not slip on the edge of the NW, c) Schematic of the AFM tip which is slipping on the edge of a NW. d) Illustration of a bad experiment process: the NW slipped on the edge of the NW and then the cantilever deflection extend curve shows a discontinuity.

During both the force exertion stage and *I-V* measurement stages, any instabilities such as the tip sliding over the NW or external disturbances such as system drifting can be easily differentiated by monitoring the force *vs.* time curve in the extend and dwell stage. A stable contact between AFM tip and the NW during force increasing process (Figure 3.3a) should have the continuity of the cantilever deflection curve

(Figure 3.3b); On the contrary, an abrupt change (discontinuity) in the cantilever deflection curve (Figure 3.3d) indicate unstable process such as AFM tip sliding over one NW on to another, as illustrated in Figure 3.3c. Therefore, through this method, data obtained under unstable contact conditions are differentiated and ruled out.

3.2 Electrical property at the Pt-GaN interface modulated by transverse force

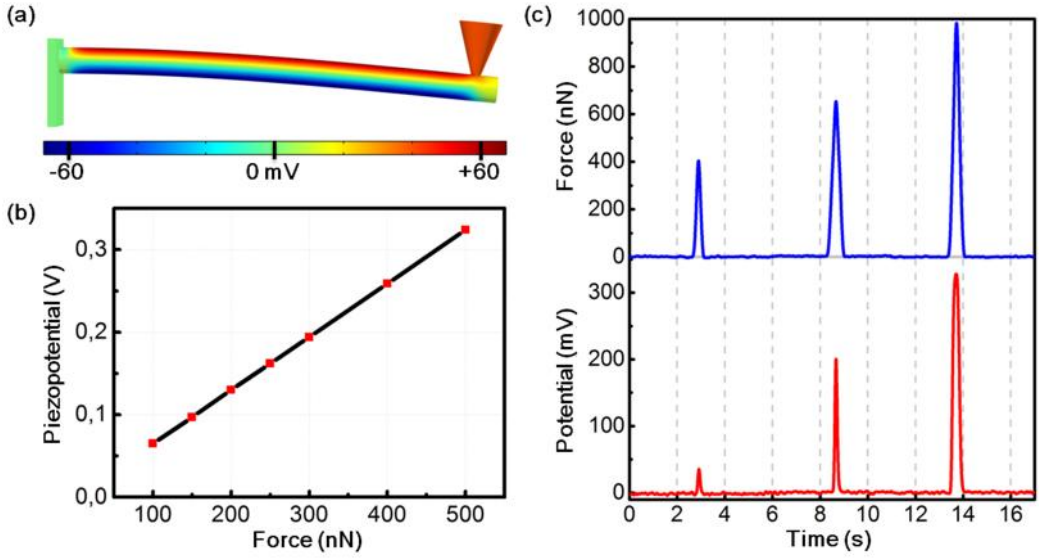

Figure 3.4 a) Finite element simulation of the potential distribution at the surface of a GaN NW when subjected to a transverse force. b) Positive piezoelectric potential generated in the NW as a function of the transverse force applied. The geometry of the GaN NW used in simulation is 1um in length, 60 nm in diameter. c) AFM measurements of the piezoelectric potential generated by a GaN NW under different bending forces.

Prior to the *I-V* measurements, finite element simulations were done, without considering the carrier concentration in the NW, to have a better understanding about

the process. The material constants of the GaN NW utilized in the simulation are, the symmetric elasticity matrix C: C_{11} = 390 GPa, C_{12} = 145 GPa, C_{13} = 106 GPa, C_{33} = 398 GPa, C_{44} = 105 GPa[43], the piezoelectric constants matrix e: e_{31} = -0.33 C/m^2, e_{33} = 0.65 C/m^2, e_{15} = -0.30 C/m[44], the relative dielectric constants matrix k: $k_{11} = k_{22} = k_{\perp}$ = 9.5, $k_{33} = k_{\parallel}$ = 10.4[45], and the density ρ = 6150 Kg m^{-3}. We assume that the NW grows vertically on the substrate. The free end of the NW is laterally pushed by an AFM tip with a force of 100nN. The length of the nanowire was set to be 1 um and the diameter was set to be 60 nm. When a transverse force was applied on the NW, the NW's top side is under tension while the bottom is under compression. The strain generates a piezoelectric potential in a Ga-polar NW as shown in Figure 3.4a. It represents the simulated piezopotential distribution of a GaN NW with a growth direction of [0001]. The color code represents the output piezopotential. The stretched side of the GaN NW exhibits a positive piezopotential with a magnitude of 0.063 V. The compressed side of the GaN NW exhibits a negative piezopotential with the same magnitude. This piezoelectric potential is proportional to the strain for small force under linear approximation, as illustrated in Figure 3.4b.

In order to verify the validity of the simulation results, we used the method described by Xin et al.[46] to measure the piezoelectric potential generated by the GaN NW using an AFM tip. As presented in Figure 3.4c, a positive piezoelectric potential was detected between the AFM tip and the sample and its magnitude increased with larger force, which is in agreement with the simulation.

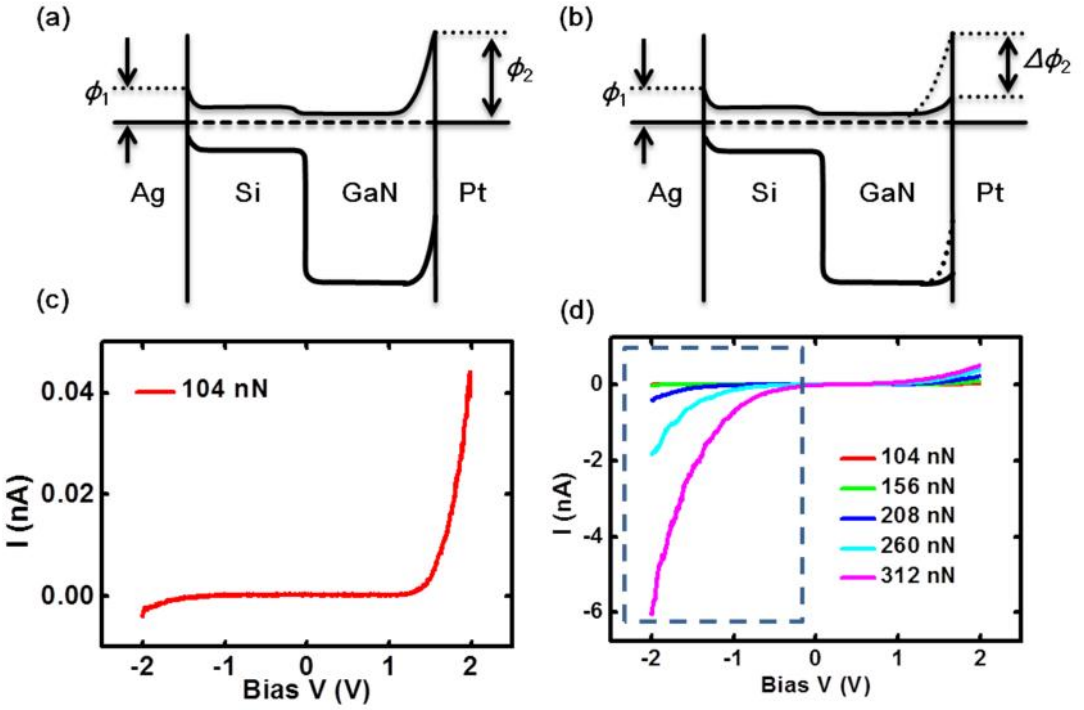

Figure 3.5 a) Energy band diagram of the electrical circuit, b) and its change with an external force induced piezopotential on GaN NWs. c) Experimentally measured *I-V* characteristics under a constant transverse force of 104 nN, and d) at different forces between 104 nN and 312 nN.

In the subsequent *I-V* measurements, there were two metal-semiconductor contacts in the circuit (Silver paste – Si substrate - GaN NW - Pt AFM tip). One was the contact between the Pt coated AFM tip and GaN NW, while the other was between the silver electrode and the Si wafer. The work functions of the two metals are higher than the corresponding semiconductors' electron affinities. As a result, both contacts are Schottky contacts with different barrier heights. The Schottky barrier height (SBH, Φ_B) of the Ag-Si contact is assumed to be much lower than that of the Pt-GaN one given that the work functions of Pt and Ag are 5.65 eV and 4.26 eV[47], respectively, and the

electron affinities of GaN and Si are 4.1 eV[48] and 4.05 eV, respectively. The heterojunction between GaN NW and Si is negligible due to the 0.05 eV difference in electron affinity and the small difference of the doping concentration[42]. The energy band diagram is shown in Figure 3.5a.

According to the piezotronic theory[6], a positive local piezo-potential would lower the SBH, as illustrated in Figure 3.5b, subsequently increasing the current flow through the NW. Due to the Ag-Si contact's opposite rectifying direction, the current flow from the Pt to the NW, defined as positive here, would be largely limited by the reversely biased Ag-Si Schottky contact, while current in the reverse direction, defined as negative here, will be dominated by the Pt-GaN Schottky contact. Therefore, by monitoring the negative current, a change in SBH of Pt-GaN contact can be derived, and the applied force can be quantified.

Experimental results are shown in Figure 3.5c and d. The current under negative bias dramatically increased as the force increased from 104 nN to 312 nN, which is qualitatively consistent with our simulation. The current change at 2V as a function of force was analyzed in both forward biased and reverse biased situations. As shown in Figure 3.6a, the current change linearly with the force under forward bias, while exponentially with the force under reverse bias. In addition, the relative change of current in forward bias is very small compared to the change in reverse bias, as indicated in Figure 3.6b. The significant difference between the forward and reverse bias cases shows that the contact is not the dominating factor for the current change; otherwise the

trends of the two curves would be in proportional with similar trends. Therefore, it is fair to explain that this asymmetric current change is mainly due to the piezotronic effect as the piezopotential reduces the SBH between the Pt coated AFM tip and the GaN NW. Under positive bias, the current was largely limited by the reversely biased Ag-GaN Schottky junction, and much less sensitive to the applied force.

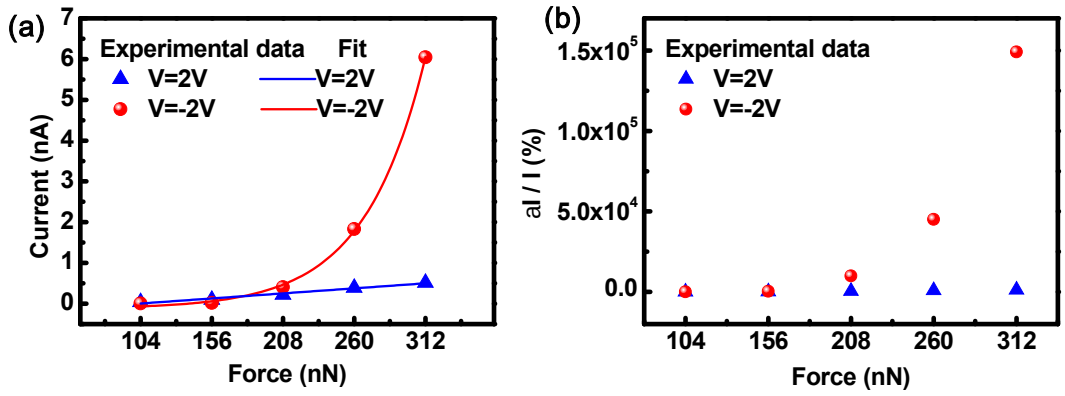

Figure 3.6 (a) Plot of measured current as a function of applied forces under forward bias (blue) and reverse bias (red) and their respective fitting curves. Red curve is an exponential fit, blue curve is a linear fit. (b) Plot of relative current change as a function of applied force.

To quantify the SBH change under the applied transverse force, we employed the classic Schottky models to derive the change in SBH (Φ_B) from the *I-V* curve. By considering the intermediate doping concentrations of the GaN NWs and that all measurements were taken at room temperature, the thermionic-emission-diffusion (TED) model and thermonic-field-emission (TFE) models are most suitable for analyzing our experimental results[40]. In the TED and TFE models, ln *I* is approximately

proportional to $V^{1/4}$ and V, respectively. By plotting both ln$I$-$V^{1/4}$ and ln$I$-V curves, we found that the ln$I$-V is closer to a linear relationship, as shown in Figure 3.7 and Table 3.1, indicating that the thermionic field emission process was dominant in our experiment.

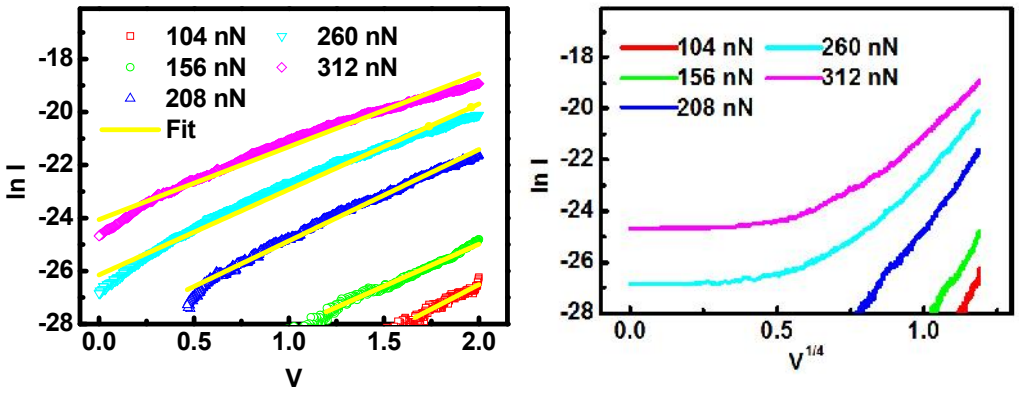

Figure 3.7 Comparison of ln$I$-V (left) and lnI-$V^{1/4}$ curve (right).

Table 3.1 Goodness of linear fitting of experimental ln$I$-F data.

Force (nN)	104	156	208	260	312
Fit Slope	3.44495	3.17552	3.69889	3.22496	2.74963
Standard error	0.01029	0.01603	0.06906	0.01128	0.01229
Adjusted R-square	0.99153	0.98738	0.93177	0.98496	0.98166

The reversely biased current is described in the TFE model by:

$$\mathrm{I} = \frac{SA^{**}T}{k}\sqrt{®E_{00}[q(V-\text{，})+\frac{¤_B}{\cosh^2(E_{00}/kT)}}]\exp(\frac{-¤_B}{E_{00}\coth(E_{00}/kT)})\exp((\frac{1}{kT}-\frac{1}{E_{00}\coth(E_{00}/kT)})qV)$$

(3.1)

where S is the area of the Schottky barrier, A^{**} is the effective Richardson constant, T is the temperature, k is Boltzmann constant, q is the electron charge, f is the distance between the Fermi energy to the bottom of the conduction band, E_{00} is the characteristic energy determined by the properties of semiconductor material:

$$E_{00} = \frac{qh}{4®}\sqrt{\frac{N_d}{m^*£}} \tag{3.2}$$

where h is the Planck's constant, N_d is the doping/impurity concentration, m^* is the tunneling electron's effective mass, and $\mathcal{E}$ is the dielectric constant of the NW. Since the square root of V is negligible compared to the exponential term, under the safe assumption that the change in A^{**} under strain is much smaller than the change in the SBH, $\Delta\Phi_B$ can be approximated using the following expression:

$$\Delta¤_{\mathrm{B}} \approx -E_{00}\coth(E_{00}/kT) \ \ *\ln(I/I_0) \tag{3.3}$$

Value of parameters used in derivation of the change of Schottky barrier height (SBH) $\Delta\Phi_B$ from experimental data are listed in Table 3.2.

Table 3.2 The parameters used in estimate the Schottky barrier change[48].

Symbol	Parameters	Value	Unit
q	Electron charge	$1.602\ 176\ 565 \times 10^{-19}$	C
h	Planck constant	$6.626\ 069\ 57 \times 10^{-34}$	J·s
N_d	Doping concentration of GaN NWs	5×10^{17}	cm^{-3}
m^*	Effective electron mass in GaN ($m^*=0.2\ m_0$).	$1.82469145 \times 10^{-31}$	kg
$\mathcal{E}$	Dielectric constant of GaN ($\mathcal{E}=8.9\ \mathcal{E}_0$).	$7.88022715713\times 10^{-11}$	$F\cdot m^{-1}$
k	Boltzmann constant	$1.380\ 6488 \times 10^{-23}$	$J\cdot K^{-1}$
T	Temperature	300	K
E_{00}	Characteristic energy	9.84×10^{-3}	eV

Based on this method, we can plot $\Delta\Phi_B$ as a function of applied forces in Figure 3.8.

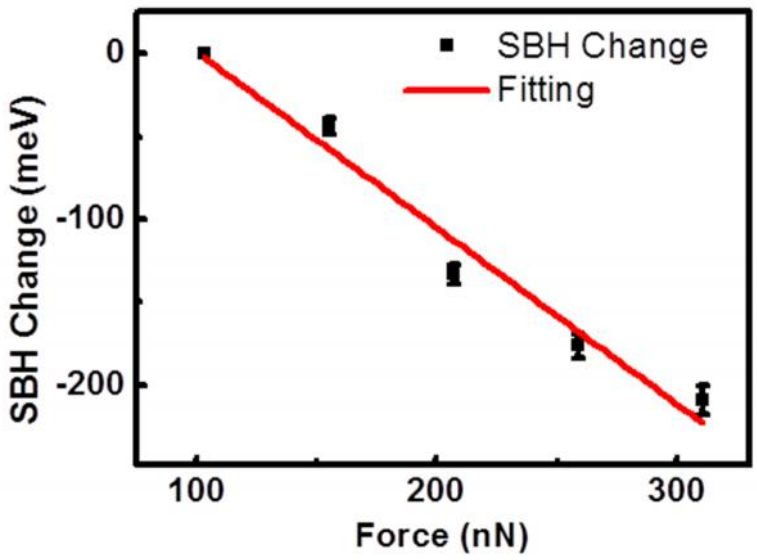

Figure 3.8 Calculated SBH change as a function of the applied force.

3.3 Transverse force sensitivity - theoretical model and experimental results

The observed linear relationship is consistent with the piezotronic model described as follows. According to previous reports about the theory of piezotronics, the induced SBH change is linearly dependent on the piezoelectric charge density ρ_{piezo}:[6]

$$\Delta\text{¤}_B \approx -\frac{q\,\circ_{piezo} W_{piezo}^2}{2\text{£}} \tag{3.4}$$

where W_{piezo} is the width of the piezoelectric polarization charge layer. Under bending, the piezocharge density depends on the NW's electrical and mechanical properties, geometry and the applied force, as described in eq.3.5,

$$\circ_{piezo} = F\frac{r}{I_m E}[2(1+\neg)e_{15} + 2\neg e_{31} - e_{33}] \tag{3.5}$$

where F is the applied transverse force, r is the NW radius , I_m is the momentum, E is the NW's Young's modulus, v is the Poisson ratio and e_{ij} are the piezoelectric coefficients. From equations 3.4 to 3.6, the transverse force could be linearly related to the change in the natural logarithm of the detected current $\Delta\ln I$,

$$F \propto \circ_{piezo} \propto \Delta\text{¤}_B \propto \Delta\ln I \tag{3.6}$$

Figure 3.9 shows the sensitivity and response time characterized by AFM. First, a current change under certain working bias (V = -2 V in this case), was recorded when increasing the bending force by a step of 16 nN. As shown in Figure 3.9a, the corresponding current, which is presented in semi-log form, increased exponentially

with applied force, consistent with the simulation and model stated above. Due to the exponential relationship between the current and force, the NW has different sensitivities in different force ranges, where the sensitivity S_I is defined as $\Delta I/\Delta F$. In lower forces range (16~32 nN), the sensitivity is about 0.5 pA/nN; while for larger forces range (64~80 nN), the sensitivity is about 2 pA/nN. From Figure 10a, since current change with 16 nN force increase can be clearly differentiated, it is fair to claim that the force resolution is better than 16 nN.

During this process, current was also influenced by the change of contact area of the AFM tip and the GaN NW. For simplicity, the tip–nanowire contact can be modeled as a sphere indenting a flat surface according to the Derjaguin–Muller–Toporov (DMT) model[49]. The contact area S can be given by:

$$S = ®[R*(F + |F_{adh}|)/E]^{2/3} \quad (3.7)$$

where R is the AFM tip radius (20 nm), E is the effective Young's modulus of the tip, F is the loading force, and F_{adh} is the tip–sample adhesion force which is experimentally determined to be 10 nN. As shown in Figure 3.10, the change of calculated contact area as a function of applied forces as applied force is negligible compared to the change of the measured current.

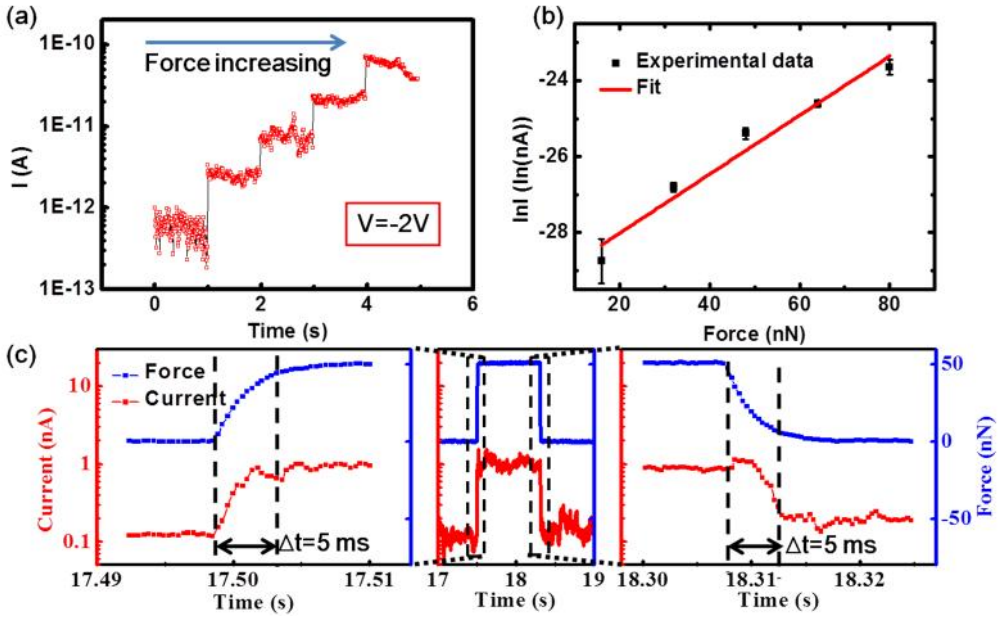

Figure 3.9 (a) Under constant applied voltage, the current passing through the GaN NW increased step-by-step as the applied force increased. (b) ln*I*-*F* curve demonstrating a linear relation between ln*I* and applied force. (c) Time response of the current change in response to the increased force (left) and deceased force (right).

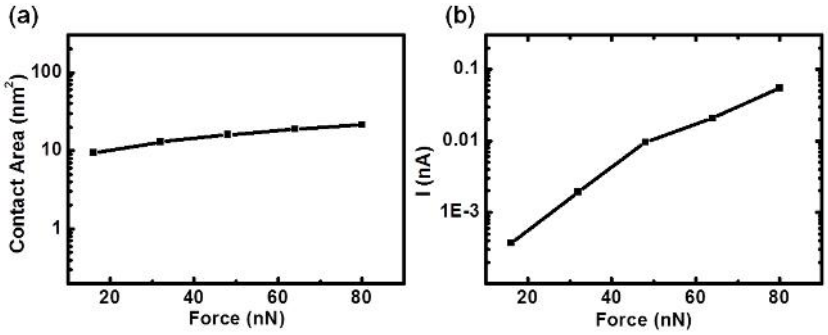

Figure 3.10 (a) Calculated contact area as a function of applied force. (b) Measured current as a function of applied force.

For practical applications, a sensor with a linear relationship between the input and output is preferred. Therefore, in our case, the ln*I* can be used as a metric to linearly represent the applied force. From the ln*I*-*F* fitting line in figure 3.9b, the sensitivity S_e defined to be $\Delta(\ln I)/\Delta F$ is calculated to be 1.24±0.13 lnA/nN by linear fitting. The response time was monitored by maximizing the sampling rate of the signal input channels of the AFM system. From Figure 3.9c, the current responds very well to the change in force even for time intervals as low as 5 ms, showing there is no remarkable delay in response at frequencies lower than 200 Hz. In the piezotronic transduction process, the strain induced carrier redistribution and Schottky barrier change is much faster than mechanical deformation.

The results show that GaN NWs can be used to transduce a shear/bending force into a dramatic current change through the NW due to the piezotronic effect. Owing to the local piezopotential generated by the applied force, the barrier height of the Schottky contact between the GaN NW and the Platinum AFM tip can be modulated. Using this transduction mechanism, the transverse force can be correlated to the natural logarithm of the current. Our results indicate that the force sensitivity is about 1.24±0.13 lnA/nN, and a force resolution of at least 16 nN is demonstrated. The Nano-Newton sensitivity in transverse sensing mode, combined with vertical mode demonstrated in Chapter 2, shed light onto the potential for piezoelectric semiconductor NWs to be used as building blocks for micro/nano force sensor arrays and high spatial resolution artificial skin.

CHAPTER 4

IN-SITU CHARACTERIZATION OF TRIBOELECTRIFICATION [50]

4.1 Existing characterization methods

Although the triboelectrification effect is known for thousands of years, a fundamental understanding about it is rather limited. The difficulties in studying it arise, in part, from the complexity of the phenomena, and in part, from lack of standard instrumentation and procedures for accurately controlling the contact electrification process and quantifying contact charging. The existing approaches use macro scale apparatuses to generate contact electrification and then measure the charge through surface electrostatic force[28], charge induction[21, 51], or surface potential[29]. One example of existing characterization methods is a rolling sphere tool that can be used to investigate the contact electrification between metal and polymers[21, 51]. As shown in Figure 4.1a, the working principle is to employ cyclically changing magnetic field to drive metallic spheres rolling on surfaces of polymers and measure the transferred charge on the spheres per circle through electrostatic induction in a metal slot underneath the polymers. It can be used for qualitative study of the kinetics of contact electrification (Figure 4.1b) generated by metallic spheres rolling on surfaces of polymers and the effects of modification of the functional groups present on the surface, and of surface moisture[21, 51]. However, because theses triboelectric characterization

methods are based on macro scale experimental setups, which measures the averaged tribo-charge transfer process, it hardly achieves a quantitative characterization of the process occurred at the interface.

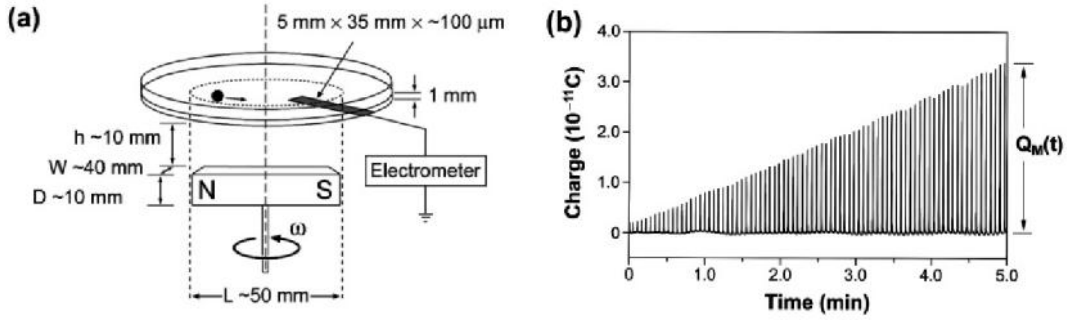

Figure 4.1 (a) Schematic of a Rolling Sphere Tool. (b) Measured charge accumulation on the sphere as a function of rolling time[51].

4.2 SPM based methods for in-situ quantitative characterization

Here an *in-situ* method was demonstrated to quantitatively characterize the triboelectrification at nano-scale *via* a combination of contact-mode AFM and scanning Kevin probe microscopy (SKPM). Systematical characterizations of the triboelectrification were realized including triboelectric charge distribution, multi-friction effect, as well as the subsequent charge diffusion on the dielectric surface. The design for the in-situ triboelectric characterization is illustrated in Figure 4.2a and Figure 4.2b. First, the AFM was operated in contact mode under a normal contact force of 120 nN to induce a friction pattern of 4×4 μm^2 area on a silicon oxide film (Figure 4.2a). Subsequently the surface topography and potential of the rubbed area were characterized *in-situ* in the scanning Kelvin potential microscopy (SKPM) mode (Figure 4.2b) with the underlying Si wafer grounded. Positive and negative charges can

be transferred to the SiO_2 surface through triboelectrification using Si-based probes with and without Pt coating, respectively. As shown in Figure. 4.2c and 4.2d, there is no detectable topographic change but a clear contrast in the surface potential images between the rubbed and intact areas. Figure 4.2e illustrates the 3D potential distribution in a 20×20 μm^2 surface area. As shown from the cross section profile (Figure 4.2g), the potential of the rubbed area is 0.167 V lower than that of the intact area, suggesting that excess negative charges transferred by rubbing lowered the surface potential of the central area.

To quantify the triboelectric charge density, the relationship between the surface charge density and the measured potential from SKPM were investigated. The principle of the SKPM is to match the probe bias V_{DC} with the contact potential difference between the sample and the probe V_{CPD} by nullifying the vibration of the probe, which is initially driven by the electrostatic force F_{ES} induced on the AFM probe, as described in Eq. 4.1[52]:

$$F_{ES} = -\frac{\partial C_t}{\partial z}\{\frac{1}{2}[(V_{DC} - V_{CPD})^2 + \frac{1}{2}V_{AC}^2] + (V_{DC} - V_{CPD}) \cdot V_{AC} \sin(\mu t) - \frac{1}{4}V_{AC}^2 \cos(2\mu t)\} \quad (4.1)$$

where C_t, z, V_{AC} and t are the equivalent capacitance between the tip and sample, the tip-sample distance, the magnitude of AC voltage applied to the probe, and the time, respectively.

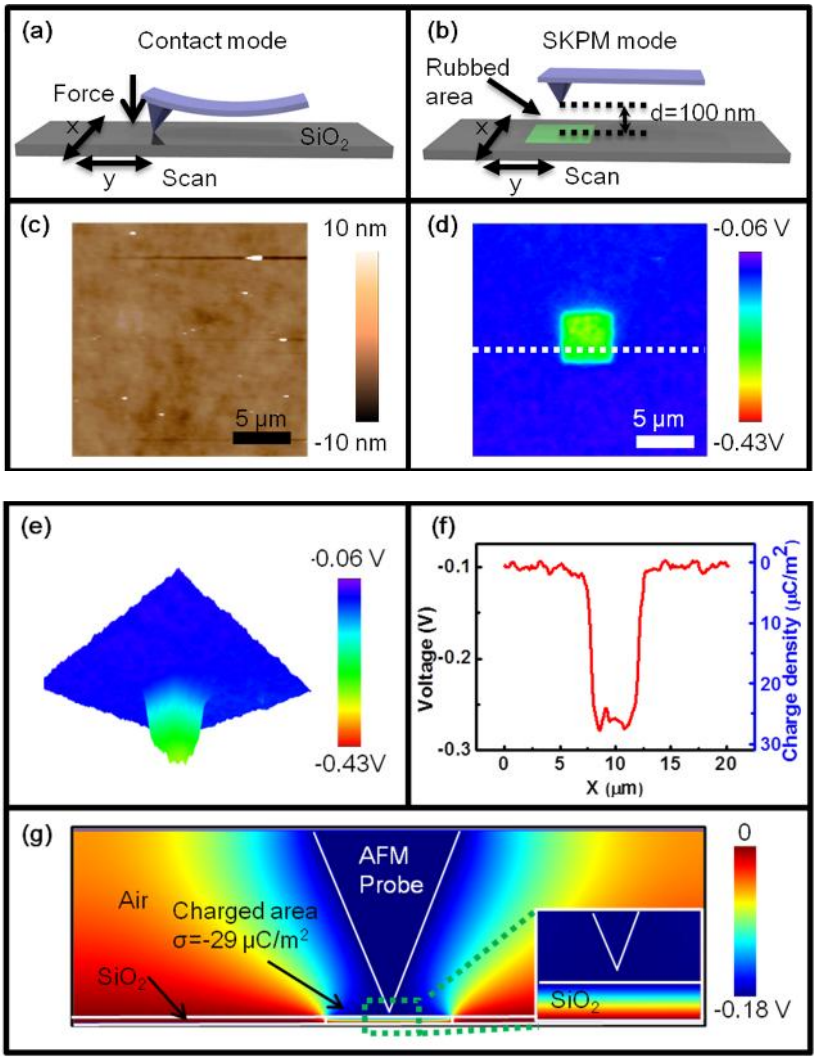

Figure 4.2 Schematic illustration of the experiments based on AFM. (a) triboelectric charge generation by friction between AFM probe and SiO_2 (b) subsequent surface potential characterization in the SKPM mode. (c) AFM topography of SKPM surface potential image (d) AFM topography of a larger area on SiO_2. The dashed line corresponds to the profile in (f). (e) 3D image of the measured surface potential profile. (f) Cross section profile of the potential distribution. (g) Simulated electric potential distribution in vertical direction under the condition when surface potential was measured in SKPM. Parameters used in

simulation: the apex angle of the AFM probe was set to 35˚ with a tip radius of 10 nm, and had potential of -0.168 V; the center 4 μm area on top surface of SiO_2 had surface charges with density of -29 μC/m^2 and the bottom surface of SiO_2 was grounded. The inset is an enlarged picture of the tip area.

The contact potential difference V_{CPD} is generally determined by two components: the effective work function of two materials and the electrostatic potential difference. The former component depends on the surface properties of the two materials, and the latter one is determined by the bias and surface charges of the sample[52]. Since the work function difference is almost the same across the measured surface, the potential contrast between the rubbed area and the intact area ΔV should be determined by the triboelectric charge induced potential change. The charge induced SiO_2 surface potential change ΔV can be correlated to the surface charge density σ using a parallel capacitor model, as given in Eq. 4.2, since the scale of the charged area (4 μm) is much larger than the thickness of the SiO_2 film (200 nm).

$$\pm = \frac{\Delta V \varepsilon_0 \varepsilon_{SiO_2}}{t_{SiO_2}} \tag{4.2}$$

where ε_0 is the vacuum dielectric constant, ε_{SiO2}, t_{SiO2} are the relative dielectric constant and thickness of SiO_2, respectively.

In the case of ΔV = -0.167 V, as shown in Figure 4.2f, σ is calculated to be -29 μC/m^2. To verify the accuracy of the simplified model, we carried out a 2D numerical calculation for the potential distribution with the surface charge density of -29 μC/m^2

and the presence of the AFM probe. When the probe bias is set at -0.168 V, there is no potential gradient between the surface of charged area and the AFM probe, which indicates the electrostatic force on the probe is nullified. This simulated bias value agrees very well with our measured -0.167 V.

4.3 Multi-friction effect on triboelectric charge transfer

Benefited from the capability of controlled charge transferring and *in-situ* measurement, the method as described above can be used to investigate the multi-friction effect on the triboelectric charge transfer at the interface. In this experiment, the SiO_2 was rubbed for multiple cycles at the same area with constant contact force. The corresponding SKPM images after each friction cycle are shown in Figure 12a and the extracted potential profiles are presented in Figure 12b. Within eight cycles of friction, the magnitude of the potential increased from 0.1 V to 0.7 V at a slowing rate.

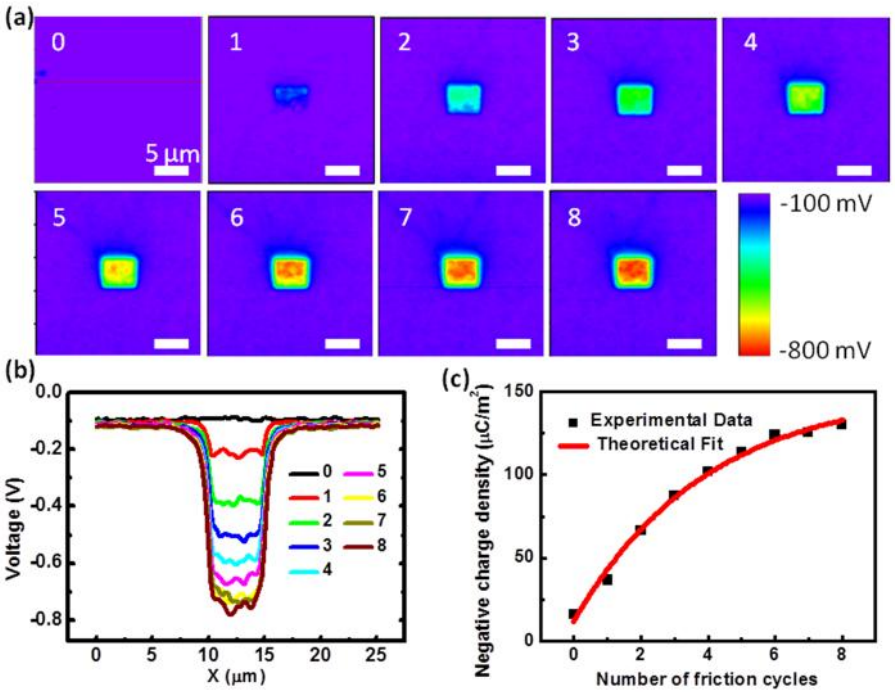

Figure 4.3 Triboelectric charge accumulation on the SiO_2 surface with the increase of the number of repeated rubbing at the same area. (a) Series of surface potential images taken in the same area from intact status to the one after 8^{th} rubbing cycles, and (b) their corresponding potential profiles. (c) Derived surface charge density as a function of the number of friction cycles, and our fit based on charge accumulation theory described in equation 4.4.

To quantify this process, the surface charge density was calculated according to Eq. (4.2). As shown in Figure 4.3c, there is a clear trend for the surface charge accumulation and saturation process. As in our experiment, the triboelectric process on the SiO_2 surface is considered as the cases of a metal-insulator. The mechanisms is mainly explained by the "effective work function" assumption in previous report, and the nature of the transfer can either be electron transfer, ion transfer or even material transfer[53]. Regardless of the nature of the transfer, the amount of charges transferred in each contacting cycle is related to the difference in the effective work function of metal/semiconductor and the insulator, $\Delta\varphi$, and the absolute value of $\Delta\varphi$ decreases with charge accumulating on the dielectric surface. When $\Delta\varphi = 0$, the triboelectric charges on the SiO_2 surface reach saturation. Thus, here we built a phenomenological model according to this proposed mechanism to fit our experimental result. Similar to the model for small particle charging, the quantity of charges transferred each time is assumed to be proportional to the potential difference between the AFM probe and the SiO_2 surface. This potential difference consists of the work function difference between

the two contacting materials V_c as well as the image charge potential V_e induced by existing charges on SiO_2 surface. V_c is a fixed value that only depends on material property, and V_e is proportional to the amount of existing charges. Thus, the overall charge transfer in each cycle is described by Eq. 4.3

$$\frac{d\pm}{dn} = kV_c - pV_e\pm \tag{4.3}$$

where σ is the accumulated surface charge density, n is the number of friction cycles, k is considered as charging efficiency coefficient, and p is considered as charging impedance coefficient. The boundary condition for equation 4.3 is as follows: σ_0 is the surface charge density before triboelectric process (e.g., at $n = 0$), and σ_∞ the saturate charge density after infinite numbers of cycles of friction. The relationship between σ and n is then obtained as shown in Eq. 4.4.

$$\pm = \pm_0 \exp(-\frac{n}{n_0}) + \pm_\infty \{1 - \exp(-\frac{n}{n_0})\} \tag{4.4}$$

where $n_0 = \frac{1}{pV_e}$ is the saturation constant that controls the speed of charge saturation, and $\pm_\infty = \frac{kV_c}{pV_e}$. The equation fits the experimental data very well, as shown in Figure 4.3c. The constants were extracted from the fitting: σ_0 = (-12 ± 3) μC/m^2, σ_∞ = (-150 ± 8) μC/m^2, n_0 = 3.9 ± 0.5. The adjusted R^2 of this fitting is 0.9911, suggesting a fairly good fit.

Similar charge accumulation behavior was also observed in the experiment of rubbing Pt coated probe on SiO_2 film. Within 40 cycles of friction, the estimated charge

density increased from 0 to 101 μC/m^2, but the surface charge density reaches saturation after n > 20. Figure 4.4 shows the estimated charge density after each cycle of friction, and a fit based on the charge accumulation theory described in equation (4.4). For this fit, R^2 = 0.94511, σ_0 = (-2 ± 5) μC/m^2, σ_∞ = (105 ± 6) μC/m^2, n_0 = 8.4 ± 1.3.

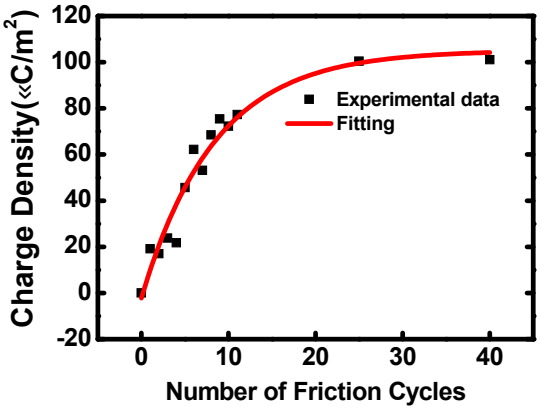

Figure 4.4 Estimated surface charge density as a function of the number of friction cycles for negative charge, and a fit based on charge accumulation theory

4.4 Surface diffusion of tribo-charge and quantification of its coefficient

Taking advantage of the nanometer resolution of AFM and SKPM, we are able to gain some insight on the migrating process of the triboelectric charges by monitoring the surface potential distribution within a time period after one cycle of triboelectrification. In our demonstrating experiment, an AFM tip firstly scanned over a 4×4 μm^2 area of SiO_2 surface in contact mode with a normal contact force of 120 nN to induce the triboelectric charges. The surface potential distribution was then monitored by SKPM every 12 min. Take the diffusion of the positive charge on SiO_2 rubbed by Pt tip as an example, as presented in Figure 4.5a, with the time changes from

0 to 84 min, the charged area becomes larger, and the peak voltage contrast becomes smaller. From the profiles of the same cross section of each image as shown in Figure 4.5c, the peak of the potential decreases from 0.4 V to -0.06 V and the half width at full maximum of the potential distribution profile increases from 5.1 to 8.6 μm, indicating the diffusion of surface charges to adjacent area.

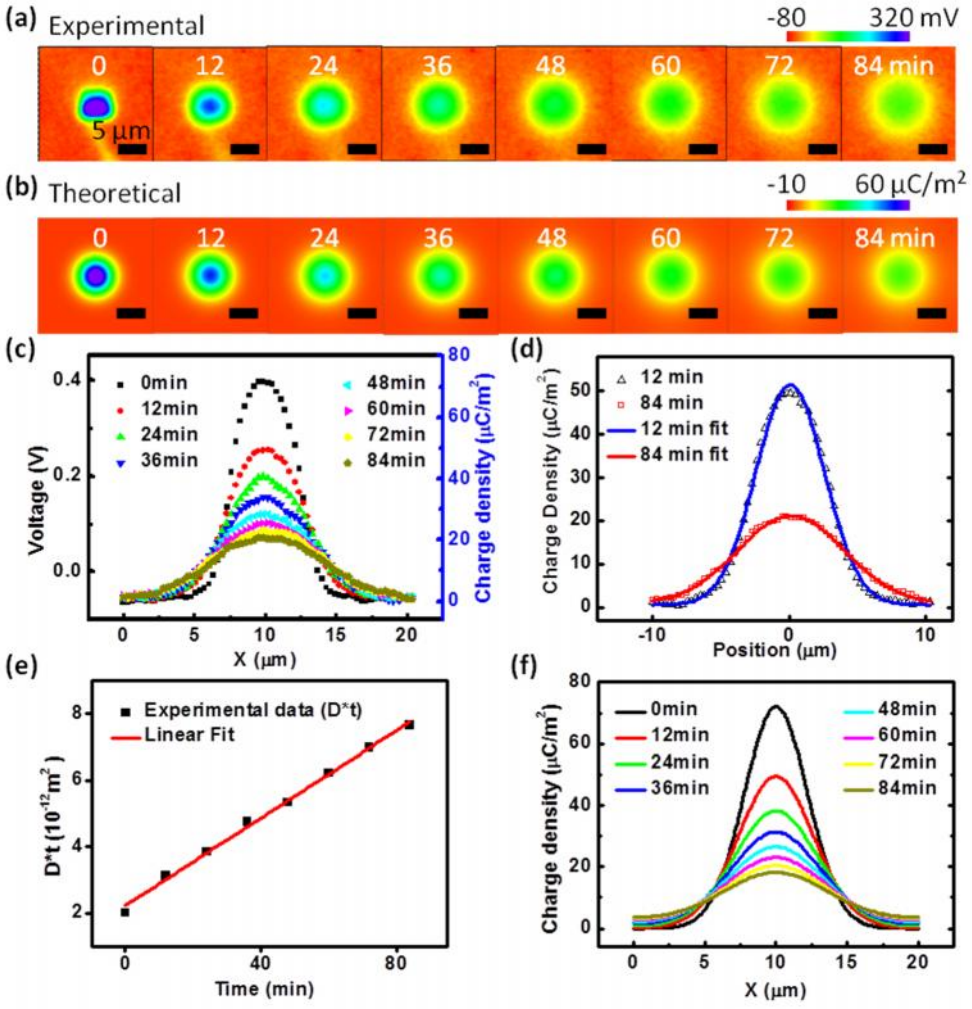

Figure 4.5 Charge diffusion over time. (a) Series of images of surface potential distribution as a function of time after the triboelectrification. (b) COMSOL simulation of surface charge density distribution. Initial charge density

was set to be a Gaussian distribution: 4.5×10^{14} exp[$-1.2\times10^{11}(x^2 + y^2)$], and diffusion coefficient to be 1.10×10^{-15} m^2/s. (c) the cross sections of the series of images in (a). (d) 1D Gaussian fit of the surface charge distribution at 12 min (blue) and 84 (red) min, respectively. Time constant (D^*t) can be derived from this fitting. (e) Time constant at different time and its linear fitting. The slope indicate diffusion coefficient. (f) The profiles of series of surface charge distribution images in (b).

Charges diffuse laterally on the surface in two-dimension as well as vertically into the bulk[54]. Here we assume that the surface diffusion rate is much higher than bulk diffusion. This is a reasonable approximation; otherwise most of the charges would have leaked into the bottom electrode rather than spreading over the surface because the characteristic length of the diffusion on the surface (about 3 μm) is much larger than the thickness of the SiO_2 (200 nm). Therefore, we employ the model for a two-dimensional diffusion to estimate the surface charge diffusion coefficient on SiO_2 on an unbounded uniform surface from a point source (x_0, y_0) from time t_0, as described in Eq. 4.5:[55]

$$\pm(x, y, t) = \frac{A}{t - t_0}\exp[-\frac{(x - x_0)^2 + (y - y_0)^2}{4D(t - t_0)}] \quad (4.5)$$

where $\sigma(x, y, t)$ is the surface charge density of point (x, y) at time t, A is the magnitude constant, and D is the isotropic diffusion coefficient on the surface. To extract diffusion coefficient from experimental data by equation (4.5), each set of data

at a cross section of $y = y_0$ at a specific time t_n was first fit with Gaussian distribution function $f_n(x)$:

$$f_n(x) = C_n \exp[-\frac{(x - x_0)^2}{2w_n^2}] \tag{4.6}$$

where C_n is the magnitude constant for $f_n(x)$, w_n is the distribution width of the Gaussian function, as shown in fig. 3d. As a further analysis, comparing equation (4.6) with equation (4.5), the following relationship is revealed.

$$D(t_n - t_0) = \frac{1}{2} w_n^2 \tag{4.7}$$

By fitting the eight groups of data at different diffusing time (as illustrated in Figure 4.5c), a $\frac{1}{2}w^2$ vs t curve is given, where D is the slope of the curve. From the fitting, D= (1.10±0.03)×10^{-15} m^2/s was obtained with R^2 = 0.9953. With this estimated diffusion coefficient, the charge distribution with time was simulated using the finite element method (COMSOL), as shown in Figures 4.5b and 4.5f, which matches very well to the experimental data.

Using the same method, the negative surface charge diffusion coefficient on the SiO_2 was also investigated. During the experiment, a Si-based AFM probe without Pt coating was firstly scanned three times consecutively over a 4×4 μm^2 area of SiO_2 surface in contact mode with a normal contact force of 120 nN to induce the triboelectric charges. The surface potential distribution was then monitored by SKPM every 12 min. Figure 4.6 a shows the profiles of surface charge density at a cross section

in each SKPM image taken from 0 min to 84 min. Compared to the positive charge diffusion shown in Figure 4.5c, the negative charged area shows a similar trend but changes slower. Further theoretical fit based on 2D diffusion model, as shown in Figure 4.6 b, confirms that the diffusion coefficient for negative charge, $D_n = 0.19 \times 10^{-15}$ m^2s^{-1}, which is less than one fifth of the estimated positive charge diffusion coefficient $D=1.10\times10^{-15}$ m^2s^{-1}.

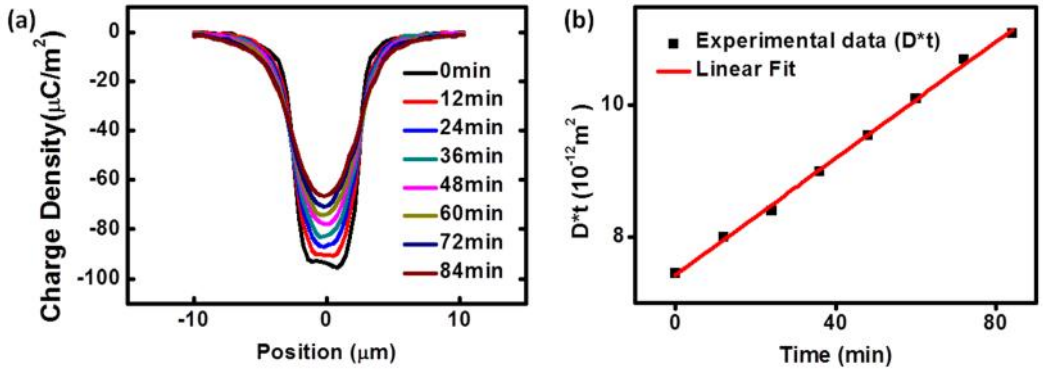

Figure 4.6 (a) Spreading of charge density profile for a negative triboelectrification process as a function of time. (b) Time constant at different time and its linear fitting for the negative charges. The slope indicates the diffusion coefficient. For this fitting, $R^2 = 0.9980$

The significant difference in the surface diffusion coefficients (more than 5 times higher for positive charges than for negative charges) may be related to difference in charge carriers and the structure of the surface.

4.5 Nano-patterning of surface charge via triboelectrification

With a precise position control, the AFM tip induced triboelectrification can also be used for patterning of surface charges at nanoscale. The polarity of the written

charges could be controlled by purposely choosing different probe materials. As demonstrated in Figure 4.7, both negative (a, b and c) and positive charges (d, e and f) can be written on the SiO_2 surface by using Si-based probes with and without Pt coating, respectively. The surface charges are successfully patterned while the topography of the area was unchanged, which shows promising potential for directed self-assembly of charged nanostructures for nanoelectronic devices[56].

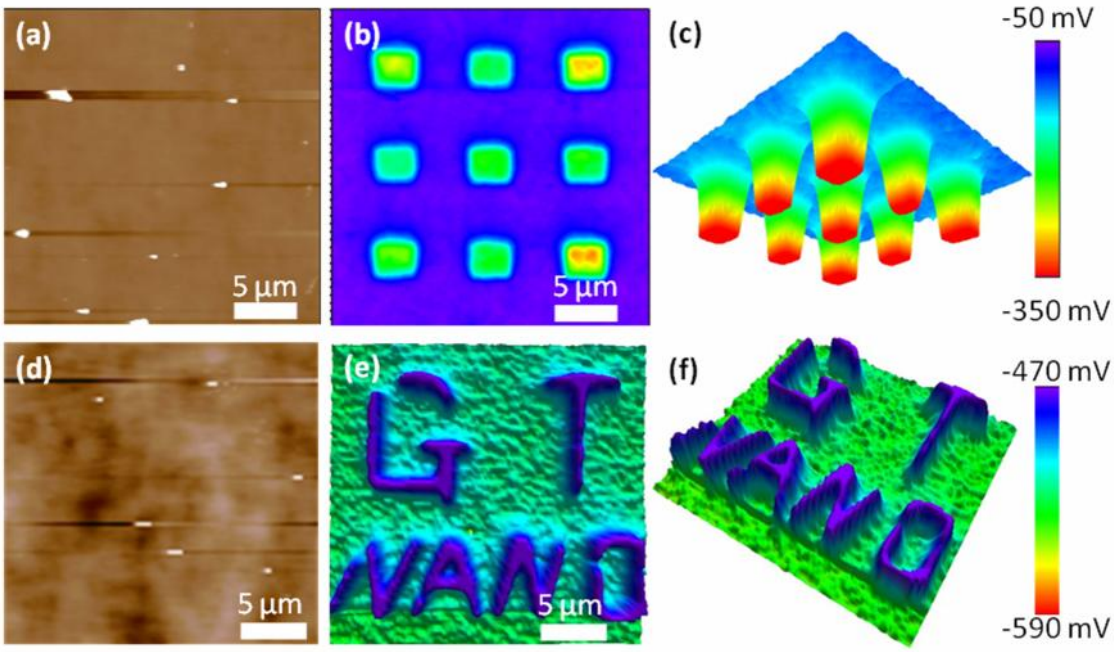

Figure 4.7 Patterning of the surface triboelectric charges on an insulator surface. Patterning of negative charges: (a) surface topography image, (b) 2D, and (c) 3D images of charge density after patterning. Patterning of positive charges: (d) surface topography image, (e) top and (f) side view of 3D images of charge density after patterning.

CHAPTER 5

MANIPULATION OF THE TRIBOELECTRIC PROCESS BY ELECTRIC FIELD[57]

5.1 Existing approaches for modulating triboelectric charge transfer

Triboelectrification has been regarded as detrimental problems in a numbers of situations such as electronic circuits and systems, which thus attracts extensive efforts to alleviate this effect[58]. On the other hand, this effect has also been utilized for different purposes such as painting,[25] particles separating,[59] and mechanical energy harvesting. For the sake of better performances in these applications, higher density of charges transferred in the contact electrification process is always favorable[31, 60]. Therefore, in all the studies and applications related to the contact electrification, control of this effect is a critical issue. Previously, modulation of triboelectric charge density was realized through intrinsic approaches such as material selection[22, 61] and surface functionalization[26, 27, 62] that directly changes the difference of the surface potentials.

Extensive research has been done to develop triboelectric series, as summarized in Figure 5.1[61], where the materials in the positive side, defined as triboelectrically positive materials, are more likely to loss electrons and be positively charged when they get in contact with another material; the materials in the negative side, defined as triboelectrically negative materials, are more likely to gain electrons and be negatively charged when they get in contact with another material. This series table provides

guidance to rational materials selection when triboelectrification charge transfer is considered: materials at two ends of the table are selected when triboelectrification is preferred to be maximized while adjacent materials in the table are selected when triboelectrification need to be minimized. In many circumstances, however, the materials selection is largely limited by fabrication feasibility, system design and functionalization.

Another approach is to modify the surface structure of contact electric materials through physical or chemical treatment. R. G. Horn, et al. demonstrated an enhanced capability of gaining negative charges on amino-silane treated silica surface based on the proposed acid-base interaction mechanism[62]. J. J. Cole, et al. employed oxygen plasma to treat PDMS to be easier to gain or lose positive charges to SiO_2 or PMMA after the two materials are in contact, explained by their theory about the reactions of different functional groups on the surface[63].

However, these methodologies are sometimes largely limited by the feasibility of material choices in some applications. So far, there have been few reports about the extrinsic method that can control charge transfer at insulator surfaces within pre-set materials. Using the recently developed atomic force microscopy (AFM) based in-situ triboelectric characterization method, as described in chapter 4, it is possible to investigate extrinsic approaches that can modulate the triboelectrification process, which can be potentially utilized to enhance the output performance of energy

harvesting devices or nullify the triboelectric charge transfer in applications where this effect is undesirable.

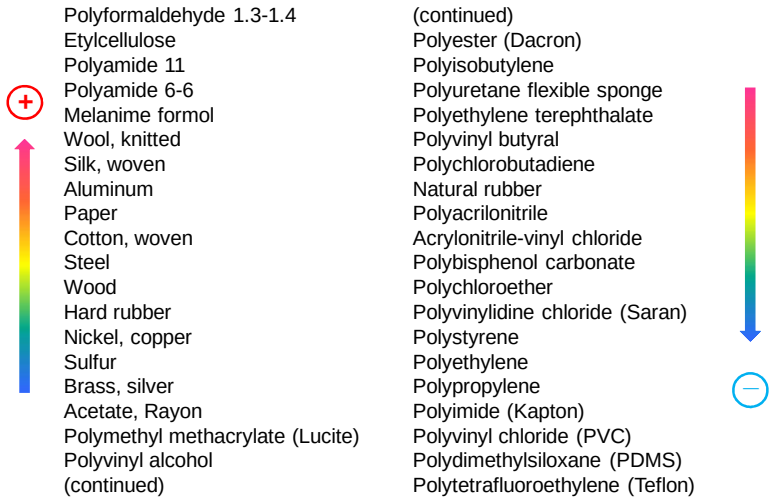

Figure 5.1 Triboelectric materials series[61]

In this chapter, the electric field modulation will be discussed. A theoretical model was derived to elaborate the dependence of transferred charge density on different parameters such as externally applied bias and the thickness of dielectric layer at the equilibrium status. To verify the model, we employed the AFM based in-situ characterization method introduced from our previous work, where a Pt coated AFM tip was scanned over a Parylene surface with a bias and the surface charge density is then characterized by the scanning Kelvin potential microscopy (SKPM).

5.2 Theoretical model for electric field's influence on triboelectrification

Figure 5.2 schematically depicts the charge transfer between a metal and a dielectric layer in contact electrification. When the top electrode contacts the dielectric layer, according to the electron transfer mechanism[64, 65], electrons will transfer from

one to the other due to the difference in the effective work functions of two materials. Subsequently, the transferred contact electric charges can also induce opposite charges in the two metal electrodes due to electrostatic induction. Although the equivalent band gap in dielectric materials are large (usually larger than 8 V), it usually has surface states within the bandgap that can accommodate electrons[65]. Here we utilized the energy band diagrams to illustrate the case of a triboelectrically negative dielectric material (as compared to the metal). Accordingly, the highest filled surface energy states of the dielectric material is below the Fermi level of the metal, as illustrated in Figure 5.2b.

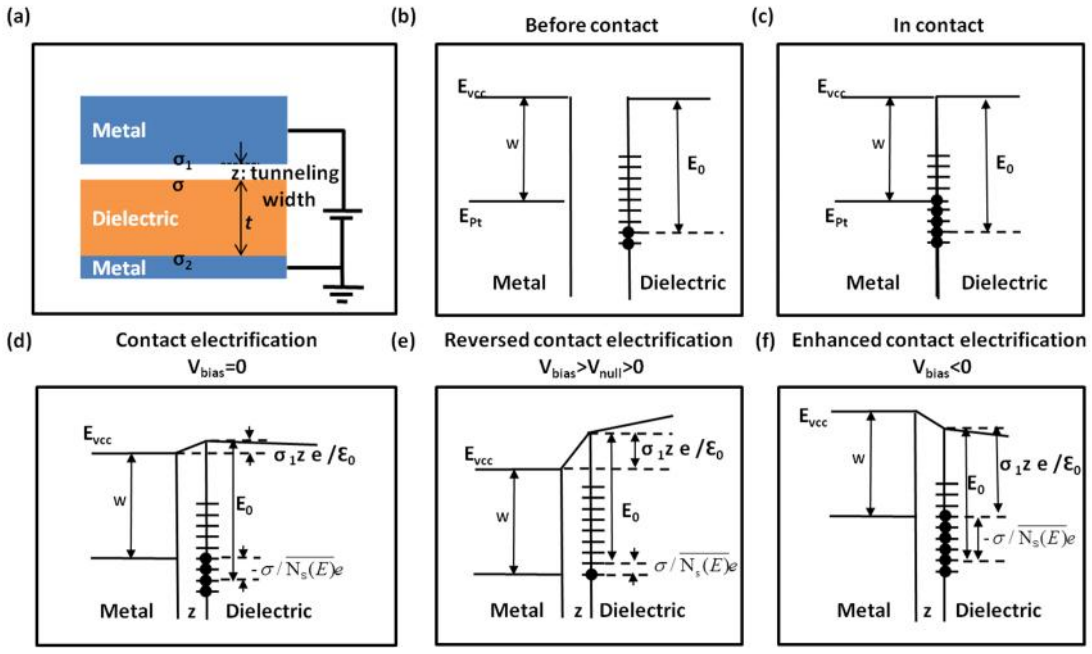

Figure 5.2 (a) Illustration of the contact electrification process with a tunneling width z, the charge transferred to the dielectric surface with a density of σ, induced charge density σ_1 and σ_2. (b-f) Energy band diagrams for the metal and dielectric

materials in the situations of pre-contact (b), in contact with no bias (c), in separation equilibrium with no (d), positive (e) and negative (f) bias.

When the two materials are in contact, electrons in the metal will flow from the top metal electrode onto the dielectric surface to fill up the surface states as high as the metal's Fermi level (Figure 5.2c). When two materials are separated from each other, an electric field is built up due to the transferred charge on the dielectric surface and image charges on the metal side, as depicted in Figure 5.2d. The strength of the electric field is proportional to the induced charge density σ_1 in the metal side. Due to this locally built-up electric potential, a portion of the charges on the dielectric surface can flow back to the metal[20, 65, 66]. The potential difference is determined by the separation distance and electric field strength. At the same time, the separation process also creates an energy barrier between two surfaces that hinders the back-flow of electrons. For simplicity, we assign a critical tunneling distance *z*, and assume that below *z* the electrons can flow freely between two surfaces to maintain a constant Fermi level and above *z* the barrier is large enough to prevent any tunneling[66]. For a parallel-plates model, at the distance *z*, the dielectric surface charge σ induces σ_1 on the top metal and σ_2 on the bottom metal, which should satisfy

$$\sigma + \sigma_1 + \sigma_2 = 0 \tag{5.1}$$

Due to built-in electric field σ_1/ε_0, the vacuum energy level between the metal and the dielectric surface changes by ΔE_{vcc} :

$$\Delta E_{vcc} = \sigma_1 ze/£_0 \tag{5.2}$$

where e is the elementary charge.

When the system is in equilibrium, the dielectric surface state will be filled up as high as the Fermi energy level in the metal. If we assume that the surface density of states is $N_s(E)$ and the range of filled surface states is ΔE_s, we have

$$\sigma = -e\int_{E_0}^{E_0+\Delta Es} N_s(E)\, dE \tag{5.3}$$

Here, we use the averaged surface density of states as defined below,

$$\overline{N_s(E)} = \frac{\int_{E_0}^{E_0+\Delta Es} N_s(E)\, dE}{\Delta E_s} \tag{5.4}$$

Therefore, the range of filled surface states ΔE_s can be described as

$$\Delta E_s = -\pm / \overline{N_s(E)}e \tag{5.5}$$

Combining Eq. (5.2) and (5.5), we have,

$$E_0 - W = \Delta E_{vcc} + \Delta E_s = \sigma_1 ze/\varepsilon_0 - \sigma/\overline{N_s(E)}e \tag{5.6}$$

An external potential applied between the top and bottom (electrode underneath the dielectric film) metals will change the relative energy band height, which modulates the charge transfer accordingly. A positive bias applied to the top metal can lower its Fermi energy level, thus reducing the number of electrons transferred from the metal to the dielectric. At certain bias, the Fermi energy level will be as low as the highest filled

surface states in the dielectric material. As a result, no charge will transfer between the metal and the dielectric surface, suggesting the contact electrification will be nullified. When the bias is more positive than the nullified bias, electrons will flow in a reversed way from the dielectric to the metal, leaving dielectric surface positively charged, as illustrated in Figure 5.2e. On the contrary, a negative bias to the metal can raise its Fermi energy level, driving more electrons flow to the dielectric surface to fill up higher surface energy states, resulting in the dielectric surface to be more negatively charged (Figure 5.2f). Under the parallel-plate assumption, the bias *V* between two metal electrodes can be written using Poisson equation as:

$$V = \frac{\sigma_1}{\varepsilon_0} z - \frac{\sigma_2}{\varepsilon\varepsilon_0} t \tag{5.7}$$

Combining Eq. (5.1), (5.6) and (5.7), we can derive the surface charge density on the dielectric surface σ as:

$$\pm = \frac{V + \frac{(W - E_0)}{e}(1 + t/£z)}{t/££_0 + \frac{1}{\overline{N_s(\mathrm{E})}e^2}(1 + t/£z)} \tag{5.8}$$

This equation provides a guideline on how the external electric field quantitatively modulates the contact electrification.

5.3 SPM based experiment method – manipulation and characterization

To understand the proposed theoretical model, we conduct the experiments using AFM, as illustrated in Figure 5.3a and 5.3b. The sample we tested on were

Parylene films with different thickness. The Parylene samples used in the experiments were prepared by depositing Parylene C layer on the copper coated silicon wafer using SCS Labcoater PDS 2010. The thickness of the Parylene layer was controlled by the weight of the Parylene C source and measured by SEM (SU8010 from Hitachi High-Tech) after deposition.

First, the AFM was operated in contact mode and the Pt coated tip scans over a certain area of a Parylene film (600 nm in thickness) under a bias between the Cu layer on the sample and the tip (Figure 5.3a). The normal force was controlled at 49nN. (The deflection of the cantilever was set to be 0.4V, the sensitivity of the optical lever 126 nm/V, and the spring constant of the cantilever 0.98 N/m.) This process incurred contact electrification between the tip and the dielectric surface, and parameters such as bias, contact force, rubbing speed and cycles can be accurately controlled in the AFM system.

Subsequently, the surface potential of a larger area including the rubbed area were characterized in SKPM mode (Figure 2b) with the substrate grounded. The quantified surface potential difference between the rubbed and intact areas can be used to calculate the surface charge density transferred by the contact electrification.

Figure 5.3c shows the surface potential distribution of a 10×10 μm^2 area including an area of 4×4 μm^2 that was rubbed at 0 and 5 V biases before the measurement of surface potential, respectively. After zero-bias contact electrification, the rubbed surface has lower surface potential compared to the surrounding intact area, suggesting a negatively charged area. In contrast, after 5 V biased contact electrification,

the rubbed surface has higher surface potential as compared to the surrounding intact area, indicating a positively charged area. The positive charges are locally preserved on the surface after 1 hour, suggesting that the reversely-charged area is very stable. The experiment results are consistent with the proposed theoretical model in Figure 5.2e.

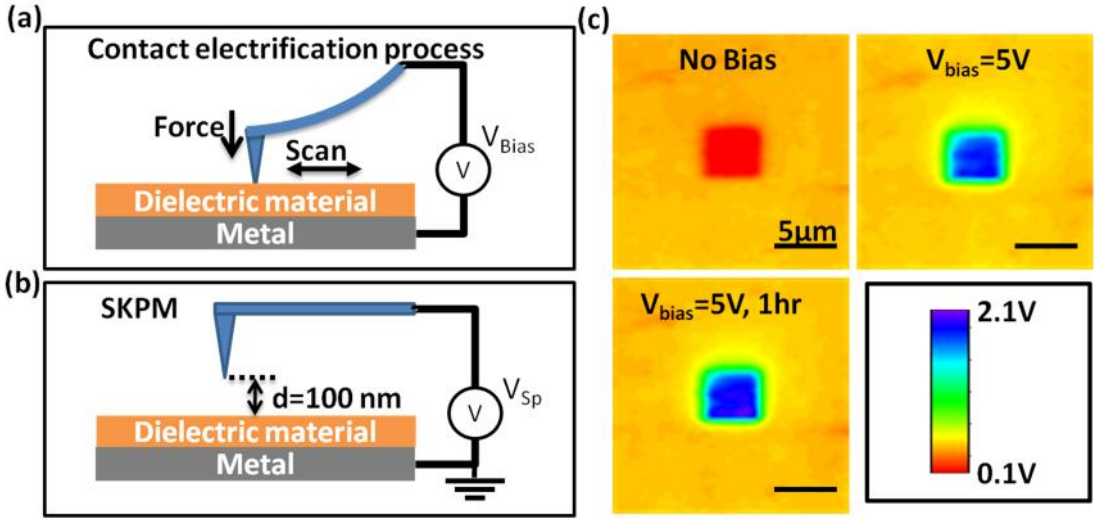

Figure 5.3 Schematic of experiment setup including two steps: (a) the first step is to use AFM tip with a bias between the tip and the substrate scan over the surface in contact mode, (b) the second step is to use SKPM to map the surface potential distribution. (c) Surface potential distribution of the rubbed and the surrounding area after regionally rubbed by AFM tip at no bias and 5 V bias immediately after rubbing and 1 hr later, demonstrating that bias can reverse the triboelectric charge transfer, and the transferred charges have little leakage or diffusion.

5.4 Results and Discussion

From Eq. (5.8), the transferred charge density σ should change with the externally applied bias V. To quantify the electric field influence, fresh areas of a

Parylene film (2 μm in thickness) were rubbed with different bias from -10 V to 10 V and then measured in the SKPM mode. Figure 5.4a displays the surface potential distribution in the areas that were rubbed with biases from -2 V to 5 V: a negative bias can enhance the negative charge density; a positive bias of 2 V almost nullified the charges; a bias of higher than 2 V brought positive charges to the rubbed surface. A cross section profile of the surface potential distribution of each experiment was plotted in Figure 5.4b. It can be found that the surface potential of the rubbed area is adjusted monotonically by the applied bias, where the positive bias brings the surface potential to be more positive, and the negative bias exhibits the opposite effect. The corresponding surface charge density calculated from the surface potential profile is plotted as a function of the applied bias during the rubbing process in the inset of Figure 5.4b.[21] It can also be seen that the surface charge density increases with increasing the applied external bias with a nonlinear characteristic, which is associated with the different energy state densities in the middle of band gap and closer to the conduction/valence band.[26]

According to Eq. (4.8), the contact electrification and the modulation of applied bias should also be dependent on the thickness of the dielectric layer. We have conducted the experiments on three Parylene samples with different thicknesses of 300 nm, 600 nm, and 2.4 μm. For the contact electrification without bias, the surface potential change increases with thickness but the transferred surface charge density

decreases with thickness, as shown in Figures 5.5 a(i) and b. Substituting $V = 0$ into Eq. (4.8), we have

$$\pm = \frac{(W - E_0)/e}{1/(\text{£}/t + 1/z)\text{£}_0 + 1/\overline{N_s(E)}e^2} \tag{4.9}$$

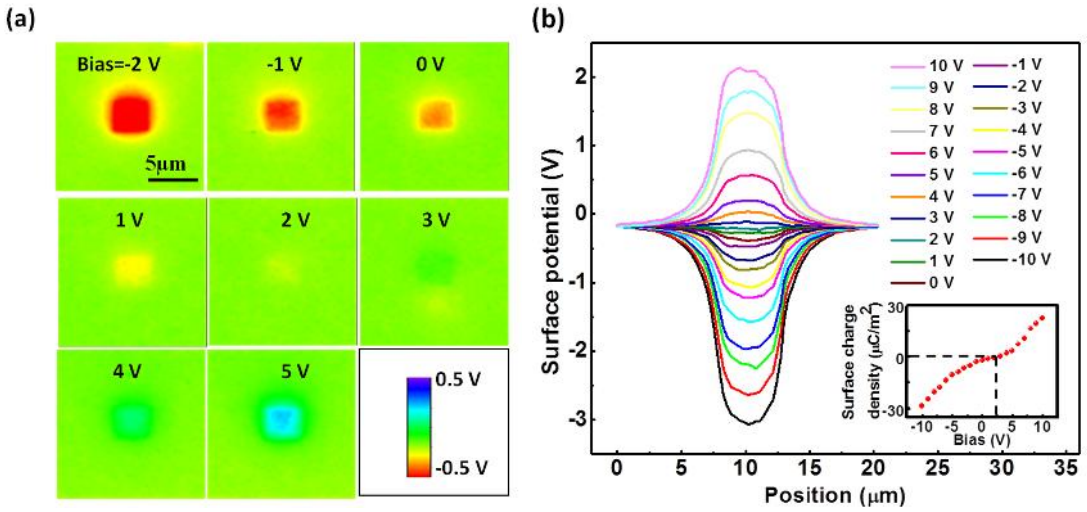

Figure 5.4 (a) Surface potential distributions of the Parylene film including the areas that were rubbed by Pt coated AFM tip at different bias from -2 V to 5 V. (b) Cross section profiles of the surface potential of the Parylene film rubbed with bias from -10 V to 10 V. The inset is the calculated surface charge density as a function of bias. With a bias of about 2.5 V, the surface charge density is zero, indicating the contact electrification is completely canceled out by the applied bias.

Eq. (4.9) indicates that the conditions of a thinner dielectric layer and larger $\text{£}/t$ can result in a higher surface charge density, which is consistent with the experimental results. In essence, this thickness dependence effect is because that the surface potential changed by contact charge decreases with thinner dielectric layer and thus it takes more

contact charges to make the upper filled energy level the same as Fermi level at the equilibrium.

The nullifying bias for different thickness also varies, as illustrated in Figures 5.5 a(ii) and c. For Parylene film with a thickness of 300 nm, a bias of 1.4 V between the tip and the bottom electrode can leave the rubbed area the same surface potential as the intact area, indicating that no charges were transferred during contact electrification process. The biases needed for nullification increases with increasing the thickness (1.4 V, 300 nm; 1.6 V, 600 nm; 3 V, 2.4 μm). From Eq. (4.8), we can derive the nullify bias by substituting the surface charge density σ with zero:

$$V_{\text{null}} = (E_0 - W)/e + \frac{t}{\text{£}z}(E_0 - W)/e \tag{4.10}$$

The bias needed to nullify the contact electrification increases with the thickness of the dielectric film. It should be noticed that the relationship between the nullifying bias and the thickness of the dielectric layer may not be linear since the back tunneling width *z* can also change with thickness. In atmospheric condition, *z* is more likely to be determined by the air breakdown electric field[30], which also varies with the dielectric thickness.

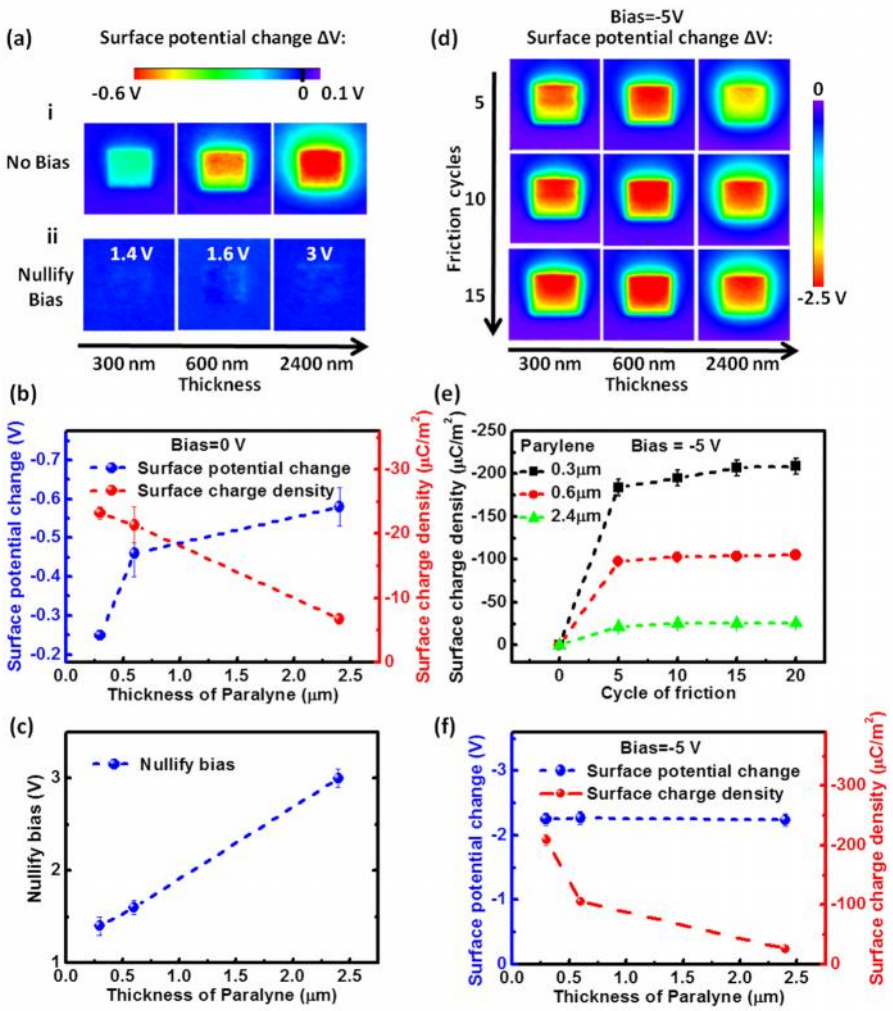

Figure 5.5 Thickness dependence of contact electrification and bias modulation. (a) Images of surface potential change Δ*V* of different thickness samples after they were rubbed at no bias (i) and nullify bias (ii), respectively. (b) The surface potential change and surface charge density as a function of the thickness of the Parylene layer after the sample was rubbed at no bias. (c) The nullify bias as a function of the thickness of the Parylene layer. (d) Images of surface potential change Δ*V* of different thickness samples after they were rubbed by different cycles. (e) Calculated surface charge density as a function of friction cycles. (f) The surface potential change and charge density after 20 cycles of friction as a function of thickness of Parylene.

We also investigated the effect of dielectric thickness on the contact electric charge density in the bias-enhanced situation. In the experiment, for each sample, a 4×4 μm^2 area was rubbed by the -5 V biased tip for 5 cycles and its surface potential was characterized in the SKPM mode. This process was repeated four times for the same area to obtain the information of the charging kinetics. As displayed in Figure 5.5e, the transferred surface charge density increases with friction cycles and saturates after around 20 cycles. Figure 5.5f illustrates that the surface potential change is almost the same for different samples, while the surface charge density is larger for thinner dielectric sample, indicating that the bias has a stronger effect on thinner samples for the surface charge transfer. This trend can also be implicated from Eq. (5.8), where the slope of V inversely correlates with the thickness t.

In conclusion, we report a new approach to manipulate contact electrification process through an applied electric field. A theoretical model and following experiments between Pt and Parylene thin film presented in this study illustrates that the charges transferred from contact electrification can be modulated in both polarity and surface charge density by an external applied bias. A positive bias between Pt and Parylene can attenuate, nullify or reverse the negative charges transferred from Pt onto Parylene surface, while a negative bias can be utilized to enhance the transferred negative charge density. Furthermore, this modulation effect is enhanced for thinner dielectric layers, and the nullifying bias increases with increasing dielectric thickness. Our study demonstrates an effective approach for controlling the contact electrification,

with potential applications in charge-assisted separation, energy harvesting as well as anti-static protection.

CHAPTER 6

SELF-POWERED DISPLACEMENT SENSOR BASED ON MICRO-GRATED TRIBOELECTRIFICATION[67]

Measurement of displacement and speed at the micro- and nano-scale has ubiquitous applications in the scientific and industrial fields such as manufacturing, automation, robotics, and nano-manipulation. Traditionally well-established techniques to detect displacement or speed include optical approaches based on optical interference[68], electrical techniques based on capacitive sensing[69, 70], electromagnetic induction[71], and piezoelectric sensors[72]. However, there is always a trade-off among resolution, working distance and complexity. Furthermore, most of the existing sensing technologies need pre-provided electrical or optical signals in order to detect the mechanical displacement, which inevitably requires external power sources. However, the increased number and density of portable electronic devices and sensing networks today desperately desires low power consumption and/or self-powered sensors[73-76].

Since 2012, the triboelectric effect, in combined with electrostatic induction, has been demonstrated with great performance in converting mechanical energy into electricity[16, 17, 19]. The corresponding working mechanism of the devices, as named triboelectric nanogenerators (TENG), is to transform motion into contact-separation between two triboelectric charged materials, which induces electrical potential change that drives electrons to flow in the external circuit. Enlightened by this approach, it is

possible to develop self-powered displacement sensors that transduce the displacement input directly into electric output signal without any external power source.

6.1 Fundamental mechanism of TENG and self-powered displacement sensor

Sliding mode nanogenerators have demonstrated electron transport driven by the electrostatic induction with relative moving triboelectric charged plates. The working mechanism is illustrated in Figure 6.1. When two plates with different dielectric materials contact with each other, charges transfer from one surface to the other due to triboelectric effect (Figure 6.1a). If one plate moves horizontally relative to the other, a portion of the transferred charge will preserve on the surface, leading to a pair of inversely charged dielectric surface (Figure 6.1b). Spatial separation of the charged dielectric surface results in a surrounding electric field that increases with amount of separated surface charge, which is a function of the separated surface areas. If the back surfaces of the two dielectric materials are coated with metal layers, there will be a measurable electrical potential between these two electrodes, which refers to open circuit (OC) voltage used in the following experiments. The magnitude of the OC voltage is a function of the separation distance.

A more detailed analytical model can be derived to explain and quantify this electrostatic induction process[60]. As illustrated in Figure 6.1, for an OC condition, the positive charge on the separated area on the bottom surface of dielectric will induce charge redistribution in the metal. If the width of the dielectric layer is much larger than

its thickness (W/t>10), we can safely use the assumption that the vertical electric field dominates the electrical field within the dielectric layer, similar as the case for parallel capacitor. When the edge effect can be neglected, the nearly uniform vertical electric field leads to uniform charge distributions on the surface of metal electrodes at each region. Therefore, the separated area of the bottom surface has negative charges distributed uniformly with density of σ to screen the charges (density of -σ) on the dielectric surface; the upper surface of metal has negligible charges within the parallel electrical field assumption; the overlapped area has uniformly distributed positive charges with density of $-\frac{x}{l-x}\sigma$, where x is the separation distance, since the total charge within the metal should be 0 in the OC condition. Similarly for metal 2, its top surface has negative charge with density of -σ for the separated area and positive charge with density of $\frac{x}{l-x}\sigma$. According to Gaussian theory, the electric field of the overlapped region in Dielectric 1 and Dielectric 2 E_{y1} and E_{y2} can be derived as:[60]

$$E_{y1} = \frac{\sigma x}{\varepsilon_0 \varepsilon_{r1}\, l-x} \tag{6.1}$$

$$E_{y2} = \frac{\sigma x}{\varepsilon_0 \varepsilon_{r2}\, l-x} \tag{6.2}$$

Therefore, the V_{OC} is given by:

$$V_{OC} = E_{y1}d_1 + E_{y2}d_2 = \frac{\sigma x}{\varepsilon_0\, l-x}\ \frac{d_1}{\varepsilon_{r1}} + \frac{d_2}{\varepsilon_{r2}} \tag{6.3}$$

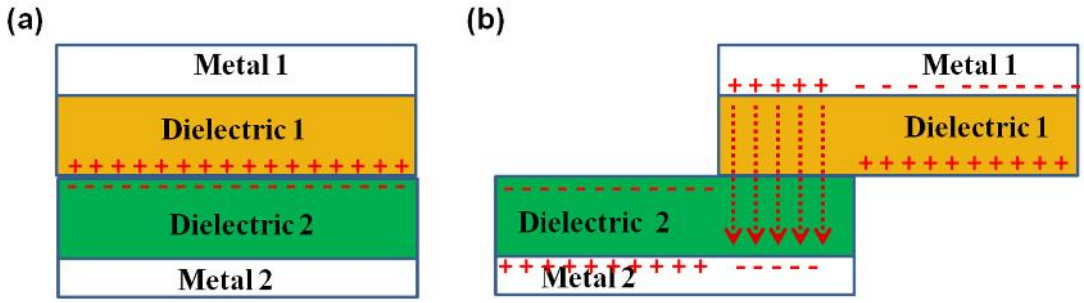

Figure 6.1 Schematic illustration of sliding mode TENG. Charge and electric field distribution when two plates (a) overlap each other and (b) separate for a certain distance.

The assumptions and results of the analytical models are validated in the finite element simulation. Figure 6.2a illustrates the parameter used in the simulation. The electric potential distributions with variable separation distances are shown in Figure 6.2b. The mesh convergence of the OC voltage at x=5cm in Figure 6.2c validates the FEM calculation. The detailed plot of V_{OC}-x relationship in Figure 6.2d agrees well with analytical model until x gets close to l. Figure 6.2e and 6.2f show the distributions of electric field in X and Y-direction, which validates our previous assumption that the Y-direction electrical field dominates in the dielectric layer. Strong X-component of electric field only exists at the edge of the two dielectrics. Inside the dielectrics, the electric field mainly has a large Y-direction component, which is nearly uniform except the edge regions where the edge effect should be considered.

It can also be found that the Y-direction component of the electric field is positive in the non-overlapped regions while negative in the overlapped regions. The nearly uniform Y-direction electric field leads to uniform charge distributions on the metal electrodes at each region, as shown in Figure 1g and h. Take the bottom electrode

as an example, at the non-overlapped regions, the charge density is approximately 7 $\mu C/m^2$, which equals to the opposite number of the surface density of tribo-charges of Dielectric 2. While at the overlapped regions, the uniform negative charges are present, which is because the total charges in each electrode are 0 at the OC condition. These results validate our previous assumptions on the uniform electric field in the dielectric layer and charge distribution at different areas of the metal electrodes.

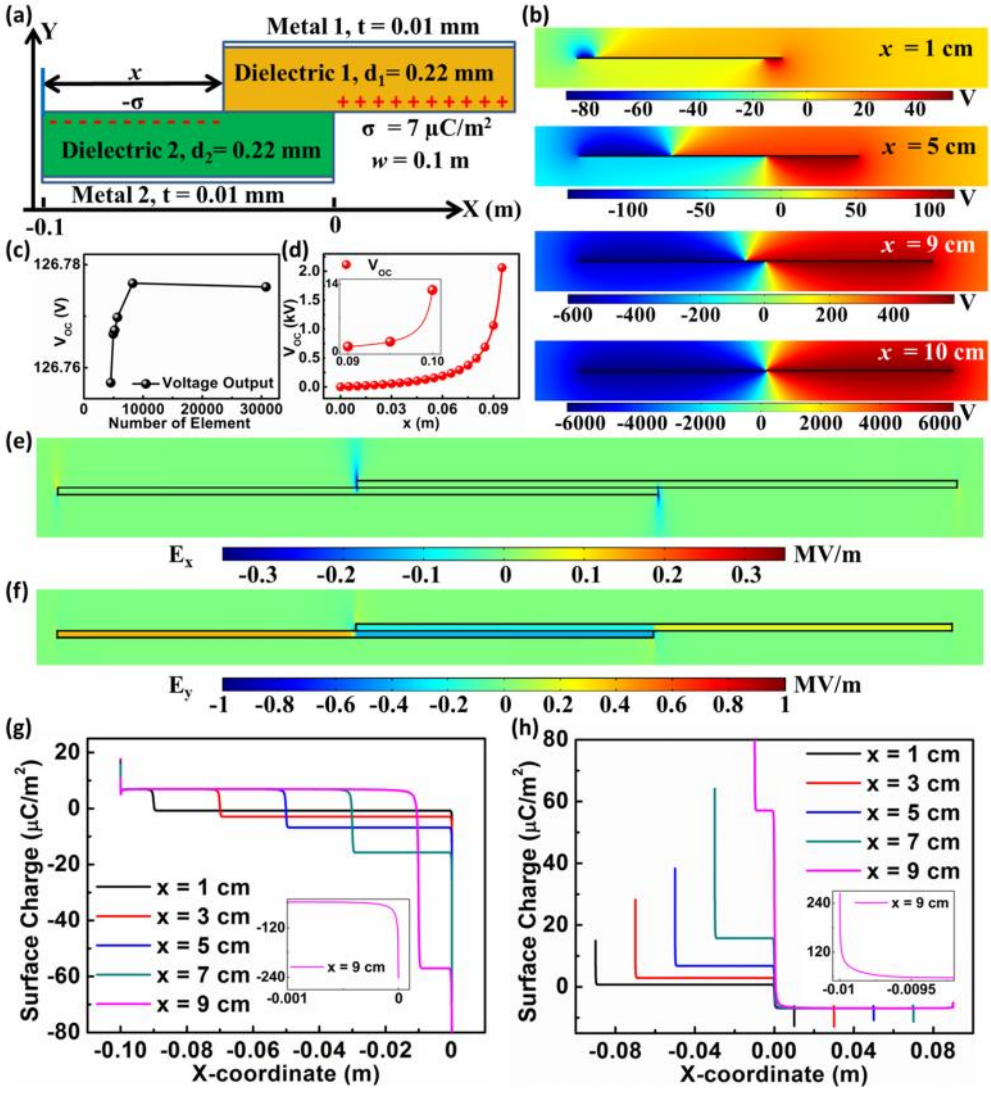

Figure 6.2 FEM calculation results of dielectric-to-dielectric TENG in open-circuit (OC) condition. (a) Structure of the FEM model. (b) Calculated electric potential

distributions at different sliding distances x. (c) Mesh convergence of V_{OC} when x = 5 cm. (d) Calculated V_{OC} at different x, the inset is the profile of the V_{OC} when x approaches to l. (e-f) Distribution of (e) the X-component and (f) the Y-component of the electric field (the scale in X-direction is 1:5 to the real case). (g-h) Calculated charge distribution of (g) the upper face of the bottom electrode and (h) the lower face of the top electrode, the inset is the enlarged profile of the surface charges at the edges when x = 0.09 m[60].

It is worth to notice that, at the edges of each region, the charge distribution is no longer uniform and peaks will exist at the two ends of the dielectrics, which is due to the edge effect. The peaks are much higher when x= 9 cm, as shown in the inset of Figure 6.2g and h, which means that the edge effect is much more significant when x approaches to l. This explains the disparity between the analytical and simulated results (Figure 6.3).

Clearly seen, Voc is a function of separation distance x and its magnitude increases monotonously with the separation distance of two plates in a predictable manner. It theoretically enlightens the potential of using TENG as a self-powered displacement sensor.

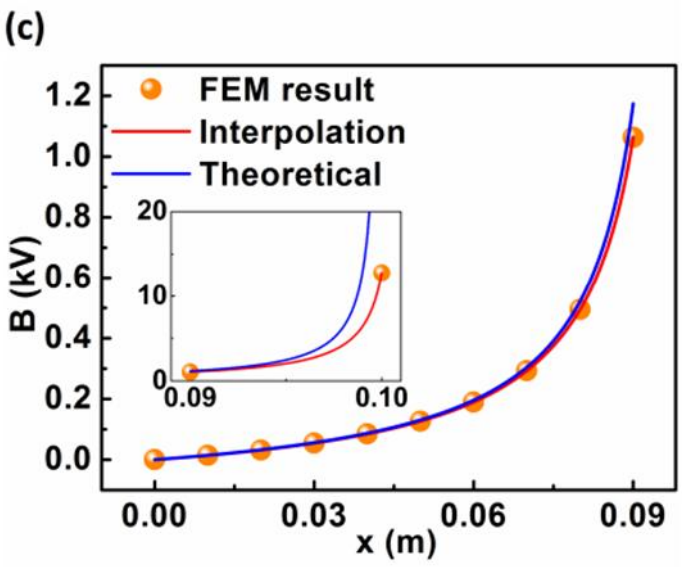

Figure 6.3 Analysis of the *V*-*Q*-*x* relationship. (a) FEM-calculated linear *V*-*Q* relationship of dielectric-on-dielectric TENG. (b-c) Comparisons of parameters (b) *A* and (c) *B* obtained through different methods: numerical FEM calculation, semi-analytical interpolation, and theoretical equation. The insets are the profile of the parameters (b) *A* and (c) *B* when *x* approaches to l[60].

In practical situation, however, dielectric surfaces have inevitable defects due to fabrication or post-process and thus the charge density may not be perfectly distributed. Therefore, the OC voltage signal will incorporate random distortion and then impair the sensing resolution. As a result, the design of the plates-pair structure has to make a trade-off between resolution and working distance: smaller plates with higher resolution or larger plates with longer detection range. In order to overcome this intrinsic dilemma of this structure design, we introduced a grating pair structure to eliminate such trade off issue.

6.2 Grating structure design for higher resolution and long working distance

The motion sensor consists of two micro-gratings with identical strip patterns, as sketched in Figure 6.4a. The grating at the bottom is made of an etched silicon wafer coated with aluminum as the bottom electrode and silicon dioxide as triboelectrically positive material; the grating on the top is made of patterned SU-8 film on a glass slide as supporting substrate and subsequently coated with Indium tin oxide (ITO) and Parylene film as the top electrode and triboelectrically negative material, respectively (Figure 6.4a inset). Transparent materials are selected for the top grating to adjust the alignment between the two gratings. Figures 6.4c, d and Figures 6.4e, f show the optical pictures and detailed microscopic structure of the as-fabricated devices, respectively. In working condition, the top grating slides within the scope of the bottom grating in a direction perpendicular to the grating strips.

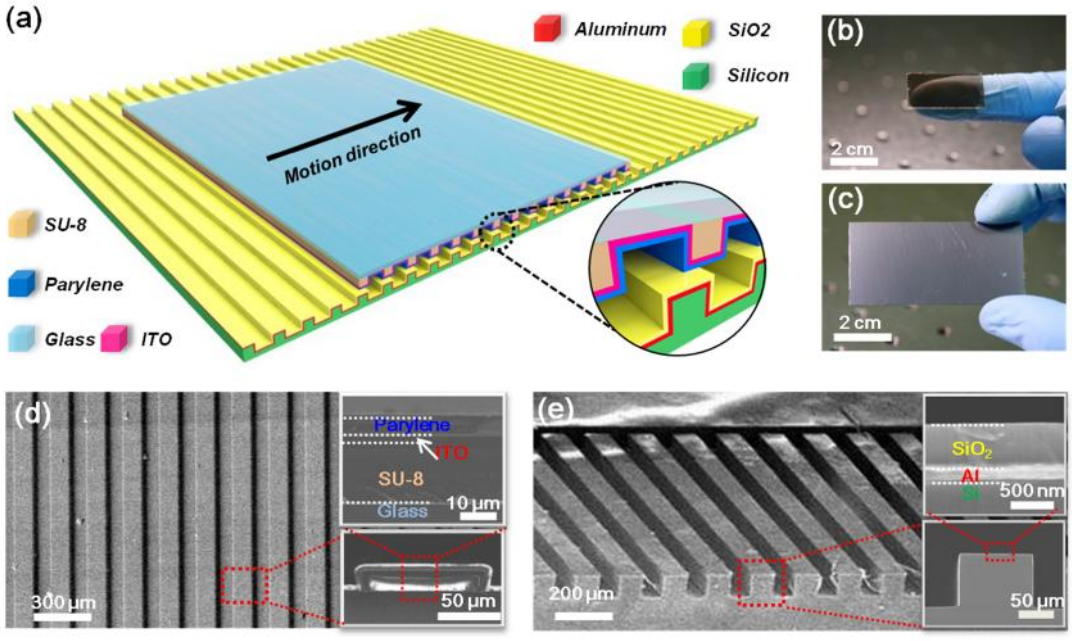

Figure 6.4 Structure of a triboelectric motion sensor. (a) Schematic of a pair of micro-gratings and detailed information of layers illustrated in the inset. (b, c) Optical photograph of as-fabricated micro-grating pair with sizes of ~30 ×15 mm^2 for the top grating and ~60×30 mm^2 for the bottom grating. (d) Scanning electron microscopic (SEM) images of the top micro-grating with glass slide substrate. The insets show the cross section profile: the ITO layer on top of the patterned SU-8 photoresist serves as the top electrode, and the outmost layer is Parylene film serving as electronegative material that participates in the triboelectric charge transfer. (e) SEM images of the bottom micro-grating. The insets show the cross section profile: the etched Silicon is coated with Al as bottom electrode and SiO_2 as electropositive material for triboelectrification.

The operating principle is illustrated in Figure 6.5. When the two gratings are brought into contact with each other, charge transfer between the two surfaces takes place due to contact electrification, resulting in negative charged Parylene surface and positive charged SiO_2 surface, because Parylene is more triboelectrically negative. A relative sliding between the two gratings results in a separation of two tribo-charged surfaces. As a result, an electrical potential between two metal electrodes underneath the tribo-charged material is built through electrostatic induction, which can be detected as open circuit (OC) voltage. If the two electrodes are connected through external circuits, the built-in voltage will drive electrons flowing from one electrode to the other when a short circuit (SC) current can be detected.

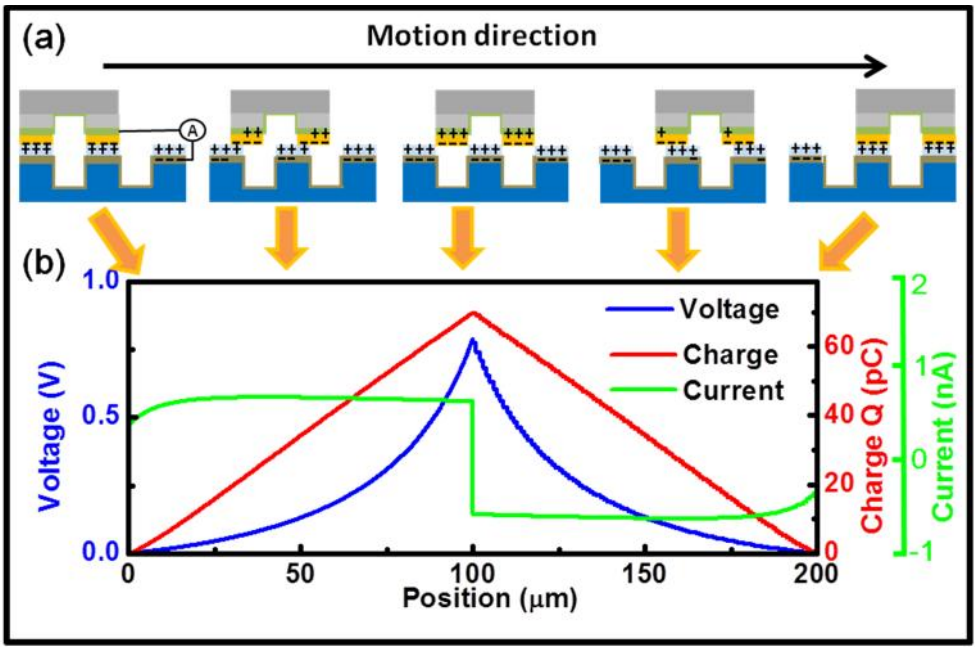

Figure 6.5 Working principle of the micrograting motion sensor. (a) Sketches that illustrate relative moving between two grating pair, leading to the charge transfer between two metal electrodes. Within a cycle of the displacement, the micrograting pair experiences conditions of full overlap, partially separation, full separation, partially separation and full overlap. (b) Numerical simulation of the electrical potential in open circuit condition (blue curve) and charge in the top metal electrode in short circuit condition (red curve). The short circuit current (green curve) is calculated from the charge change by assuming a constant moving speed of 1 mm/s. In OC condition, the potential valley and the peak present at two ends (full overlap) and the middle (full separate), respectively. In the SC condition, current changes signs from negative to positive at the two ends, from positive to negative in the middle.

Finite element simulations using COMSOL show the OC voltage and the amount of SC charge induced on the top electrode as a function of positions within a

cycle, as drawn in Figure 6.6. For simplicity, we consider four pitches for the top grating and eight for the bottom grating in the simulation model. The sidewalls of the trenches are neglected in the model due to its negligible influence on the charge induction. The width and period of the grating is set to be 100 μm and 200μm, respectively. The charge density of the bottom surface of Parylene and the top surface of SiO_2 is set to be -2 $\mu C/m^2$, 1$\mu C/m^2$, respectively. Other parameters are described in Table 6.1.

Table 6.1 Parameter used for the grating structure simulation

	Material (dielectric constant)	Thickness / μm
Top dielectric layer	Parylene (3.15)	5
Top metal layer	ITO	0.2
Bottom dielectric layer	SiO_2 (3.9)	0.5
Bottom metal layer	Al	0.2

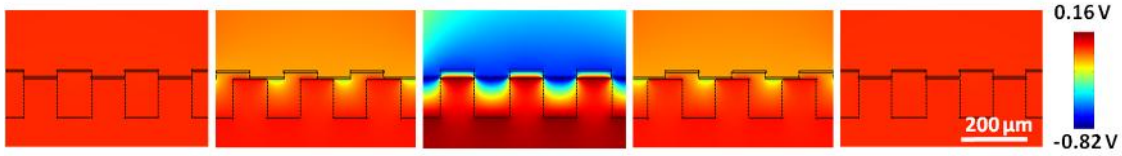

Figure 6.6 Illustration of the electrical potential change when the top grating moves one period. The figures from the left to the right describe different status: full overlap – half separation – full separation – half separation.

Figure 6.6 shows the surrounding potential distribution when the top grating is positioned at different location relative to the bottom grating. The magnitude of the

voltage and charge transfer between two electrodes at OC and SC conditions, respectively, were obtained at ten positions and then interpolated into a continuous curve, as shown in the lower graph of Figure 6.5. For the first half cycle when the top micro-grating moves from overlap to separation, the OC voltage and the amount of induced charge increases from zero to their maximums, and accordingly the SC current is positive; for the second half cycle when the top micro-grating moves from separation to overlap position, the OC voltage and the amount of induced charge decreases from their maximums to zero, and accordingly the SC current changes to be negative. Continuous movement alternates the two oppositely charged surfaces between overlap and separation, thus generating an alternating OC voltage or SC current output.

For low resolution detection, by counting the number (n) of the voltage peaks plus valleys (or the current zero-crossings), the displacement can be calculated

$$D = nP/2 \tag{6.4}$$

where P is the period of the grating. This period counting method simplifies the circuit design, though the resolution is limited by half of the pitch size, which usually can be 1-100 um with current microfabrication capabilities.

For high resolution sensing, the magnitude of OC voltage within one pitch can be corresponded to the relative position between two gratings, as we simulated above. Benefited from the fact that the output signal originates from about 150 pitches that are

in parallel, the sensor has large tolerance of any variation caused by non-uniform surface charge distribution, surface contamination or grating defects.

6.3 Device fabrication and displacement sensing test

An example of the fabrication process for the micrograting pair is demonstrated here. For the top grating, an SU-8 layer with thickness of 17 μm was spun coated on a glass slide and patterned to be one dimensional grating (width: 100 μm, period: 200 μm) using standard photolithography. Afterwards, the grating was cut into desired size (15 mm x 30 mm for the presented device), followed by a sputtering of Indium Tin Oxide (200 nm), and thermally coated with Parylene C (5 μm) using STS Parylene coater. For the bottom grating, a Si wafer was etched into periodical trenches (100 μm in width and 100 μm in depth) with 200 μm period using standard inductively coupled plasma (ICP) etching methods with patterned NR9-1500PY negative photoresist (from *Futurrex, Inc*.) as etching mask. Afterwards, a layer of Al (200 nm) was coated using DC sputter and SiO_2 (500 nm) deposited using plasma enhanced chemical vapor deposition (PECVD).

The experimental setup for the displacement and speed sensing test is shown in Figure 6.7. The bottom grating is fixed on a platform that sits on a tilting stage that adjusts the alignment of the strips between the grating pair. The top grating was attached to an Acrylic plate that is fixed on a linear motorized stage (VP-25XA from *Newport Inc*.). Adhesive sponge (2 mm in thickness) is used to cushion the contact force for an intimate contact area between two grating planes. During the test, the linear motorized

stage brings the top grating substrate to move in the direction perpendicular to the strips. The acceleration/deceleration rate was set to be ±40 mm/s^2 in the uniform velocity experiment so that the non-uniform motion time is marginal. The OC voltage and SC current was measured by an electrometer (6514 from Keithley Instruments), was measured by a current preamplifier (SR570 from Stanford Research System). A low pass filter (20Hz) was used in data post-processing of OC voltage.

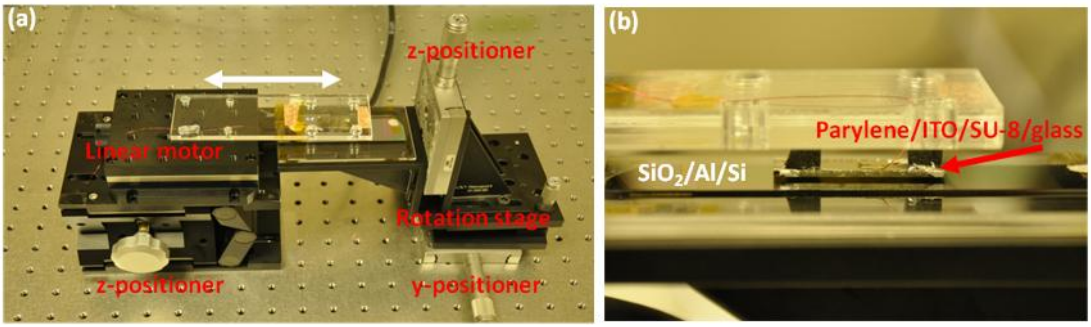

Figure 6.7 Experimental setup for the motion sensor testing. (a) The top grating is attached to an Acrylic plate using two pieces of adhesive sponge as cushion, the Acrylic plate is fixed on a 1-dimensional linear motor attached on a vertical positioner. The bottom grating is fixed on a plate that is attached with two 1D positioners and a tilt and rotation platform. (b) Detailed amplification of the two grating pair when they are in contact.

To characterize the motion sensor, a uniform speed (1mm/s) motion test was carried out. During the movement, the OC voltage measured between the two electrodes (Figure 6.8a) alternates between 0 and ~160 mV periodically at a frequency of 5 Hz (Figure 6.8b). As aforementioned, since each cycle corresponds to the period of the gratings, which is 200 μm in this device, the real time displacement can be calculated

by accumulating extra 200 μm once one more peak is detected. As shown in the blue curve in Figure 3c, the detected displacement increases linearly with time. With time frame simultaneously recorded, the real time motion speed can also be derived by dividing the width of one pitch (200 μm in this device) by the time interval between two adjacent voltage peaks, as shown in the red curve in Figure 6.8c. The average of the measured velocity is 0.994 ± 0.011 mm/s, which has 0.6% difference compared to the preset value.

During a non-uniform motion testing, the motor was set to accelerate to 1 mm/s with a rate of 0.1 mm/s^2, maintain the speed and then decelerate at a rate of -0.1 mm/s^2 until stop. The SC current measured between the two electrodes is alternating between negative to positive periodically during the motion, as displayed in Figure 6.8d. By counting the number of zero-crossings, each of which counted as 100 μm step of displacement, the real time displacement can be derived and is shown as the blue dots in Figure 6.8e. Compared with the preset trajectory as indicated in red curve, the measurement matched very well. Using a similar method for the speed calculation in uniform motion, a real time speed during this non-uniform motion can be obtained, as shown in Figure 6.8f. The advantage of the peak/zero-crossing counting method is that the measured displacement is independent of the magnitude (as long as well above the noise level) of the output signal, endowing its potential of direct interfacing with digital circuit after signal conditioning (pre-amplification), which would largely simplify the entire measurement system by avoiding complex analog to digital converting circuits.

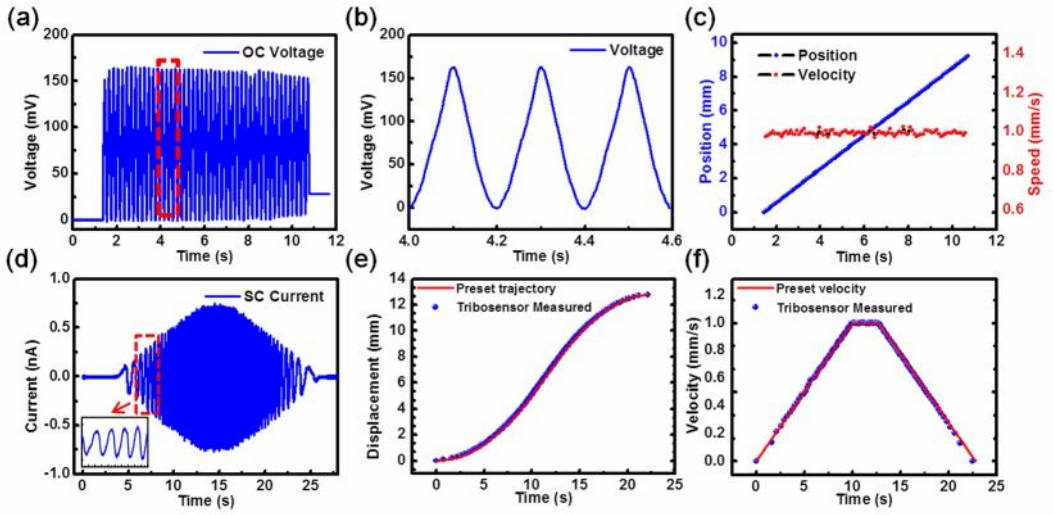

Figure 6.8 Demonstration of the long distance motion sensing by the OC voltage peak and SC zero-crossings counting method. (a) The OC voltage signals acquired from a displacement of 9.2 mm at a preset speed of 1 mm/s. (b) An enlarged view of the OC voltage signal from a, showing a similar shape as expected from aforementioned numerical simulation. (c) The real time displacement and speed derived from the measured voltage signal. (d) The SC current signals acquired from a non-uniform motion (decelerate - uniform speed - deceleration). (e) The preset motor's trajectory (red curve) and the real time displacement detected by the motion sensor (blue dots). (f) The preset motor's speed (red curve) and the real time speed detected by the motion sensor (blue dots).

For the need of high resolution sensing, analysis of the voltage within a period can substantially enhance the resolution for the displacement detection. Starting from a status with complete overlap, a step motion test with each step of 5 μm was performed. As shown in Figure 6.9a, the voltage at each position stays stable, benefited from the

extreme low mobility of the charges on the insulator surfaces. The sensitive region is found to be from 10 μm to 190 μm, where each step motion of 1 μm can be clearly differentiated from the voltage response, as shown in Figure 6.9b.

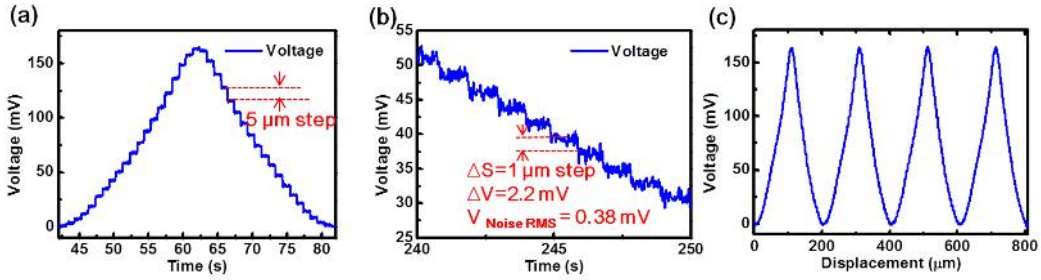

Figure 6.9 High resolution in displacement sensing realized by analyzing the magnitude of the OC voltage. (a) The OC voltage measured with a step motion of 5 μm per step within a pitch (200 μm). (b) Step motion with 1 μm per step in the sensitive region (10-190 μm) can be clearly resolved through the OC voltage signal. Given the RMS value of noise (0.38 mV), and the voltage change corresponding to 1 μm step motion (2.2 mV), the resolution can be calculated to be 173 nm. (c) OC voltage signal from 1 mm displacement. The shape of voltage signal within a pitch is very repeatable across pitches.

The change of the voltage for each step in the sensitive region is about 2.2 mV, and the Root Mean Square (RMS) of the noise V_{nosie} at 1 Hz is 0.38 mV as shown in Figure 6.10. Accordingly, the displacement resolution at bandwidth of 1 Hz can be calculated to be 173 nm by

$$S = \frac{\Delta s}{\Delta V / V_{noise}^{RMS}} \tag{6.5}$$

where ΔV is the change in output voltage in response to the displacement Δs.

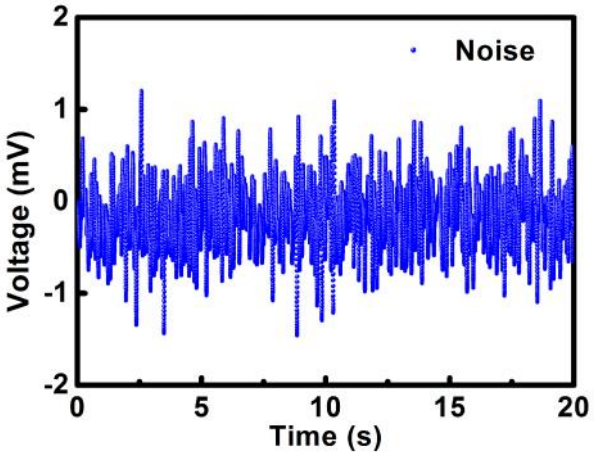

Figure 6.10 The noise of the voltage output signal.

The voltage response within a pitch can be linearized by a pre-calibration through mathematically fitting the voltage-position curve. The as-fabricated sensor has a linearity error of less than 5% within the measured range of 100 μm. The shape of the voltage signal within a pitch is very repeatable across pitches, as shown in Figure 6.9c. Since this error is almost fixed within the full sensing range (25 mm in this device), the linearity error of the sensor is less than 0.02%.

6.4 Reproducibility and reliability test

The device is based on coupling of triboelectrification and electrostatic induction, each of those two effects has been used for decades and is very well reproducible. We fabricated and tested six devices, which work in the way described above but have small variance in magnitude and shape of the OC voltage, as indicated in Fig. 6.11. The variance in magnitude may arise from the variance in the surface states

of those dielectric layers that leads to different triboelectric charge density and/or the variance in the thickness of the dielectric layer that causes different electric potential through electrostatic induction process. The variance in the shape of the OC voltage mainly comes from the variance in the width of the as-fabricated grating and/or the misalignment of two grating pairs. However, a pre-calibration of the shape and magnitude of the output signal will overcome the abovementioned shortcomings.

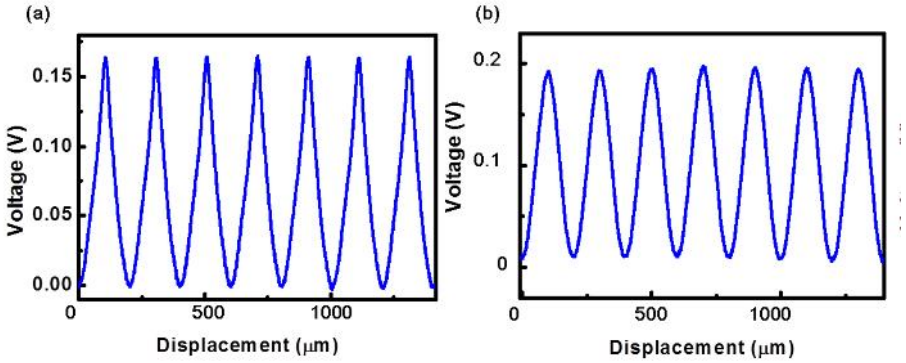

Figure 6.11 The OC voltage in response to displacement from different as-fabricated devices with feature size of 100 μm (a-b).

In the reliability test, the voltage output before and after about 1000 cycles of friction between Parylene and SiO_2 are shown in Figure 6.12 a and b, respectively. No significant change has been found. The SEM images of the surface of rubbed Parylene (Figure 6.13 a) show that most of the surface area stays almost intact while some area has slight scratches, as indicated in Figure 6.13c. The reason is that in the working condition, there is very small normal force between the two grating pairs, thus leading to a very small friction force. The small scratched area is likely caused by the particle

contaminations from the surfaces during device fabrication. This can be mostly avoided by using a higher class clean room to fabricate and package the device.

The device is designed to be very robust against abrasive wear. First, both of the friction interface materials are insulating materials with SiO_2 as a much harder material than Parylene. This prevents the two electrodes from getting electrically shorted if worn off of one dielectric layer gets the underneath conducting layer exposed. Second, the underneath conducting layers are deposited uniformly to fully cover the top, bottom and side surfaces of the gratings, which prevents the fail of one line of the grating due to cut-off damage in one line of the conducting layer, which could potentially degrade the performance without this design.

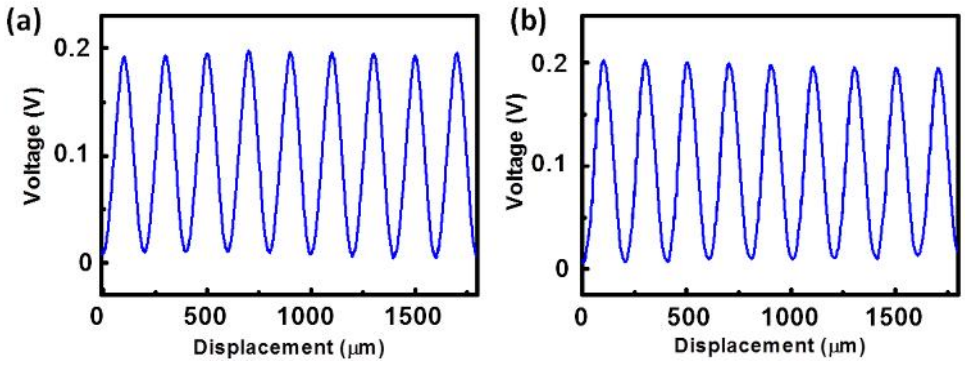

Figure 6.12 The voltage output of the displacement sensor before and after about 1000 cycles of friction between Parylene and SiO_2 are shown in (a) and (b).

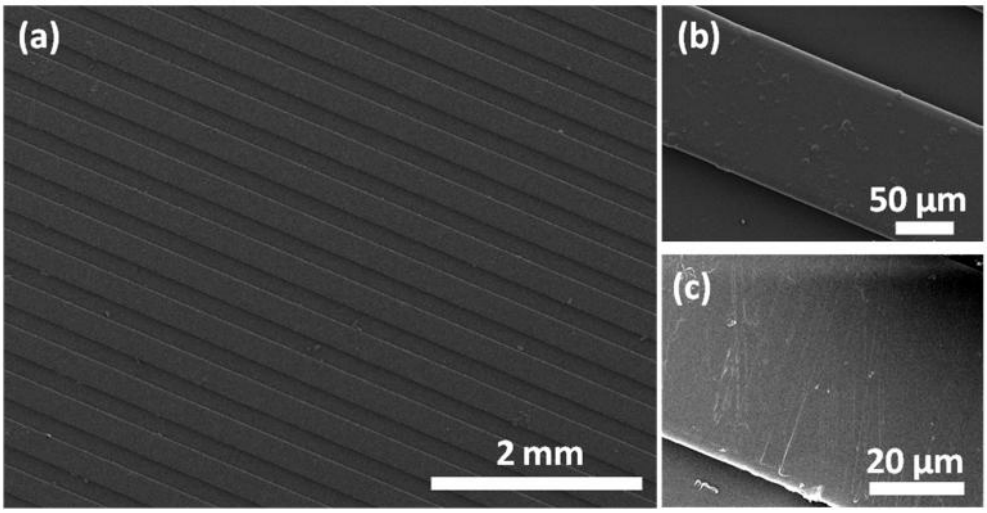

Figure 6.13 The SEM image of Parylene surface after about 1000 cycles' friction with SiO_2

6.5 Dynamic speed sensing using amplitude of SC current

In the applications when the real time speed is preferably to be directly detected, the amplitude of the SC current can be used to be quantitatively correlated with the speed. As illustrated in Figure 6.5b, the amount of charges Q induced on the electrodes is approximately linearly correlated to the displacement, as described by

$$Q=NW\sigma x \tag{6.6}$$

where x is the relative displacement within a pitch, σ is the triboelectrically transferred surface charge density on the top micro-grating, N and W are the total number of periods, and the width of the top grating, respectively. Therefore the current *I*, as a time derivative of charges *Q*, can be linearly correlated to the time derivative of the displacement—speed *v*, as indicated in Eq. (6.7) and the green curve in Fig. 6.5b.

$$I = \frac{dQ}{dt} = NW\pm v \tag{6.7}$$

The experimental SC current output under a speed ranging from 10^{-5} m/s to 10^{-1} m/s is shown in Figure 6.14 a-d with the scale of each chart 10 times as large as that for the previous one. The current in the four figures seems to have the "same" magnitude of their plateaus and valleys in their scales, indicating a very good linearity in sensing the speed over a 4 order of magnitude dynamic range. A logarithm plot of the magnitude of the detected current against motion speed from 5 μm/s to 10 mm/s is shown in Figure 6.14e. A linear fit gives its sensitivity of (679±4) pA/(mm/s) with adjusted R^2 = 0.99938. The speed resolution is calculated to be 1.2 μm/s using similar approach as described in Eq. (1), as the magnitude of the current is 6.5 pA for a speed of 10 μm/s and the RMS value of the noise is 0.8 pA.

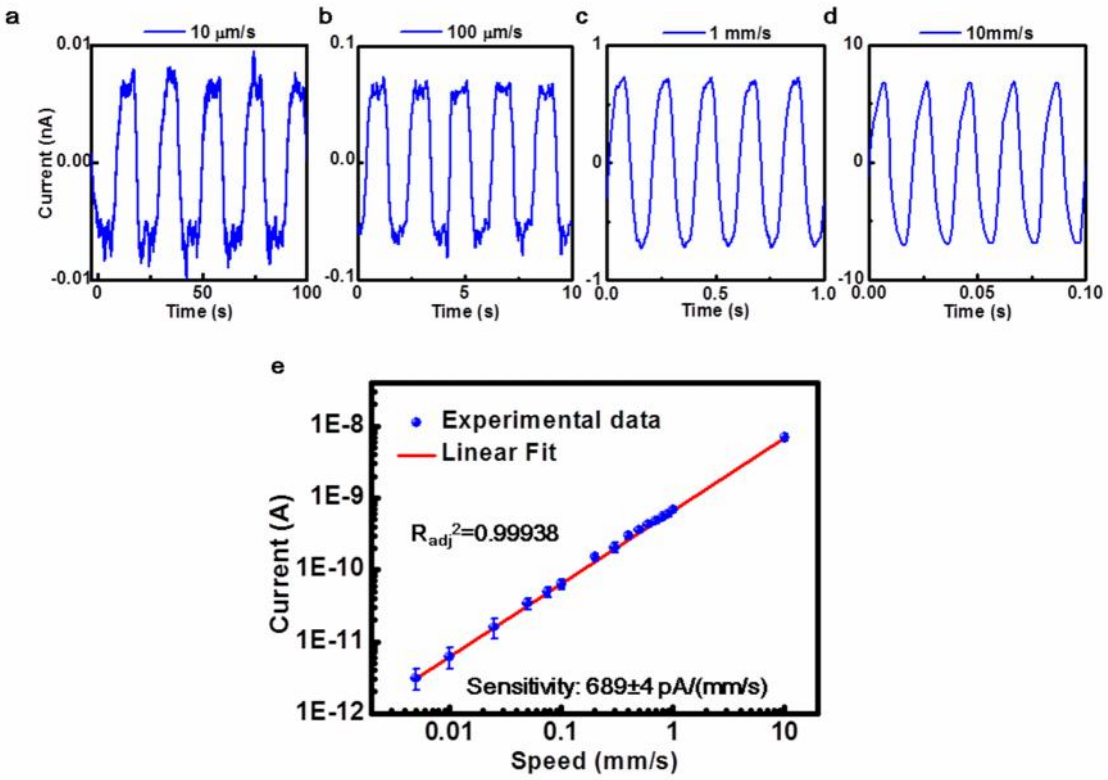

Figure 6.14 Real time speed detection through SC current. (a-d) The SC current measured with motion speed from 10 μm/s, 100 μm/s, 1 mm/s, 10 mm/s, respectively. (e) A plot of SC current as a function of motion speed from 5 μm/s to 10 mm/s with a calculated sensitivity of 689±4 pA (mm/s). (f) Speed resolution for different grating feature width at the measurement noise level of 1 pA.

6.6 Dependence of sensor resolution on grating size

The resolution of the displacement and speed sensing can be further enhanced. For displacement sensing through OC voltage, with a linear approximation, the resolution (minimum detectable displacement) can be defined as the displacement range that corresponds to half of a cycle of the output signal (one cycle corresponds to one grating period P in this device) divided by the signal-noise ratio (SNR) of the output OC voltage. From a device perspective, on one hand, SNR can be enhanced by increasing the amplitude of the sensor's OC voltage, which can be realized by increasing the triboelectric charge density at the interface through choosing more triboelectrically positive and negative materials as the triboelectric layers for the top and bottom grating, respectively. On the other hand, the displacement range per cycle can be reduced by scaling down the grating's period (*P*). Fig.6.15 shows the OC voltage output from a sensor with a period of 40 μm under uniform speed displacement condition and step motion (2 μm /step) condition, respectively. The resolution in the high sensitive region is calculated to be 54 nm, which is more than three times lower than the resolution of the 200 μm period grating sensor (173 nm).

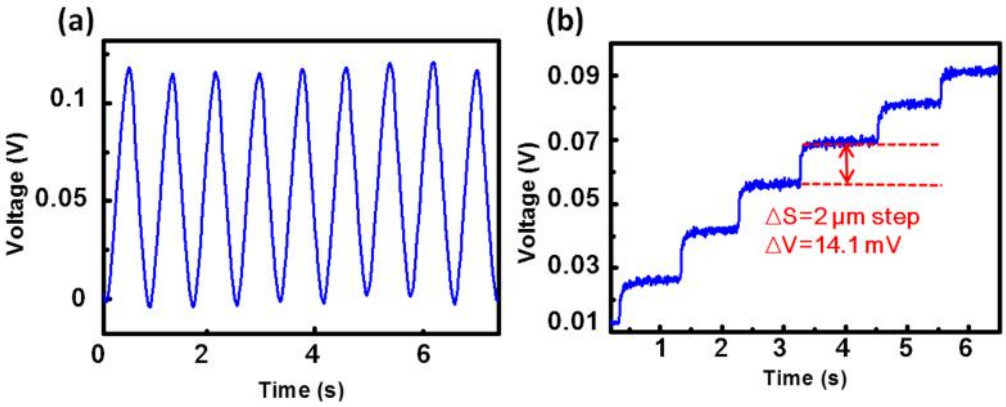

Figure 6.15 OC voltage output from a sensor with a period of 40 μm under (a) uniform speed displacement condition, and (b) step motion (2 μm /step) condition

However, reducing the size of the grooves also attenuates the OC voltage, as illustrated from the finite element simulation results shown in Figure 6.16. The reason is that the capacitance between two electrodes will increase due to increased fringe effect of the electric field between two electrodes, leading to a decreased OC voltage since *V*oc equals to the charge divided by the capacitance.

We simulated the OC voltage in full separation condition using several different grating size. From the simulation result shown in Figure 6.16, the electric field is mainly perpendicular to the ITO surface for the 100 μm grating feature width (Figure 6.16 a&c), while radiates when the width is reduced down to 10 μm (Figure 6.16 b&d). Therefore, there will be an optimized size of the grating so that relative decrease of the OC voltage is no larger than relative decrease of the grating size. The OC voltage in full separation condition was simulated with several different grating sizes and the optimized size (P/2) is found to be around 20 μm for the largest sensitivity (Figure 6.16f).

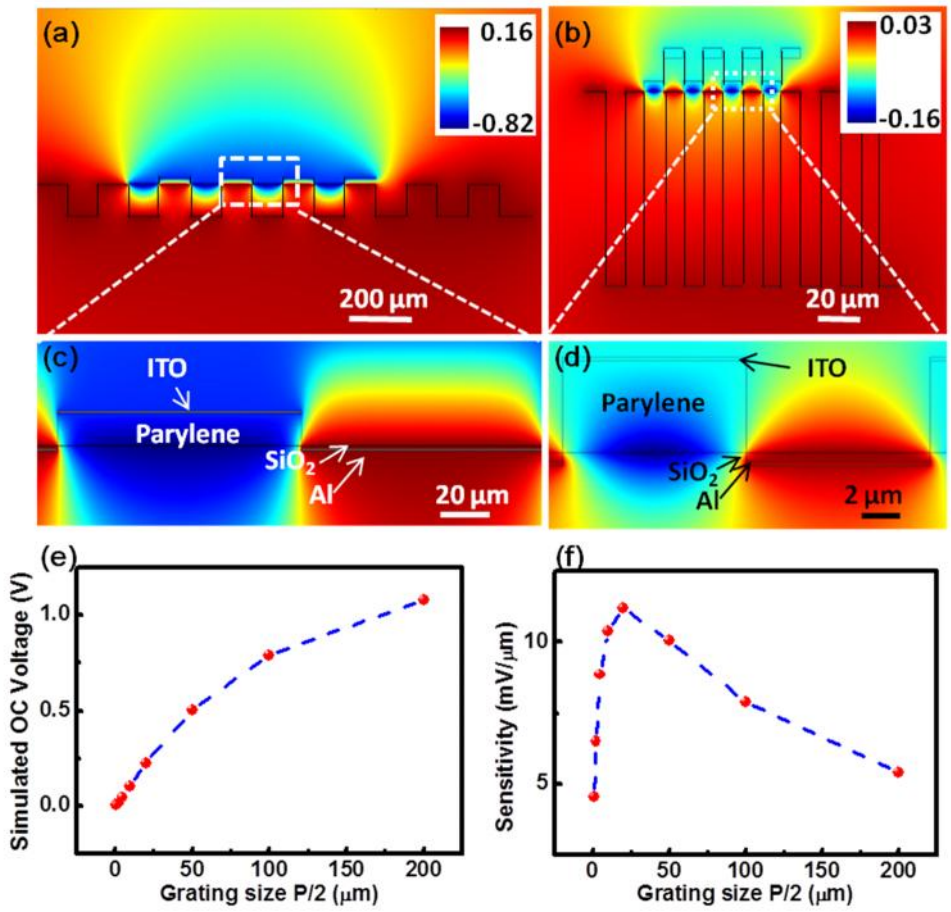

Figure 6.16 COMSOL simulation to illustrate the influence of the grating size on the OC voltage and the sensor's displacement sensitivity. Simulation of the electric potential distribution in open circuit condition of a grating pair with the grating size (as half of its period) of 100 µm (a, c) and 10 µm (b, d), respectively. In the model, side walls were neglected. Black lines that represent the sidewall were added afterwards to illustrate the structure of the grating more clearly. (e) Simulated OC voltage output as a function of grating size. (f) The sensitivity, defined as the measured range in a half cycle divided by OC voltage, is a function of the grating size.

Regarding dynamic speed sensing from SC current, according to Eq. (6.7), the resolution can be further enhanced by increasing the number of gratings (N), the width of device (W), and/or the tribo-charge density σ using different triboelectric materials system. Provided fixed device area ($L \times W$), the number of gratings (N) can be increased by scale down the grating period (P) as $N=L/P$. Similarly, because of non-negligible fringe effect as grating size shrunk down, the charges flowing between two metal electrodes during overlap-separation process are less than the triboelectric charges on the insulating surface. The amount of charges induced in the metal (Qsc) to the surface charges on the insulator for different grating feature width (w_{feature}=P/2), are calculated. As shown in Figure 6.17a, Q_{sc} decreases dramatically when the grating feature width shrinks below 25 μm, which is comparable to the thickness of the Parylene layer (5 μm). Further shrinking the grating feature width below the threshold of 2 μm no longer boosts up the output current. Therefore, there would also be a threshold grating width below which the current cannot be further enhanced. A plot of the output current as a function of the motion speed for different grating sizes, as shown in Figure 6.17b, shows the SC current increases with decrease of the grating feature width until 2 μm. Considering the 1 pA (RMS value) of the measurement system noise level, the speed resolution can be optimized to be 107 nm/s using grating feature width of 2 μm.

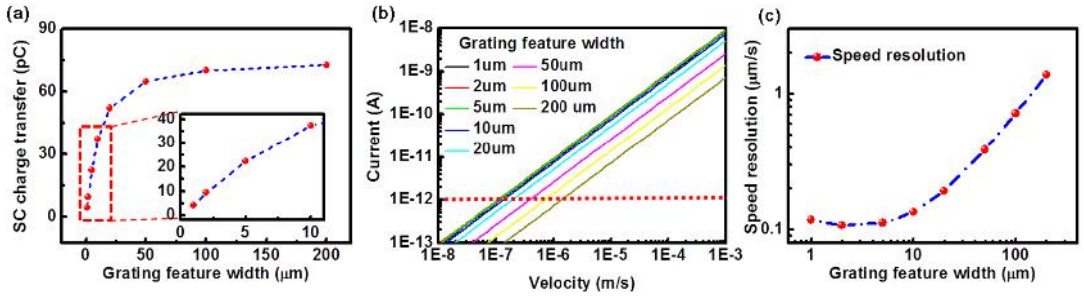

Figure 6.17 Charge transfer between two electrodes under SC condition as a function of the grating feature size simulated by COMSOL. The inset shows a zoomed-in regime. (b) Calculated SC current as a function of motion velocity for grating pairs with different feature widths. (c) Considering the 1 pA (RMS value) of the measurement system noise level, the speed resolution as a function of grating feature width.

6.7 Asymmetric feature design for direction identification

Through an asymmetric design of the grating feature, the displacement direction can be recognized from the SC charge transfer curve. As illustrated in Figure 6.18a, if the bottom grating is triangle while the top is a rectangular, when the two are moving from overlap to separation, the overlapping area of these two gratings changes differently between moving forward and backward, as shown in Figure 6.18b and c. A sample based on this design was fabricated and tested. As shown in Figure d, e and f, the SC charge transfer between two electrodes changes periodically with displacement but the shape within one period from the forward motion (e) is like a mirrored image compared to the backward motion (f). By calculating the second order time derivative of the SC charge transfer curve, the direction will be automatically recognized.

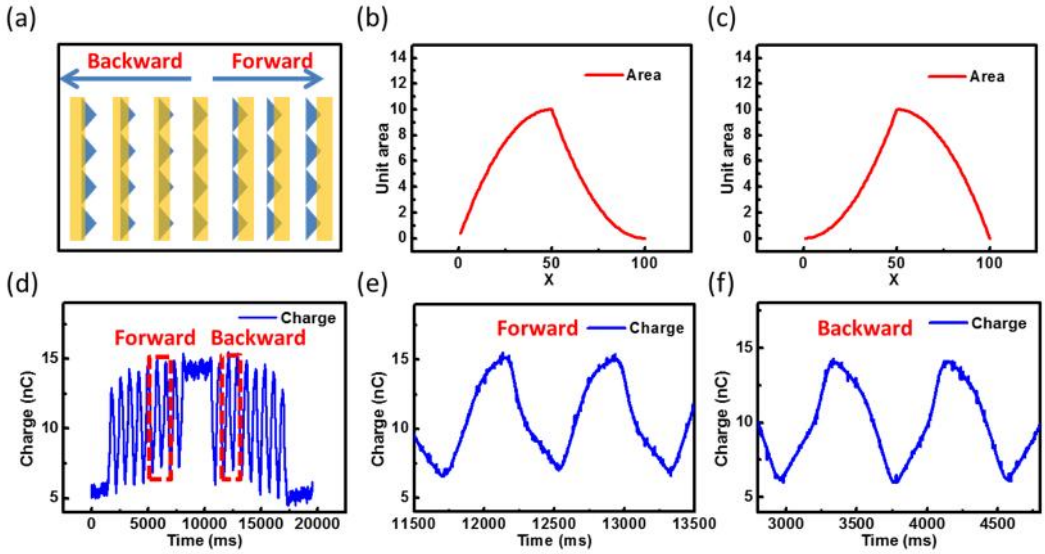

Figure 6.18 Moving direction can be identified using asymmetric grating patterns. (a) Illustration of triangle bottom grating structure (blue) and its overlapping area with regard to the top grating (yellow) at forward and backward motion. Overlapping area change as a function of displacement within one pitch at forward (b) and backward (c) motion. (d), (e), (f) experimental results of the SC charge transfer as a function of displacement.

In summary, this triboelectric motion sensor demonstrates a new approach of sensing displacement and speed without need for external power supply. The grating structure breaks displacement into cyclic signals, which solves the dilemma between resolution and working distance and significantly enhances its robustness. Besides, the sensors can be easily scaled up with very low cost if laser interference lithography is used to fabricate the micro/nano gratings. This design opens a new paradigm for displacement/speed sensing by distinguishing itself from the existing technologies

through a combination of self-powered, nano-resolution at a long working distance, high robustness and tolerance, non-optical simple structure as well as low cost. This technology has huge potential in future applications in sensor networks and self-sustained systems.

CHAPTER 7

CONCLUSION

Piezotronic and triboelectric effects have recently been demonstrated with promising applications in high sensitivity force sensing and high efficiency energy harvesting devices, respectively. This thesis focuses on characterizing these two effects at nano scale and applying the triboelectric effect to a self-powered motion sensing technology.

For piezotronic effect, in order to to directly investigate its potential as a building block for force or strain micro sensor arrays, AFM based methods are developed to characterize both longitudinal and transverse sensing modes. To extend this effect to other functional materials, CdSe and GaN nanowire arrays are characterized. Experimental results show exponential response of the conductivity change to applied forces. Theoretical models are presented to explain this mechanism and quantify the relationship, where strain induced piezoelectric polarization changes the metal-semiconductor Schottky barrier height. The AFM method demonstrated here provide an agile approach to investigate electromechanical coupling for the as-grown nanowires. The superior performance in force sensing with piezotronic effect will have potential applications in human-machine interface, cell-manipulation robotics, etc.

For the study on triboelectrification, an in-situ method with combination of AFM and SKPM is developed to characterize the charge transfer process, including

tribo-charge intensity, multi-cycle friction effect, as well as its surface diffusion. This method provides a powerful tool for in-situ study of the intrinsic parameters such as charge transfer kinetics and diffusion coefficient.

Utilizing this method, effect of external electric field was investigated as an approach to manipulate the polarization and intensity. The experimental results between Pt and Parylene film show that the triboelectrification can be nullified or enhanced to be eight times higher with a 10 V bias. This study demonstrates an effective approach for controlling the contact electrification, with potential applications in charge-assisted separation, energy harvesting as well as anti-static protection.

Finally, a concept of self-powered motion sensing technology is developed using micro-grated triboelectric structure and is demonstrated experimentally with nanometer resolution, long working distance as well as high robustness. It provides a promising solution for application areas that need ultra-low power consumption devices.

In summary, this dissertation presents new SPM based characterization methods for study of two newly discovered or re-utilized transduction effects - piezotronics and triboelectrification for advanced mechanical sensing mechanisms. We envision these effects and the self-powered motion sensing technology to have extensive applications in the emerging wave of “internet of things”.

REFERENCES

1. Someya, T.; Sekitani, T.; Iba, S.; Kato, Y.; Kawaguchi, H.; Sakurai, T. *P Natl Acad Sci USA* **2004,** *101* (27), 9966-9970.
2. Jager, E. W. H.; Inganas, O.; Lundstrom, I. *Science* **2000,** *288* (5475), 2335-2338.
3. Zhou, J.; Gu, Y. D.; Fei, P.; Mai, W. J.; Gao, Y. F.; Yang, R. S.; Bao, G.; Wang, Z. L. *Nano Lett.* **2008,** *8* (9), 3035-3040.
4. Wang, X. D.; Zhou, J.; Song, J. H.; Liu, J.; Xu, N. S.; Wang, Z. L. *Nano Lett.* **2006,** *6* (12), 2768-2772.
5. Wang, Z. L. *J Phys Chem Lett* **2010,** *1* (9), 1388-1393.
6. Zhang, Y.; Liu, Y.; Wang, Z. L. *Adv. Mater.* **2011,** *23* (27), 3004-3013.
7. Zhou, J.; Fei, P.; Gu, Y. D.; Mai, W. J.; Gao, Y. F.; Yang, R.; Bao, G.; Wang, Z. L. *Nano Lett.* **2008,** *8* (11), 3973-3977.
8. Wu, W. Z.; Wei, Y. G.; Wang, Z. L. *Adv. Mater.* **2010,** *22* (42), 4711-4715.
9. Wu, W. Z.; Wang, Z. L. *Nano Lett.* **2011,** *11* (7), 2779-2785.
10. Wu, J. M.; Chen, C. Y.; Zhang, Y.; Chen, K. H.; Yang, Y.; Hu, Y. F.; He, J. H.; Wang, Z. L. *ACS Nano* **2012,** *6* (5), 4369-4374.
11. Butefisch, S.; Buttgenbach, S. *Tech Mess* **1999,** *66* (5), 185-190.
12. Chu, Z.; Sarro, P. M.; Middelhoek, S. *Sensor Actuat a-Phys* **1996,** *54* (1-3), 505-510.
13. Lee, H. K.; Chung, J.; Chang, S. I.; Yoon, E. *J Microelectromech S* **2008,** *17* (4), 934-942.
14. Gao, Y.; Wang, Z. L. *Nano Lett.* **2009,** *9* (3), 1103-1110.
15. Han, W. H.; Zhou, Y. S.; Zhang, Y.; Chen, C. Y.; Lin, L.; Wang, X.; Wang, S. H.; Wang, Z. L. *ACS Nano* **2012,** *6* (5), 3760-3766.
16. Fan, F. R.; Lin, L.; Zhu, G.; Wu, W. Z.; Zhang, R.; Wang, Z. L. *Nano Lett.* **2012,** *12* (6), 3109-3114.
17. Fan, FR; Tian, Z. Q., Wang, Z. L. *Nano Energy* **2012,** *1* (2), 7.
18. Wang, S. H.; Lin, L.; Wang, Z. L. *Nano Lett.* **2012,** *12* (12), 6339-6346.
19. Zhu, G.; Pan, C. F.; Guo, W. X.; Chen, C. Y.; Zhou, Y. S.; Yu, R. M.; Wang, Z. L. *Nano Lett.* **2012,** *12* (9), 4960-4965.
20. Harper, W. R., *Contact and frictional electrification*. Laplacian Press: Morgan Hill, Calif., 1998; p xx, 369 p.
21. Wiles, J. A.; Grzybowski, B. A.; Winkleman, A.; Whitesides, G. M. *Anal. Chem.* **2003,** *75* (18), 4859-4867.
22. Zhu, G.; Lin, Z. H.; Jing, Q. S.; Bai, P.; Pan, C. F.; Yang, Y.; Zhou, Y. S.; Wang, Z. L. *Nano Lett.* **2013,** *13* (2), 847-853.
23. Wang, S. H.; Lin, L.; Xie, Y. N.; Jing, Q. S.; Niu, S. M.; Wang, Z. L. *Nano Lett.* **2013,** *13* (5), 2226-2233.
24. Lin, L.; Wang, S. H.; Xie, Y. N.; Jing, Q. S.; Niu, S. M.; Hu, Y. F.; Wang, Z. L. *Nano Lett.* **2013,** *13* (6), 2916-2923.
25. Kleber, W.; Makin, B. *Particul. Sci. Technol.* **1998,** *16* (1), 43-53.

26. Trigwell, S.; Grable, N.; Yurteri, C. U.; Sharma, R.; Mazumder, M. K. *Ieee T Ind Appl* **2003,** *39* (1), 79-86.
27. Lin, Z. H.; Xie, Y. N.; Yang, Y.; Wang, S. H.; Zhu, G.; Wang, Z. L. *ACS Nano* **2013,** *7* (5), 4554-4560.
28. Terris, B. D.; Stern, J. E.; Rugar, D.; Mamin, H. J. *Phys Rev Lett* **1989,** *63* (24), 2669-2672.
29. Hong, J. W.; Park, S. I.; Khim, Z. G. *Rev. Sci. Instrum.* **1999,** *70* (3), 1735-1739.
30. Germer, L. H. *J. Appl. Phys.* **1959,** *30* (1), 46-51.
31. Niu, S. M.; Wang, S. H.; Lin, L.; Liu, Y.; Zhou, Y. S.; Hua, Y. F.; Wang, Z. L. *Energ Environ Sci* **2013,** *6* (12), 3576-3583.
32. Kalinin, S. V.; Gruverman, A., *Scanning probe microscopy : electrical and electromechanical phenomena at the nanoscale*. Springer: New York, 2007.
33. Zhou, Y. S.; Wang, K.; Han, W. H.; Rai, S. C.; Zhang, Y.; Ding, Y.; Pan, C. F.; Zhang, F.; Zhou, W. L.; Wang, Z. L. *ACS Nano* **2012,** *6* (7), 6478-6482.
34. Colvin, V. L.; Schlamp, M. C.; Alivisatos, A. P. *Nature* **1994,** *370* (6488), 354-357.
35. Yu, Y. H.; Kamat, P. V.; Kuno, M. *Adv Funct Mater* **2010,** *20* (9), 1464-1472.
36. Jiang, Y.; Zhang, W. J.; Jie, J. S.; Meng, X. M.; Fan, X.; Lee, S. T. *Adv Funct Mater* **2007,** *17* (11), 1795-1800.
37. Li, G. H.; Zhai, T. Y.; Jiang, Y.; Bando, Y.; Golberg, D. *J Phys Chem C* **2011,** *115* (19), 9740-9745.
38. Schroder, D. K., *Semiconductor material and device characterization*. 3rd ed.; IEEE Press ;Wiley: Piscataway, N.J.; Hoboken, N.J., 2006; 779 p.
39. Swank, R. K. *Phys Rev* **1967,** *153* (3), 844.
40. Sze, S. M.; Ng, K. K., *Physics of semiconductor devices*. 3rd ed.; Wiley-Interscience: Hoboken, N.J., 2007; p x, 815 p.
41. Zhou, Y. S.; Hinchet, R.; Yang, Y.; Ardila, G.; Songmuang, R.; Zhang, F.; Zhang, Y.; Han, W. H.; Pradel, K.; Montes, L.; Mouis, M.; Wang, Z. L. *Adv. Mater.* **2013,** *25* (6), 883-888.
42. Songmuang, R.; Landre, O.; Daudin, B. *Appl. Phys. Lett.* **2007,** *91* (25).
43. Polian, A.; Grimsditch, M.; Grzegory, I. *J. Appl. Phys.* **1996,** *79* (6), 3343-3344.
44. Bykhovski, A. D.; Gelmont, B. L.; Shur, M. S. *J. Appl. Phys.* **1997,** *81* (9), 6332-6338.
45. Barker, A. S.; Ilegems, M. *Phys. Rev. B* **1973,** *7* (2), 743-750.
46. Xu, X.; Potie, A.; Songmuang, R.; Lee, J. W.; Bercu, B.; Baron, T.; Salem, B.; Montes, L. *Nanotechnology* **2011,** *22* (10).
47. CRC handbook of chemistry and physics. In Chapman and Hall/CRCnetBASE,: Boca Raton, FL, 1999; pp CD-ROMs.
48. Levinshteĭn, M. E.; Rumyantsev, S. L.; Shur, M., *Properties of advanced semiconductor materials : GaN, AlN, InN, BN, SiC, SiGe*. Wiley: New York, 2001; p xvii, 194 p.
49. Yang, Y.; Qi, J. J.; Guo, W.; Gu, Y. S.; Huang, Y. H.; Zhang, Y. *Phys. Chem. Chem. Phys.* **2010,** *12* (39), 12415-12419.
50. Zhou, Y. S. L., Y.; Zhu, G.; Lin, Z. H.; Pan, C.; Jing, Q.; Wang, Z. L. *Nano Lett.* **2013,** *13* (6), 6.

51. Grzybowski, B. A.; Fialkowski, M.; Wiles, J. A. *J Phys Chem B* **2005,** *109* (43), 20511-20515.
52. Melitz, W.; Shen, J.; Kummel, A. C.; Lee, S. *Surf. Sci. Rep.* **2011,** *66* (1), 1-27.
53. Matsusaka, S.; Maruyama, H.; Matsuyama, T.; Ghadiri, M. *Chem. Eng. Sci.* **2010,** *65* (22), 5781-5807.
54. Knorr, N.; Rosselli, S.; Nelles, G. *J. Appl. Phys.* **2010,** *107* (5).
55. Guenther, R. B.; Lee, J. W., *Partial differential equations of mathematical physics and integral equations*. Dover ed.; Dover Publications: New York, 1996; p xii, 562 p.
56. Mesquida, P.; Stemmer, A. *Adv. Mater.* **2001,** *13* (18), 1395-1398.
57. Zhou, Y. S.; Wang, S. H.; Yang, Y.; Zhu, G.; Niu, S. M.; Lin, Z. H.; Liu, Y.; Wang, Z. L. *Nano Lett.* **2014,** *14* (3), 1567-1572.
58. Lorenz, R. D. *Space Sci Rev* **2008,** *137* (1-4), 287-294.
59. Kwetkus, B. A. *Particul. Sci. Technol.* **1998,** *16* (1), 55-68.
60. Niu, S. M. L., Y.; Wang, S. H.; Lin L.; Zhou. Y. S.; Hu, Y. F.; Wang, Z. L. . **2013**.
61. Diaz, A. F.; Felix-Navarro, R. M. *J. Electrostat.* **2004,** *62* (4), 277-290.
62. Horn, R. G.; Smith, D. T.; Grabbe, A. *Nature* **1993,** *366* (6454), 442-443.
63. Cole, J. J.; Barry, C. R.; Knuesel, R. J.; Wang, X. Y.; Jacobs, H. O. *Langmuir* **2011,** *27* (11), 7321-7329.
64. Wahlin, A.; Backstro.G. *J. Appl. Phys.* **1974,** *45* (5), 2058-2064.
65. Lowell, J.; Roseinnes, A. C. *Adv Phys* **1980,** *29* (6), 947-1023.
66. Lowell, J. *J. Phys. D: Appl. Phys.* **1979,** *12* (9), 1541-1554.
67. Zhou, Y. S.; Zhu, G.; Niu, S. M.; Liu, Y.; Bai, P. S.; Jing, Q.; Wang, Z. L. *Adv. Mater.* **2014,** *26* (11), 1719-1724.
68. Yoshino, T.; Kurosawa, K.; Itoh, K.; Ose, T. *Ieee J Quantum Elect* **1982,** *18* (10), 1624-1633.
69. Wolfenda.Pc. *J Phys E Sci Instrum* **1968,** *1* (8), 817-&.
70. Kosel, P. B.; Munro, G. S.; Vaughan, R. *Ieee T Instrum Meas* **1981,** *30* (2), 114-123.
71. Guckel, H.; Earles, T.; Klein, J.; Zook, J. D.; Ohnstein, T. *Sensor Actuat a-Phys* **1996,** *53* (1-3), 386-391.
72. Persano, L.; Dagdeviren, C.; Su, Y. W.; Zhang, Y. H.; Girardo, S.; Pisignano, D.; Huang, Y. G.; Rogers, J. A. *Nat Commun* **2013,** *4*.
73. Katz, E.; Buckmann, A. F.; Willner, I. *J Am Chem Soc* **2001,** *123* (43), 10752-10753.
74. Klauk, H.; Zschieschang, U.; Pflaum, J.; Halik, M. *Nature* **2007,** *445* (7129), 745-748.
75. Xu, S.; Qin, Y.; Xu, C.; Wei, Y. G.; Yang, R. S.; Wang, Z. L. *Nat Nanotechnol* **2010,** *5* (5), 366-373.
76. Arechederra, R. L.; Minteer, S. D. *Anal Bioanal Chem* **2011,** *400* (6), 1605-1611.